ELECTRONIC PROPERTIES OF NANO-CRYSTALLINE TITANIUM DIOXIDE THIN FILMS

THÈSE N^{O} 2094 (1999)

PRÉSENTÉE AU DÉPARTEMENT DE PHYSIQUE

ÉCOLE POLYTECHNIQUE FÉDÉRALE DE LAUSANNE

POUR L'OBTENTION DU GRADE DE DOCTEUR ÈS SCIENCES

PAR

Alain BALLY

Ingénieur physicien diplômé EPF
de nationalité suisse et originaire de Boussens (VD)

acceptée sur proposition du jury:

Dr P.E. Schmid, directeur de thèse
Dr P. Bujard, rapporteur
Prof. R. Griessen, rapporteur
Prof. F. Lévy, rapporteur
Prof. L. Zuppiroli, rapporteur

Lausanne, EPFL
1999

Propriétés électroniques de films minces d’oxyde de titane à grains nanométriques

Version abrégée

L’oxyde de titane est un matériau bon marché, chimiquement stable et non toxique. Par contre, ses propriétés électriques sont instables et c’est un modeste semi-conducteur ou un médiocre isolant selon le point de vue. Pour de nombreuses applications, il serait intéressant de le rendre soit plus isolant, soit plus conducteur. Le but de ce travail est de modifier les propriétés électriques de couches minces de TiO_2 nano-cristallin fabriquées par pulvérisation cathodique et de comprendre les mécanismes conduisant à ces changements.

Les facteurs principaux influençant la conduction électrique sont d’une part la concentration et le type des impuretés incorporées dans TiO_2 et d’autre part la morphologie des couches minces. L’étude a été scindée en deux parties. La première partie décrit les modifications du matériau pulvérisé obtenues par dopage des couches minces de TiO_2. Du niobium, du cérium, du fer ou du fluor ont été incorporés dans le TiO_2. La seconde partie décrit les modifications obtenues en changeant le gaz réactif utilisé durant la pulvérisation cathodique : ainsi de la vapeur d’eau a été substituée à l’oxygène.

Différentes techniques d’analyse ont été mises en œuvre pour caractériser les couches minces de TiO_2. Elles sont essentiellement divisées en quatre catégories. Les analyses chimiques comprennent la microsonde électronique, la spectroscopie par photoémission de rayon X et la spectroscopie de masse des ions secondaires. L’analyse de la structure et de la morphologie des films a été réalisée grâce à la diffraction des rayons X et à la microscopie à force atomique. Les propriétés électriques en mode continu ou alternatif ont été mesurées entre la température ambiante et 350°C. Finalement des mesures de transmission optique ont fourni des informations sur les états électroniques et la morphologie des couches.

Les résultats montrent qu’en choisissant des impuretés appropriées, le dioxyde de titane peut être rendu isolant (TiO_2:Ce) ou plus conducteur avec une conduction électrique de type *n* (TiO_2:Nb) ou de type *p* (TiO_2:Fe). Les couches minces de TiO_2 ne sont pas seulement modifiées du point de vue chimique, mais chaque dopage est accompagné par des changements de structure et de morphologie importants, comme la transformation de la structure anatase à la structure rutile. Il est aussi montré que les atomes incorporés engendrent des défauts tels que des lacunes d'oxygène. Ces défauts s'opposent à la variation de la conduction électrique introduite par les impuretés. Ainsi, malgré des concentrations de dopants de l'ordre du pour-cent, la variation de la conduction électrique est une augmentation ou une diminution de trois ordres de grandeur par rapport au TiO_2 non dopé. Les couches minces fabriquées avec de la vapeur d'eau présentent une augmentation de conductivité électrique de huit ordres de grandeur par rapport à des échantillons préparés avec de l'oxygène dans des conditions similaires. Aucun atome autre que le titane ou l'oxygène en concentration significative n'a été détecté dans ces couches minces. L'importante augmentation de la conduction électrique est due à l'injection dans les grains de TiO_2 d'électrons provenant de liaisons non saturées d'atomes de titane se trouvant à la surface des grains. C'est la taille nanométrique des grains qui rend possible un dopage aussi important.

Les résultats montrent que suivant les impuretés ou les gaz réactifs choisis, le dioxyde de titane peut être un bon isolant avec une constante diélectrique élevée ou un conducteur transparent raisonnable. La plage de conduction électrique couverte par les échantillons produits s'étend de 10^{-10} S m^{-1} à 10^{3} S m^{-1}.

Abstract

Titanium dioxide is a cheap, chemically stable and non-toxic material. However its electrical properties are unstable and it is a modest semiconductor and a mediocre insulator. For several applications it would be interesting to make it either more insulating or more conducting. The goal of this work was to modify the electrical properties of nano-crystalline TiO_2 thin films deposited by reactive sputtering and to understand the mechanism leading to these modifications.

The principal factors that influence the electrical conductivity are on the one hand the concentration and nature of the chemical impurities incorporated in TiO_2, and on the other hand the morphology of the thin films. The study was split into two parts. The fist part describes the modifications of the sputtered material obtained by chemical doping of the TiO_2 thin films. Niobium, cerium, iron, and fluorine were incorporated successfully in TiO_2. The second part describes the modifications obtained by modifying the reactive gas used during the sputtering process: thus oxygen was substituted with water vapor.

Several analysis techniques have been used to characterize the TiO_2 thin films. They are essentially divided in four categories. The chemical analyses included electron probe microanalyses, x-ray photoemission spectroscopy, and secondary ion mass spectrometry. The structure and morphology analyses of thin films were carried out with x-ray diffraction and atomic force microscopy. The electrical properties in dc or ac mode were measured between room temperature and 350°C. Finally optical transmission provided information on the electronic states and morphology of the thin films.

With an appropriate choice of impurities, titanium dioxide can be made more insulating (TiO_2:Ce), more conducting with an *n*-type electrical conductivity (TiO_2:Nb) or *p*-type electrical conductivity (TiO_2:Fe). Chemical doping is also the cause of important structure and morphology changes, for example it can force the transformation from the anatase to the rutile structure. It is shown in particular that dopant atoms generate defects such as oxygen vacancies. These defects impede the variation of the electrical conductivity produced by the impurities, thus, in spite of dopant concentration in the percent range, the variation of the electrical conductivity is an increase or a decrease of three order of magnitude at most when compared with undoped TiO_2. Thin films deposited with water vapor as the reactive gas present an increase in the electrical conductivity by height order of magnitude compared to samples prepared with oxygen in similar conditions. No atom other than titanium or oxygen could be detected in the thin films in significant concentration. The dramatic conductivity increase is due to the injection inside TiO_2 grains of electrons donated by unsaturated titanium

atoms lying on the grain surface. A nanometric grain size is a requirement to make such high doping levels possible.

Depending on the impurities or reactive gas selected, titanium dioxide can be made either into a good insulator with a high breakdown field and a high permittivity or into a reasonably conducting, transparent film. The electrical conductivity of the samples prepared for this study cover the range from 10^{-10} to 10^{3} S m^{-1}.

Contents

Chapter 1

Introduction

Titanium dioxide (TiO_2) is a material used in a wide range of common and high-tech applications. It is cheap, chemically stable, non-toxic, and last but not least bio-compatible. Titanium is successfully used as implant material for dental, orthopedic and osteosynthesis application and its native oxide is mostly constituted of titanium dioxide [1]. TiO_2 powder is used as white pigment in paint [2], replacing lead oxide which is toxic, and in toothpaste. Transparent single crystals or thin films have a high refractive index that makes TiO_2 suitable for optical applications [3-5]. Multi-layers composed of TiO_2 and SiO_2 are designed to make antireflection coatings in the whole visible range [6-7]. TiO_2 is widely used for photocatalysis [8], for example for water treatment by oxidation of dissolved organic molecules [9-11]. Electrodes made of TiO_2 are used in electrochromic devices [12] and dye-sensitized solar cells [13]. Solid-state photovoltaic solar cells with porous TiO_2 layer show promising results [14-15]. Pd-TiO_2 diodes are used as hydrogen gas sensor [16-17], and nowadays TiO_2 can replace ZrO_2 in lambda probes used in the car industry [18]. Thus, research in many different fields is devoted to titanium dioxide under various forms such as single crystals, ceramics, and thin films.

Titanium oxide has four known structures under ambient conditions: rutile, anatase, brookite, and srilankite (this last structure is also called α-PbO_2 type TiO_2 or TiO_2-II) [19-21]. The rutile structure is the most stable [21] and also the most studied. TiO_2 can be synthesized as single crystals, powders, ceramics and thin films. Transition metal oxides are often nonstoichiometric, at near-atmospheric oxygen pressure the oxygen vacancies is the predominant defect in TiO_2 [22]. The oxygen deficiency introduces an excess of electrons in the material resulting in an increase of the electrical conductivity [22]. The oxygen vacancies act as electron donors, thus TiO_{2-x} is an n-type semiconductor, in contrast with p-type semiconductors which contain electron acceptors and where the charge carriers are holes rather than electrons [23]. Substoichiometric TiO_{2-x} is both a poor insulator and a modest semiconductor. Therefore several attempts have been made either to control the oxygen vacancy concentration or to introduce charge carriers (doping) inside TiO_2 in order to increase or decrease the electrical conductivity, depending on the desired application. During the last 40 years, almost half the atoms of the periodic table have been incorporated into TiO_2 [24-48]. An overview of their effects on conductivity is presented in Figure 1.1. For example, when niobium or tantalum atoms are incorporated into TiO_2, they act as electron donors [31-30], resulting in an increase of the electrical conductivity. Chromium, manganese, and iron are reported as electron acceptors [31,34,26] increasing or decreasing the TiO_2 electrical conductivity depending on the ratio between their concentration and the oxygen vacancy concentration [29]. These incorporations do not only modify the electrical conductivity of TiO_2, but also influence the structure and morphology of TiO_2. For instance, silicon incorporation favors the anatase structure, while tin incorporation favors the rutile structure [36]. Large atoms like cerium can break the crystal lattice resulting in amorphous TiO_2 [49].

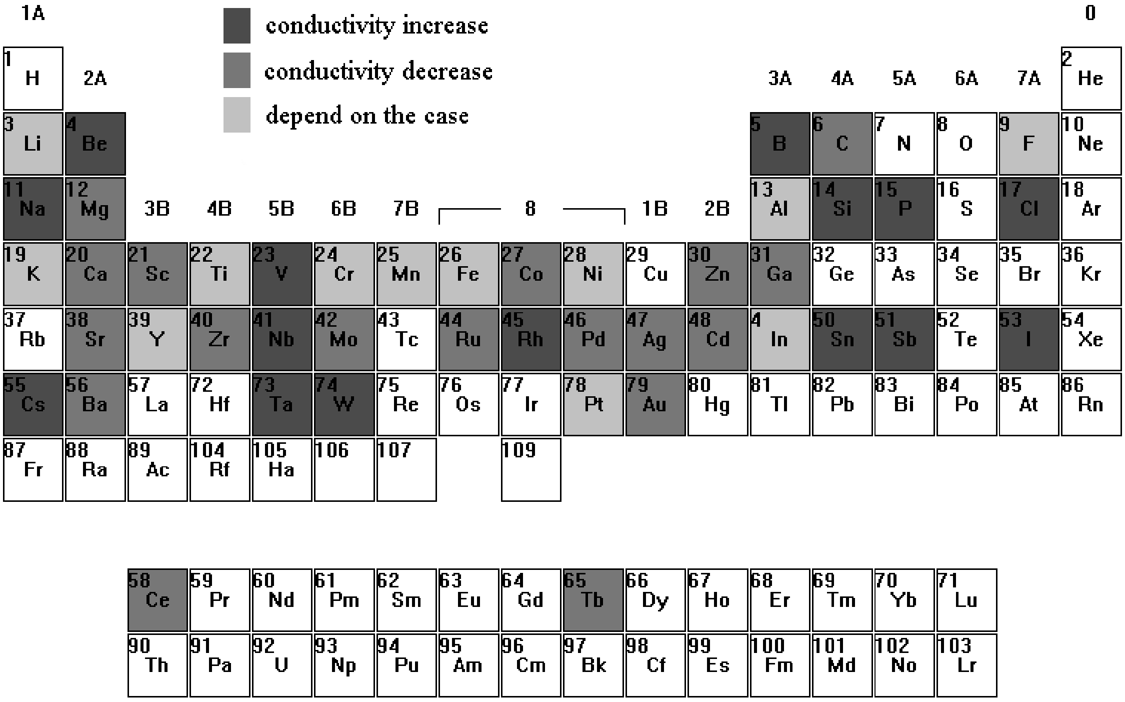

Figure 1.1: Table of impurities included inside TiO_2.

In spite of the work done on this subject, it is difficult to draw general conclusions on the behavior of the impurities incorporated into TiO_2, in particular when the morphology of the TiO_2 samples changes. For instance the ac electrical properties of a single crystal depend essentially on bulk properties, while grain boundary contributions could be important in thin films [50]. In this case, it is necessary to know where the impurities are located, either inside the grains or at their surface, to relate the properties of the thin films to the properties of the single crystals. Because of the large potential of TiO_2 in applications and the lack of a basic understanding of this material, the research on this material is mostly topical. The applications are essentially focussed on TiO_2 thin films.

In this work, we are interested in the improvement of the electrical conductivity of TiO_2 with impurity incorporation in order to make on the one hand a better insulator than pure TiO_2

and on the other hand a better conductor than pure TiO_2. Both have to be as stable as possible under thermal treatment. Insulating TiO_2 is interesting because it has a high static dielectric constant: 173 for the rutile structure and 48 for the anatase structure [51]. If the electrical conductivity of TiO_2 is high enough, it could be used as transparent conducting oxide (TCO) like indium-tin oxide, fluorine doped tin oxide or zinc oxide [52]. In any case, more conducting n-type and p-type TiO_2 are useful for catalytic applications.

The samples described in the present work are TiO_2 thin films, less than 1 μm thick, deposited on several substrates such as glass and silicon. The deposition technique is reactive sputtering [53]. The starting material (target) is metal titanium that is sputtered by plasma typically composed of argon and oxygen, in order to obtain titanium oxide. In a first stage, impurities are incorporated inside TiO_2 by modifying the target composition. Among the dopants tested, three have been subjected to deeper investigations. The first is cerium doping which results in highly insulating, amorphous, layers. The second is niobium incorporation, which is one of the most common ways to make conducting, n-type TiO_2, for a comparison with the results reported in literature. The third is iron doping because it is an important impurity found in industrial-grade titanium metal. When iron concentration is sufficiently high, TiO_2:Fe becomes a p-type semiconductor. In a second stage of the present study, the oxygen used as reactive gas during the thin film deposition has been replaced with water vapor. Thin films deposited with water vapor present a high electrical conductivity, 10^8 times higher than the conductivity of undoped TiO_2 deposited with O_2 as reactive gas, in the same conditions, nevertheless they are transparent.

Beside the electrical measurements, the chemical composition, the structure, the morphology, and the optical properties of the TiO_2 thin films have been investigated. All these measurements are necessary to understand the effect of the impurities incorporated in TiO_2, and to try to make quantitative interpretations of the results.

The manuscript is divided in seven chapters. Chapter 2 gives an overview of TiO_2 and its semiconductor properties which are necessary to understand the later chapters. Chapter 3 explains the fabrication of the thin films and describes the reactive sputtering method. The different techniques of analysis are reported in Chapter 4. Results on titanium dioxide doped with cerium, niobium, and iron, are presented in Chapter 5. Chapter 6 relates the effect of water vapor used as reactive gas during the deposition of titanium oxide. Chapter 7 ends the thesis with a general conclusion. Appendices contain the full text of papers published in the course of the thesis.

Bibliography

[1] C. E. Sittig: “Charakterisierung der Oxidschichten auf Titan und Titanlegierungen sowie deren Reaktionen in Kontact mit biologisch relevanten Modellösungen”, Dissertation ETH Nr. 12657, Zürich (1998).

[2] W. Clark and P. Broadhead, Journal of Physics C 3 (1970), 1047.

[3] R. R. Willey: “Practical design and production of optical thin films”, Marcel Dekker, New York (1996).

[4] M. Radecka, K. Zahrzewska, H. Czternastek, and T. Stapinski, Applied Surface Science 65/66 (1993), 227.

[5] S. Lee, B. Hun Park, and S.-G. Oh, Journal of the Korean Physical Society 31 (1997), 352.

[6] X. Orignac, H. C. Vasconcelos, X. M. Du, and R. M. Almeida, Journal of Sol-Gel Science and Technology 8 (1997), 243.

[7] R. E. Hummel, and K. H. Guenther: “Handbook of optical properties ; vol. 1: Thin films for optical coatings”, CRC, (1995).

[8] M. Schiavello: “Heterogeneous Photocatalysis”, John Wiley & Sons, New York (1997).

[9] D. Dumitriu, A. R. Bally, C. Ballif, V. I. Parvulescu, P. E. Schmid, R. Sanjinés, and F. Lévy, Preparation of Catalysts VII (1998), 485.

[10] T. Sakata and T Kawai, Chemical Physics Letters 80 (1981), 341.

[11] J. Y. Ying and T. Sun, Journal of Electroceramics 1 (1997), 219.

[12] P. Bonhôte, J. E. Moser, N. Vlachopoulos, L. Walder, S. M. Zakeeruddin, R. Humphry-Baker, P. Pechy, and M. Graetzel, Journal of Chemical Society, Chemical Communication (1996), 1163.

[13] M. Grätzel and K. Kalyanasundaram, Current Science 66 (1994), 706.

[14] S. Siebentritt, K. Ernst, C.-H. Fischer, R. Könenkamp, and M. C. Lux-Steiner, 14th European Photovoltaic Solar Energy Conference, Barcelona, Spain 30 june-4 July (1997), 1823.

[15] K. Tennakone, G. R. R. A. Kumara, I. R. M. Kottegoda, V. P. S. Perera, and G. M. L. P. Aponsu, Journal of Physics D: Applied Physics 31 (1998), 2326.

[16] A. Mandelis and C. Christofides: “Physics, chemistry and technology of solid state gas sensor devices”, John Wiley & Sons, New York (1993).

[17] N. Yamamoto, S. Tonomura, and H. Tsubomura, Journal of the Electrochemical Society 129 (1982), 444.

[18] J. Bilbao: “Cours du brevet fédéral d’électromecanicien”, (1999).

[19] R. W. G. Wyckoff: “Crystal structure”, Interscience Publishers, New York (1965).

[20] R. K. Linde and P. S. DeCarli, The Journal of Chemical Physics 50 (1969), 319.

[21] J. Haines and J. N. Léger, Physica B 192 (1993), 233.

[22] P. Kofstad: “Nonstoichiometry, diffussion, and electrical conductivity in binary metal oxides”, Wiley Interscience, New York (1972).

[23] S. M. Sze: “Physics of semiconductor devices”, Wiley Interscience, New York (1981).

[24] G. H. Johnson, Journal of The American Ceramic Society 36 (1953), 97.

[25] J. F. Houlihan, J. R. Hamilton, and D. P. Madacsi, Material Research Bulletin 14 (1979), 915.

[26] N. G. Eror, Journal of Solid State Chemistry 38 (1981), 281.

[27] K. Tennakone, S. W. M. S. Wickramanayake, P. Samarasekara, and C. A. N. Fernando, Physica Status Solidi (a) 104 (1987), K57.

[28] S. R. Kurtz and R. G. Gordon, Thin Solid Films 147 (1987), 167.

[29] J.-L. Carpentier, A. Lebrun, and F. Perdu, Journal of Physics and Chemistry of Solids 50 (1989), 145.

[30] E. C. Akubuiro and X. E. Verykios, Journal of Physics and Chemistry of Solids 50 (1989), 17.

[31] A. Bernasik, M. Radecka, M. Rekas, and M. Sloma, Applied Surface Science 65/66 (1993), 240.

[32] Y. Takao, Y. Iwanaga, Y. Shimizu, and M. Egashira, Sensors and Actuators B 10 (1993), 229.
Y. Takao, K. Fukada, Y. Shimizu, and M. Egashira, Sensors and Actuators B 10 (1993), 235.

[33] K. Satake, A. Katayama, H. Ohkoshi, T. Nakahara and T. Takeushi, Sensors and Actuators B 20 (1994), 111.

[34] S. Fujitsu and T. Hamada, Journal of The American Ceramic Society 77 (1994), 3281.

[35] H. Tang, K. Prasad, R. Sanjinés, and F. Lévy, Sensors and Actuators B 26-27 (1995), 71.

[36] S. Vemury and S. E. Pratsinis, Journal of The American Ceramic Society 78(11) (1995), 2984.

[37] R. Zanoni, G. Righini, A. Montenero, G. Gnappi, A. Bearzotti, G. Montesperelli, and E. Traversa, Sensors and Actuators B 24-25 (1995), 886.

[38] R. Fromknecht, R. Auer, I. Khubeis, and O. Meyer, Nuclear Instruments and Methods in Physics Research B 120 (1996), 252.

[39] F. Bregani, C. Casale, L. E. Depero, I. Natali-Sora, D. Robba, L. Sangaletti, and G. P. Toledo, Sensors and actuators B 31 (1996), 25.

[40] E. Traversa, G. Gnappi, A. Montenero, and G. Gusmano, Sensors and actuators B 31 (1996), 59.

[41] K. Hatta, M. Higuchi, J. Takahashi, and K. Kodaira, Journal of Crystal Growth 163 (1996), 279.

[42] M. Stromme, A. Gutarra, G. A. Niklasson, and C. G. Granqvist, Journal of Applied Physics 79 (1996), 3749.

[43] Md. Mosaddeq-ur-Rahman, T. Miki, K. Murali Krishna, T. Soga, K. Igarashi, S. Tanemura, and M. Umeno, Materials Science and Engineering B41 (1996), 67.

[44] A. Stashans, S. Lunell, R. Bergström, A. Hagfeldt and S.-E. Lindquist, Physical Review B 53 (1996), 159.

[45] W. A. Badaway, Journal of Materials Science 32 (1997), 4979.

[46] O. Meyer, I. Khubeis, R. Fromknecht, and S. Massing, Nuclear Instruments and Methods in Physics Research B 127/128 (1997), 624.

[47] I. Khubeis, R. Fromknecht, and O. Meyer, Physical Review B 55(1) (1997), 136.

[48] C. H. Lee and C. W. Ching, Materials Chemistry and Physics 47 (1997), 193.

[49] K. Prasad, A. R. Bally, P. E. Schmid, F. Lévy, J. Benoit, C. Barthou, and P. Bénalloul, Japanese Journal of Applied Physics 36 (1997), 5696. Paper reported in Appendix A.

[50] J. R. Macdonald: “Impedance spectroscopy”, John Wiley & Sons, New York (1987).

[51] A. Eucken and A. Büchner, Zeitschrift für physikalische Chemie B 27 (1935), 321.

[52] H. L. Hartnagel, A. L. Dawar, A. K. Jain, and C. Jagadish: “Semiconducting transparent thin films”, Institute of Physics Publishing, Bristol (1995).

[53] M. Ohring: “The materials Science of Thin Films”, Academic Press, San diego (1992).

Chapter 2

General properties of titanium dioxide

This chapter gives information necessary to understand the discussions and interpretations of the measurements made on TiO_2 thin films. It starts with a description of the different polymorphs of titanium dioxide. Then, a short reminder the properties of semiconductors are presented. The notion of oxygen vacancy, of chemical impurity is introduced, and the manner in which they can influence the electrical conductivity is explained.

2.1 TiO_2 crystal structures

The titanium oxide can crystallize in different structures. At ambient conditions, four structures are known: rutile, anatase, brookite, and srilankite [1]. At higher pressure, i.e. more than 10 Gpa, a baddeleyite structure appears [2], and theoretical work predicts a new structure, not yet observed, similar to fluorite HfO_2 at even higher pressure [3]. The most common and studied structure is rutile, it is also the most stable structure of TiO_2 [4]. TiO_2 thin films with all of the four structures can be synthesized, though generally only anatase and rutile are present. The brookite structure has been obtained by the sol-gel method [5-6], and TiO_2-II (srilankite) has been grown by atomic layer epitaxy from $TiCl_4$ and H_2O [7]. To our knowledge, only rutile and anatase have been produced by sputtering, which is the process used to prepare our samples. It is also possible to produce amorphous TiO_2 thin films at low temperature, i.e. below 150°C, in our sputtering installations. Structural, optical, and electrical properties of TiO_2 are reported in Table 2.I.

Table 2.I: TiO_2 properties.

polymorph	rutile	anatase	brookite	Srilankite
structure [1]	tetragonal $P4_2/mnm$	tetragonal $I4_1/amd$	orthorhombic Pcab	orthorhombic Pbcn
density [1]	4.25	3.89	4.12	4.37

refraction index
λ = 600 nm [8]
	⊥ to c axis
	2.60
	// to c axis
	2.89
		⊥ to c axis
		2.55
		// to c axis
		2.48
			// to a or b axis
			2.57
			// to c axis
			2.69	

dielectric constant [9-11]	⊥ to c axis 89 // to c axis 173	⊥ to c axis 31 // to c axis 48	78	
band gap [eV] [12-13]	⊥ to c axis direct 3.04 // to c axis indirect 3.05	⊥ to c axis direct 3.42 // to c axis indirect 3.46	3.14	
electron mobility [10^{-4} m^2/Vs] [12, 14, 15]	crystal: 0.1–10 thin film: 0.1	crystal: 15–550 thin film: 0.1-4		

The elementary cells of the TiO_2 crystal structures are presented in Figure 2.1. Rutile and anatase, which are tetragonal, are more ordered than the orthorhombic structure. The anatase, which is the least dense structure, has empty channels along the a and b axes.

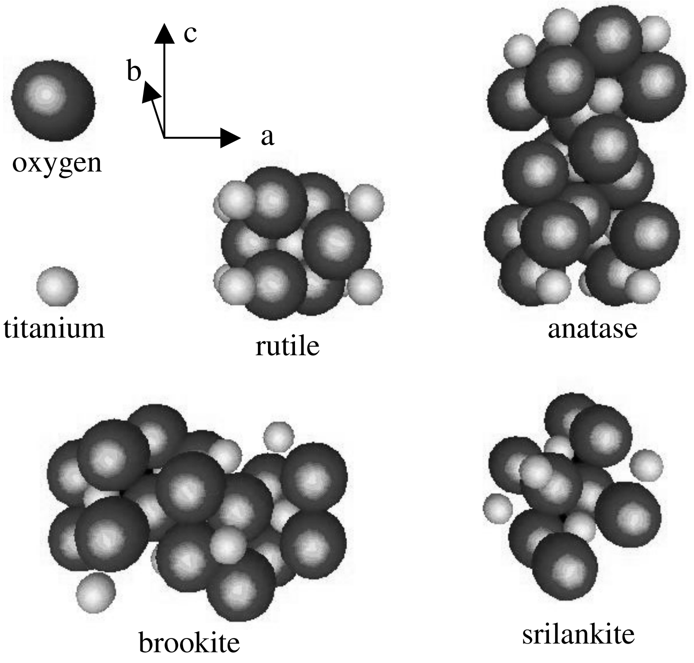

Figure 2.1: Elementary cell of TiO_2 polymorphs.

In the following, the description of the properties of titanium oxide will be focussed on the rutile and anatase polymorphs of TiO_2 because they are the only polymorphs synthesized in our thin films. When the titanium oxide stoichiometry is varied from 0 to 2, Ti, Ti_2O, TiO, Ti_2O_3, Ti_3O_5, Ti_nO_{2n-1}, and TiO_2 are encountered (see Figure 2.2). Rutile and anatase structures are compatible with stoichiometries higher than 1.95 only. No titanium oxide structure with a stoichiometry higher than 2 has been reported.

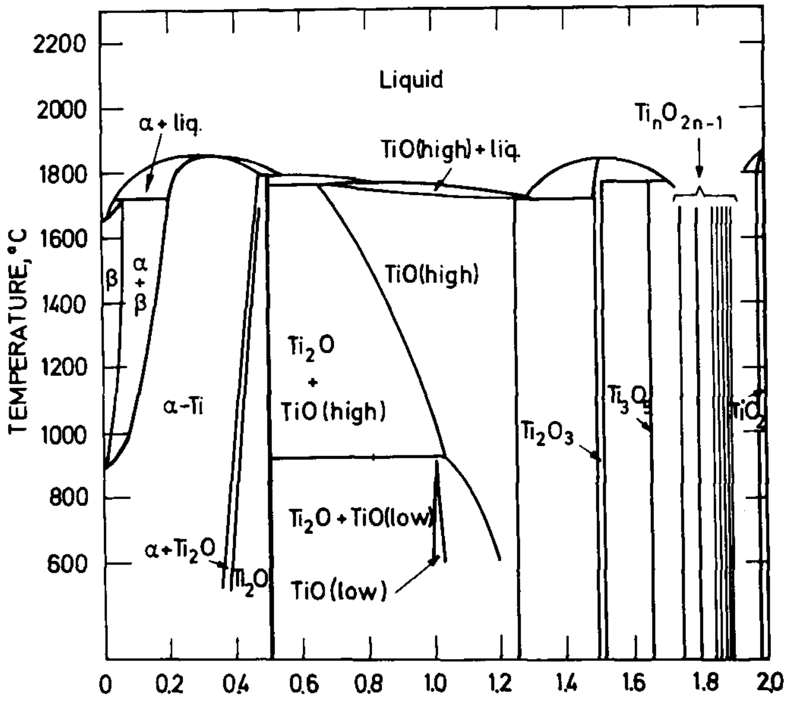

Figure 2.2: The titanium oxygen phase diagram [16].

Rutile can exist at any temperature below 1800°C, at which point titanium dioxide becomes liquid, while for temperatures above 700°C the anatase structure changes to the rutile structure [17]. To our knowledge, the reverse transformation never occurs. The transformation temperature can be modified by adding impurities into TiO_2. For instance, the anatase phase completely disappears at temperature of about 530°C, 680°C, and 830°C for powder samples containing vanadium, molybdenum, and tungsten respectively [18].

2.2 Semiconductor properties

The information given in this section relies on the work of S. M. Sze [19]. Solid materials are classified in three groups depending on their electrical conductivity σ. Highly conducting materials are metals ($\sigma > 10^4$ S m^{-1}), material with very low electrical conductivity are insulators ($\sigma < 10^{-8}$ S m^{-1}), and in-between stand the semiconductors. The main difference between metal and semiconductor is the fact that for metals, the electrical conductivity decreases when temperature increases, while the reverse phenomenon usually occurs in the case of semiconductors.

The energy band diagram of a pure semiconductor containing a negligible amount of impurities (intrinsic semiconductor), is characterized by an energy gap (E_G) inside which no electronic states are encountered. The electrical conductivity is given by the following formulas:

$$\sigma = \sigma_n + \sigma_p = q\,\mu_n\,n + q\,\mu_p\,p$$

where $n = N_c \exp\left(-\dfrac{E_C - E_F}{kT}\right)$ is the electron density in the conduction band,

$p = N_V \exp\left(-\dfrac{E_F - E_V}{kT}\right)$ is the hole density in the valence band,

$E_F = \dfrac{E_C + E_V}{2} + \dfrac{kT}{2}\ln\left(\dfrac{N_V}{N_C}\right)$ is the Fermi energy,

q is the electronic charge, k is Boltzmann's constant, T the absolute temperature, μ_n and μ_p are the electron and hole mobility respectively, N_C and N_V are the effective density of state of the conduction and valence band, E_C the energy of the bottom of conduction band, and E_V the energy of the top of valence band (see Figure 2.3).

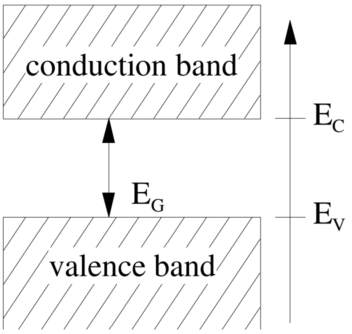

Figure 2.3: Simplified band diagram of a semiconductor.

When a semiconductor is doped with donor and/or acceptor impurities, impurity energy levels are introduced. A donor level is defined as being neutral if filled with an electron, and positive if empty. An acceptor level is neutral if empty, and negative if filled by an electron. The Fermi level for the intrinsic semiconductor lies close to the middle of the bandgap (see Figure 2.4 (a)). When impurity atoms are introduced, the Fermi level must adjust itself to preserve charge neutrality (see Figure 2.4 (b) and (c)), the total negative charge (electrons and ionized acceptors) must equal the total positive charge (holes and ionized donors). n-type (donors impurities) and p-type (acceptor impurities) semiconductor band diagrams and density of states are given in Figure 2.4 (b) and (c).

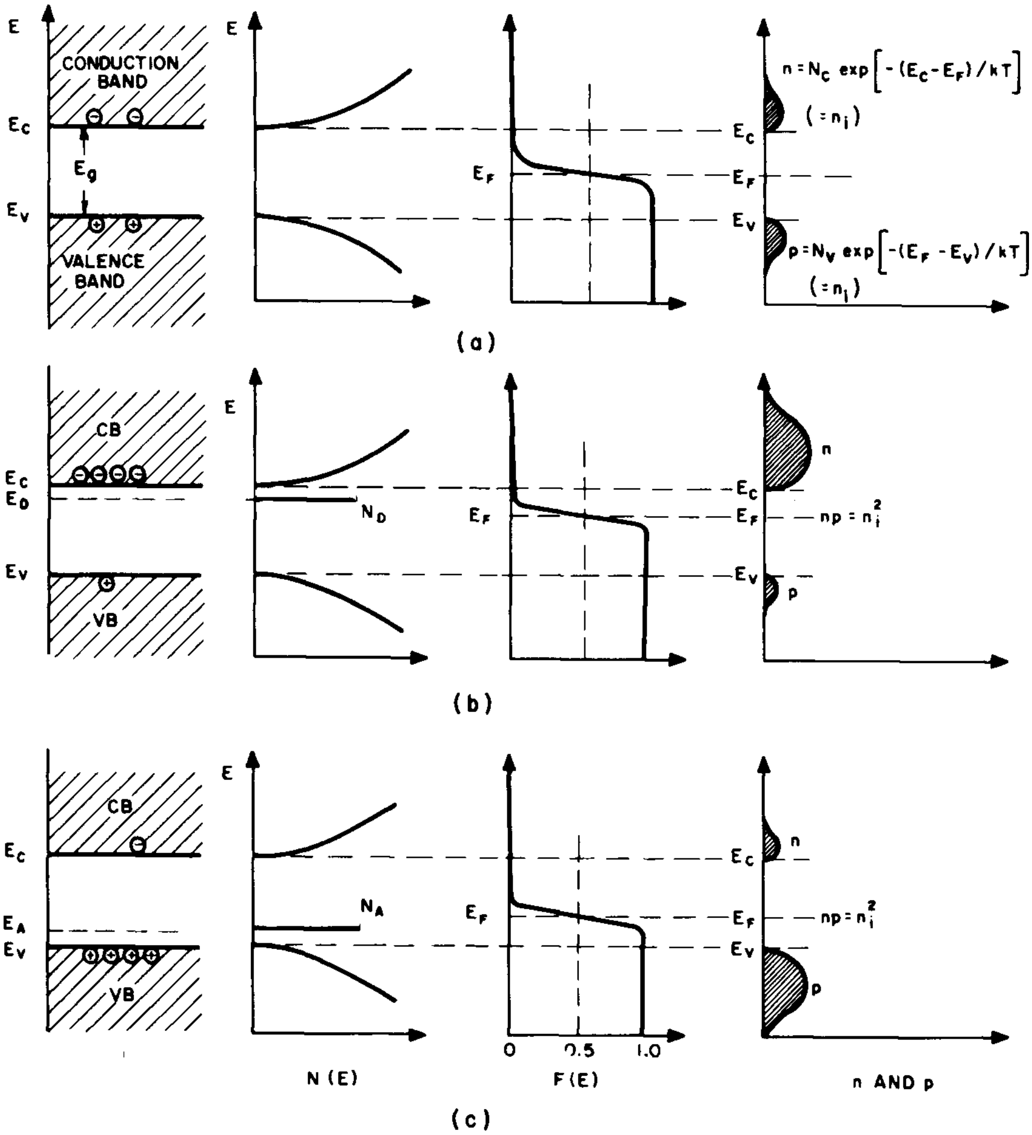

Figure 2.4: Schematic band diagram, density of states, Fermi-Dirac distribution, and the carrier concentration for (a) intrinsic, (b) n-type, and (c) p-type semiconductors at thermal equilibrium [19].

Consider the case where donor impurities with concentration N_D and acceptor impurities with concentration N_A: the charge neutrality is given by:

$$N_A^- + n = N_D^+ + p$$

where $N_D^+ = N_D\left(1 - \dfrac{1}{1 + \dfrac{1}{g_D}\exp\left(\dfrac{E_D - E_F}{kT}\right)}\right)$ is the number of ionized donors,

$$N_A^- = \frac{N_A}{1 + g_A \exp\left(\frac{E_A - E_F}{kT}\right)}$$ is the number of ionized acceptor,

E_D and E_A the ionization energy of the donors and acceptors, and g_D and g_A are the ground-state degeneracies of the donors and acceptors.

For a set of given N_C, N_V, N_D, N_A, E_C, E_V, E_D, E_A, and T, the Fermi level E_F can be uniquely determined. If μ_n and μ_p are known, the electrical conductivity can be calculated.

2.3 Oxygen vacancies and other impurities

The ideal crystal does not exist. At any temperature crystals contain various structural imperfections or defects. There are several types of such defects, and these are often divided into three main groups: point defects, line defects, and plane defects. Point defects include empty sites (vacancies), where constituent atoms are missing in the structure, and interstitial atoms occupying interstices between the regular atomic sites. Line defects or dislocations are characterized by displacements in the periodic structure in certain directions. The plane defects comprise stacking faults, internal surfaces (grain boundary), and external surfaces.

The most notable point defects of pure rutile TiO_2, called native point defects, are oxygen vacancies and interstitial titanium atoms. An oxygen vacancy is formed by the transfer of an oxygen atom on a normal site to the gaseous state. In the Kröger and Vink notation [20], the chemical reaction is written in the following way:

$$O_O \leftrightarrow V_O^x + \tfrac{1}{2} O_2$$

where O_O is an oxygen ion on a normal lattice site and V_O^x is a neutral oxygen vacancy.

The two trapped electrons (e´) associated with the vacancy may, depending on the temperature, be excited and freed from the vacancy. In this case, the vacancy acts as a donor and becomes singly ($V_O^{\cdot}$) or doubly ($V_O^{\cdot\cdot}$) charged [21]:

$$V_O^x \leftrightarrow V_O^{\cdot} + e'$$

$$V_O^{\cdot} \leftrightarrow V_O^{\cdot\cdot} + e'$$

An interstitial titanium is created in the following way:

$$Ti_{Ti} \leftrightarrow Ti_i^{\cdot\cdot\cdot} + V_{Ti}^{'''} \text{ or } Ti_{Ti} \leftrightarrow Ti_i^{\cdot\cdot\cdot\cdot} + V_{Ti}^{''''}$$

where Ti_{Ti} is an titanium ion on a normal lattice site, $Ti_i^{\bullet\bullet\bullet}$ or $Ti_i^{\bullet\bullet\bullet\bullet}$ are interstitial titanium (three or four times charged), and V_{Ti}''' or V_{Ti}'''' are titanium vacancy (three or four times charged).

The point defects contribute to the electrical conductivity in two ways. They can provide mobile charge carriers (ionization), or they can also move in response to an electric field and so produce an ionic current. Thus it is important to know the concentration of point defects in the material studied. The concentrations of point defects in TiO_2 at high temperature are reported in Figure 2.5. At near-atmospheric oxygen pressure oxygen vacancies are the predominant defects in both cases. As the enthalpy of formation of the oxygen vacancy (105 kcal/mol ≡ 4.55 eV/vacancy) is lower than the enthalpy of formation of a triply-charged interstitial titanium (210 kcal/mol ≡ 9.11 eV/interstitial titanium), the oxygen vacancy is also the dominant defect at room temperature. As the electrical measurements presented in this thesis were made at temperature lower than 400°C and generally in air, we will only consider oxygen vacancies as native point defects.

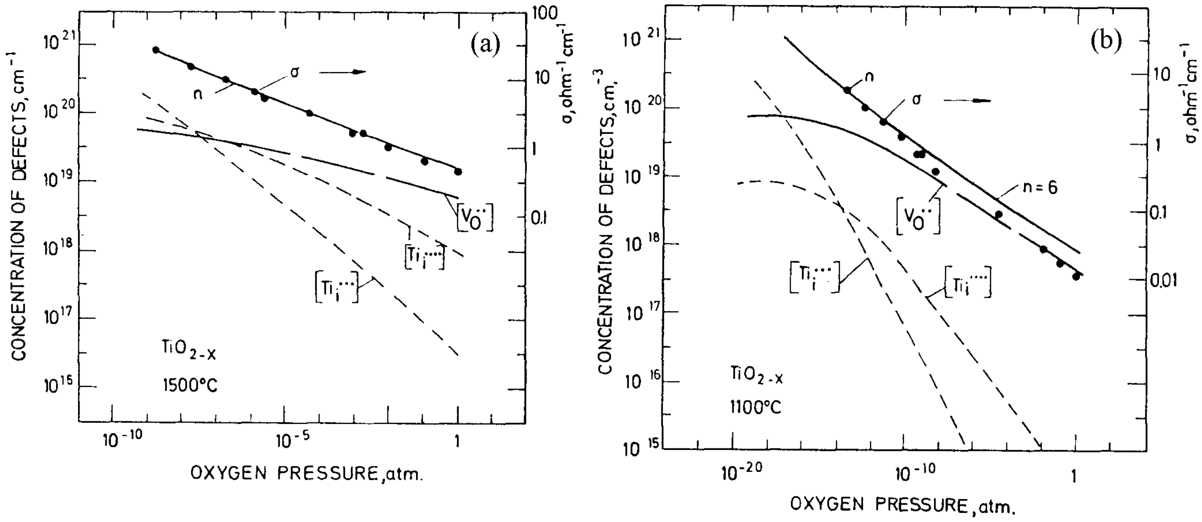

Figure 2.5: The concentration of point defects and electrons in rutile TiO_{2-x} as a function of the partial pressure of oxygen. (a) 1500°C; (b) 1100°C [21].

The ionic conductivity due to oxygen vacancies is related to the vacancy diffusion coefficient D through the Nernst-Einstein relation:

$$\sigma_D = q\,z\,c\,\mu_D$$

$$\text{with } \mu_D = \frac{q\,z\,D}{kT} \text{ and } z \text{ the valence}$$

The diffusion coefficient value is 10^{-14} cm^2/s at 850°C [21]. As it is thermally activated with an activation energy of 60 kcal/mole or 2.6 eV, its value at 400°C is much lower than 10^{-14} cm^2/s. With an oxygen vacancy concentration of 1% (~5 x 10^{20} cm^{-3}), the resulting conductivity is less than 5 x 10^{-11} Ω^{-1} cm^{-1}, therefore we will omit the ionic conduction and consider that oxygen vacancies contribute only to the electronic conduction as double donors with a shallow donor level (0 - 200 meV) and a deep donor level (600 – 750 meV) [12,22].

Although complete analyses of defect concentration in anatase TiO_2 have not been reported, we assume that oxygen vacancies are also the dominant point defects in anatase TiO_2.

When impurities are incorporated into TiO_2, they can dissolve inside the crystallites, or settle in the grain boundaries. They can also agglomerate, if the maximum solubility is exceeded, as precipitates either at the center of crystallites or at the grain boundaries. As the mechanisms involved are complex and multiple, it is not possible to describe here all that can happen when impurities are incorporated into the TiO_2 crystal lattice. Only two examples resulting in n-type TiO_2 and p-type TiO_2 will be shown.

The first example is niobium doping. If niobium replaces titanium, a chemical reaction can be written in this way

$$Nb_2O_5 \leftrightarrow 2\ Nbi_{Ti}^{\bullet} + 4\ O_O + 2\ e' + \tfrac{1}{2}\ O_2$$

The temperature has been supposed high enough to ionize the niobium atoms so that each gives up one electron [23]. If this is not the case, the number of ionized niobium atoms is settled by the ionization energy and the temperature using the Fermi-dirac distribution [24]. Instead of creating conduction electrons, charge compensation can also be achieved by lattice defects such as interstitial oxygens or titanium vacancies [23]:

$$Nb_2O_5 \leftrightarrow 2\ Nbi_{Ti}^{\bullet} + O_i^{''} + 4\ O_O$$

$$2\ Nb_2O_5 \leftrightarrow 4\ Nbi_{Ti}^{\bullet} + V_{Ti}^{''''} + 10\ O_O$$

The second example is aluminum doping. If Al_2O_3 is dissolved substitutionally in TiO_2 and if the predominating defects are oxygen vacancies, the reaction may be written

$$Al_2O_3 \leftrightarrow 2\ Al_{Ti}^{'} + V_O^{\bullet\bullet} + 3\ O_O$$

In this case the oxygen vacancy concentration is increased and correspondingly the electron concentration will be decreased [21]. The substitutional aluminum atom is, in this case, an acceptor impurity.

Bibliography

[1] Standard CPDS X-ray diffraction spectra database.

[2] J. Staun Olsen, L. Gerwald, and J. Z. Jiang, Journal of Physics and Chemistry of Solids 60 (1999), 229.

[3] J. K. Dewhurst and J. E. Lowther, Physical Review B 54 (1996), R3673.

[4] J. Haines and J. N. Léger, Physica B 192 (1993), 233.

[5] Md. Mosaddeq-ur-Rahman, T. Miki, K. Murali Krishna, T. Soga, K. Igarashi, S. Tanemura, and M. Umeno, Materials Science and Engineering B41 (1996), 67.

[6] M. Gotic, M. Ivanda, A. Sekulic, S. Music, S. Popovic, A. Turkovic, and K. Furic, Materials Letters 28 (1996), 225.

[7] J. Aarik, A. Aidla, V. Sammelselg, H. Siimon, and T. Uustare, Journal of Crystal Growth 169 (1996), 496.

[8] J. D'Ans, P. Ten Bruggengate, A. Eucken, G. Joos, and W. A. Roth, Landolt-Börnstein 6 II/8, Springer Verlag, Berlin (1965), 2-145.

[9] A. Eucken and A. Büchner, Zeitschrift für physikalische Chemie B 27 (1935), 321.

[10] S. Roberts, Physical Review 76 (1949), 1215.

[11] J. D'Ans, A. Eucken, G. Joos, and W. A. Roth, Landolt-Börnstein 6 II/6, Springer Verlag, Berlin (1959), 483.

[12] H. Tang: "Electronic properties of anatase TiO_2 investigated by electrical and optical measurements on single crystals and thin films", Thèse EPFL N° 1311, Lausanne (1994).

[13] M. Grätzel and F. P. Rotzinger, Chemical Physics Letters 118 (1985), 474.

[14] L. Forro, O. Chauvet, D. Emin, L. Zuppiroli, H. Berger, and F. Lévy, Journal of Applied Physics 75 (1994), 633.

[15] R. G. Breckenridge and W. Hosler, Physical Review 91 (1953), 793.

[16] P. G. Wahlbeck and P. W. Gilles, Journal of The American Ceramic Society 49 (1966), 180.

[17] J. B. Goodenough, A. Hammett, G. Huber, F. Hulliger, M. Leiss, S. K. Ramasesha, and H. Werheit, Landolt-Börnstein III/17g, Springer Verlag, Berlin (1984).

[18] F. Bregani, C. Casale, L. E. Depero, I. Natali-Sora, D. Robba, L. Sangaletti, and G. P. Toledo, Sensors and Actuators B 31 (1996), 25.

[19] S. M. Sze: "Physics of Semiconductor devices", Wiley Interscience, New York (1981).

[20] F. A. Kröger and H. J. Vink: "Solid State Physics", Academic Press, New York (1956), 307.

[21] P. Kofstad: "Nonstoichiometry, diffusion, and electrical conductivity in binary metal oxides", Wiley Interscience, New York (1972).

[22] K. Mizushima, M. Tanaka, A. Asai, S. Ilda, and J. B. Goodenough, Journal of Physics and Chemistry of Solids 40 (1979), 1129.

[23] G. Levin and C. J. Rosa, Zeitschrift für Metallkunde 70 (1979), 601.
G. Levin and C. J. Rosa, Zeitschrift für Metallkunde 70 (1979), 646.

[24] A. Bernasik, M. Radecka, M. Rekas, and M. Sloma, Applied Surface Science 65/66 (1993), 240.

Chapter 3

Thin film preparation

The manufacture of titanium oxide thin films is a sequence of three main stages.

1) The first stage consists in the choice of the substrates on which the oxide will be deposited. It depends on the kind of measurements planned for the sample. For example, depending on the thin film electrical resistance, electrical characterization is carried out preferentially on indium tin oxide coated glass (ITO) or on glass. Chemical analyses are advantageously made on top of a silicon substrate.
2) The second step is the deposition of the titanium oxide thin film by reactive sputtering, possibly followed by a heat treatment.
3) If necessary, electrical contacts are deposited in a third step by thermal evaporation (gold, aluminum) or sputtering (platinum, ITO).

3.1 Substrates

The substrate is important because it can influence the structure and the properties of the thin film. In an ideal case, all measurements should be made on the same kind of substrate to make sure that good correlations can be established between results, but it is often not possible. The substrates are described below and their use is listed in Table 3.I.

- Glass coated with indium-tin oxide (ITO): polycrystalline thin films (100nm, rutile-like structure) on glass, transparent to visible and near-infrared light, resistance 18 Ω/□ (MBC Merck Balzers Ltd).
- Glass: amorphous, transparent to visible and near-infrared light, electrical insulator (microscope slides, RE-WA Lehmann-Schmidt).
- Silicon: single crystal, (001) oriented, transparent to near and middle infrared light, resistivity 3-5 Ω cm, n-type doping (ACM).

- Silicon with both faces polished: single crystal, (001) oriented, transparent to near and middle infrared light, resistivity 0.07-0.13 Ω cm, p-type doping (ACM).

Table 3.I: Use of the substrates*.

Name	Measurement type			
	Structural	Chemical	Electrical	Optical
ITO	X-ray diffraction spectroscopy	-	Insulating layer	350 nm < λ < 2000 nm
Glass	X-ray diffraction spectroscopy Atomic force microscopy	-	Conductive layer	325 nm < λ < 4000 nm
Silicon	X-ray diffraction spectroscopy Transmission electron microscopy	Electron probe microanalysis X-ray photoemission Spectroscopy Secondary ion mass spectroscopy	-	5000 cm^{-1} < λ < 600 cm^{-1}

*See Chapter 4 for more details.

3.2 Reactive sputtering

3.2.1 Process description

The basic sputtering mechanism will be explained first in the simple case of a DC (direct current), diode, sputtering system (see Figure 3.1). Substrates are placed in a vacuum chamber facing the target which is composed of the material to be deposited. The sputtering gas is often an inert gas, generally argon, which is introduced into the chamber to a pressure between 10^{-3} to 10^{-2} mbar. A high negative voltage is applied to the target (cathode), while the substrate holder (anode) is connected to the chamber walls and to the ground. Under the applied high voltage, the gas is ionized and a plasma is created between the (small) cathode and the (large) anode. Positively charged ions are accelerated toward the cathode and their impact sputters atoms off the target. These atoms travel across the chamber and a fraction of them land on the substrate, resulting in a film that grows in thickness. The deposition rate depends on many parameters, especially on the pressure inside the chamber and on the power applied to the target. Detailed accounts of the sputter mechanisms can be found in the literature [1-3].

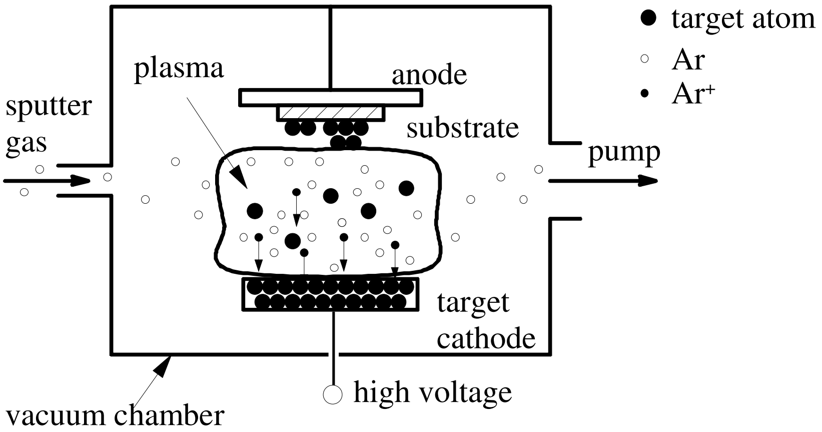

Figure 3.1: DC diode sputtering system.

If either the target or the material deposited is an insulator, an insulating layer may form over the target and accumulate charges until the discharge actually stops. In such a case, the DC power supply must be replaced by a RF power supply. The discharge frequency must be greater than 100 kHz to have a continuous discharge, i.e. in order to maintain the plasma discharge. Usually the applied frequency is the RF industrial frequency (13.56 MHz). In a low gas pressure discharge, electrons have a greater velocity than the ions, which are several thousand times heavier. Objects plunged inside the plasma sustain a more important electron bombardment than ion bombardment, and therefore they charge negatively until the ion current and electron current are equal. The bias that appears negative compared with the plasma potential is called self-bias. The current-voltage characteristic for the ion current in the dark space near an electrode is not linear, but has a diode-like curve. When RF voltage is applied, due to the asymmetric I-V characteristic, the total positive current crossing the electrode is larger than the total negative current; thus an additional negative bias appears leading to a zero dc current. Supposing that the anode and cathode currents are equal, and that the voltage bias is proportional to the inverse of the capacity, using the Langmuir-Child equation [1] for the ion current density near the electrode

$$j = K\frac{V^{3/2}}{M^{1/2}\,d^2}$$

where d is the thickness of the space charge zone, M is the ion mass, and K is a constant, we obtain the following relation between the self-polarization potential of the electrodes and the electrode areas: $V_{anode}/V_{cathode} = (A_{cathode}/A_{anode})^2$ [1]. This means that the larger the electrode, the smaller the self-polarization potential. Usually, the substrates are electrically connected to the sputter chamber, while the target makes the second, smaller electrode.

It is often more convenient to use a metal target instead of a ceramic target for sputtering, because a metal target has a good thermal conduction, it is easy to machine, and it can be used with a DC power supply. A reactive gas (O_2, CH_4, N_2 or H_2S, etc.) is added to the sputter gas in order to deposit oxides, carbides, nitrides or sulfides from a metal target. The chemical composition of the thin films can be varied over a wide range by adjusting the partial pressure of the reactive gas. With a titanium target, using O_2 as the reactive gas, TiO_x thin films with x ranging from 0 to 2 can be obtained, provided that the pumping speed or the gas flow rate in the installation is high enough to minimize hysteresis effects in the deposition rate and layer composition [4]. Sputtering performed in the presence of a reactive gas is called reactive sputtering. With our sputtering deposition conditions, TiO_2 thin films can be deposited by reactive DC sputtering using a titanium metallic target.

TiO_2 thin films have been produced in two different facilities. The necessity for changing the deposition equipment did not arise from scientific reasons, but from the fact that the first equipment broke down. As the design of both installations is quite different, the deposition parameters could not be transferred from one installation to the other. The characteristics of each facility are described in the following paragraphs.

3.2.2 Triode apparatus (Sputtron, Balzers)

The Sputtron equipment is designed to make depositions on several substrates at the same time. Thus the distance between the substrates and the target is relatively large, about 25 cm; it results in a low deposition rate. As shown in Figure 3.2, the substrates are placed on a rotating substrate holder in a quasi-vertical position. Among the four targets present inside the chamber, only one could be active at any given time, but it is possible to switch from one to the other without opening the chamber and so to deposit multilayer thin films. The plasma is confined with a magnetic coil and it is sustained with an auxiliary electron gun. The presence of an auxiliary anode inside the electron gun explains the term “triode” describing this kind of installation. Triode sputtering allows a lower gas pressure during the deposition and the plasma parameters are not sensitive to the power applied to the target. Infrared lamps can heat the substrates up to 320°C.

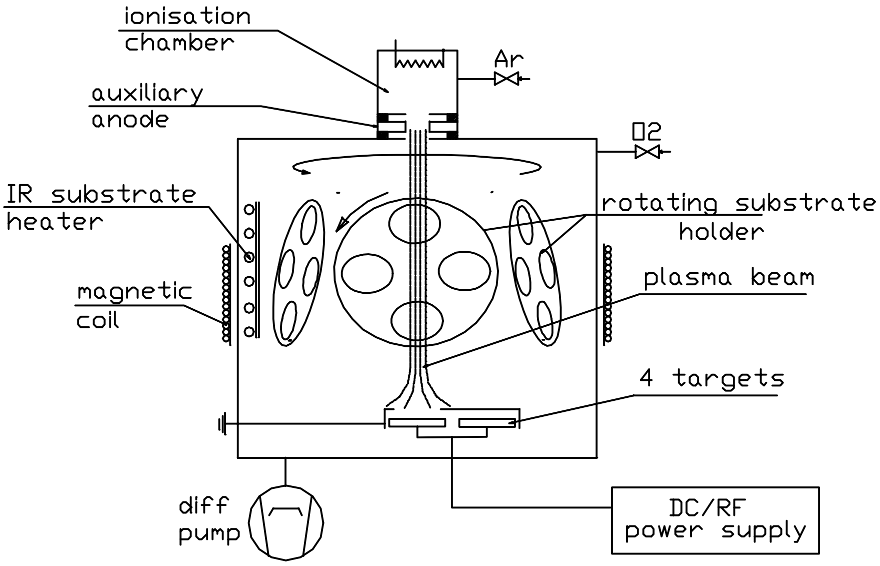

Figure 3.2: Diagram of the triode installation.

As only one target is available at any given time, a composite target was used for the deposition of TiO_2:Nb, TiO_2:Fe and TiO_2:Ce thin films. In the case of TiO_2:Nb or TiO_2:Fe, the composite target consisted of a titanium disk (purity 99.5%, 60 mm diameter) with 19 holes drilled on the front surface (Figure 3.3). The doping concentration was controlled by changing the number of holes filled with Nb_2O_5 powder (purity 99.998%) or Fe_2O_3 powder (purity 99.999%). For the deposition of TiO_2:Ce, titanium targets (purity 99.5%, 60 mm diameter) with a single hole of appropriate diameter filled with CeO_2 powder were used. RF power was required to account for the insulating character of the oxide powders.

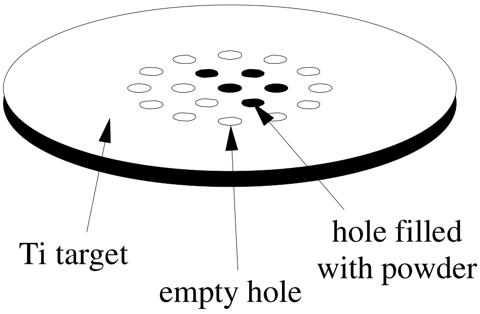

Figure 3.3: Composite target.

3.2.3 Magnetron installation (Latorus, home made)

The Latorus apparatus is a diode, magnetron sputtering system. It is called a magnetron system because permanent magnets are arranged under the target so as to create a magnetic field that confines the plasma and increases its density in the immediate vicinity of the target. The magnetic field creates a torus of plasma just above (less than 1 cm) the target as shown in Figure 3.4. It also prevents substrate heating by electrons that are efficiently confined by the magnetic field. Magnetron sputtering makes possible an increase of the ion concentration in the sputter gas and a corresponding increase of the deposition rate for a given total pressure.

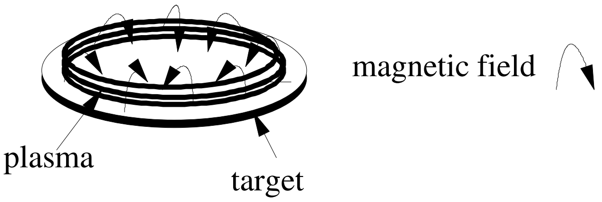

Figure 3.4: Magnetron target.

Only small substrates (max 2” in diameter) can be used in this installation, and the substrates can be replaced without breaking the vacuum inside the deposition chamber thanks to an introduction chamber (see Figure 3.5). More than one deposition can be achieved in one day. The substrates are placed in a horizontal position and the distance between substrate and target can be varied from 6 cm to 25 cm. Infrared lamps can heat the substrates up to 600°C.

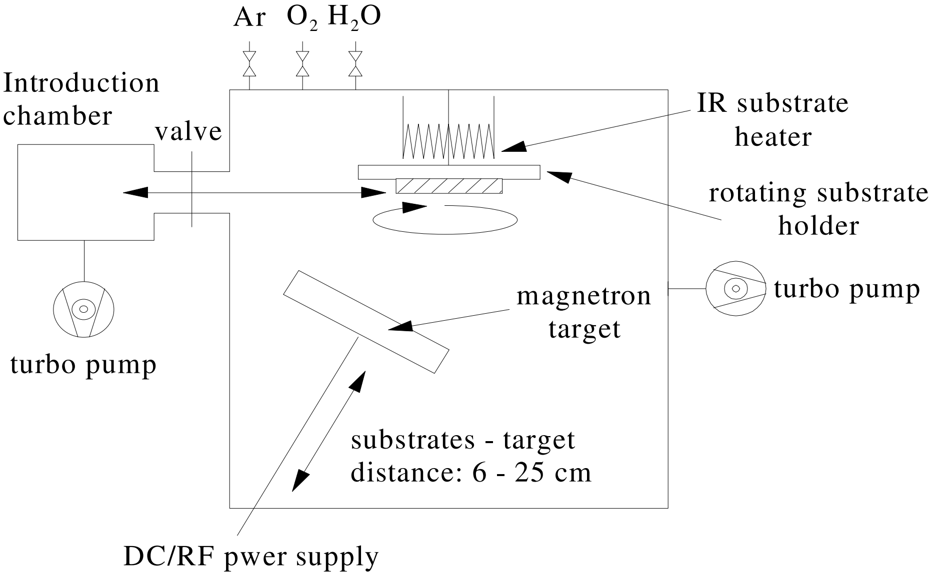

Figure 3.5: Diagram of the magnetron installation.

Doped TiO_2 films are also prepared with a composite target (titanium: purity 99.98%, 2” diameter and appropriate metal oxide) like in the triode installation.

3.2.4 Depositions parameters

When film doping was attempted by way of a target modification, a maximum number of parameters were left unchanged to highlight the doping effects. Reference undoped thin films were also deposited, and in principle only the size or the number of holes filled with oxide powders was changed. The substrate temperature was set high enough to produce polycrystalline material and low enough to obtain the anatase structure rather than the rutile structure. The minimum temperature depends on the discharge current, and on the total pressure [5-6]. The anatase phase is favored by a high partial pressure of oxygen.

TiO_2 thin films deposited in the triode installation at substrate temperatures lower than 150°C are amorphous. Generally the substrate temperature was set around 260°C. With a total pressure of 10^{-3} mbar and a RF power between 700 W and 1000 W, an Ar 78%, O_2 gas mixture was needed to obtain TiO_2. These conditions lead to mixed anatase/rutile thin films with a small fraction of anatase [Appendix C]. By increasing the oxygen concentration up to 30%, thin films are composed of the anatase phase only on most of substrates, excepted for ITO substrates, which still develop the rutile structure. In the magnetron apparatus, extensive tests led us to the parameters given in Table 3.II. The large distance between substrates and target, in the case of the triode installation, is counterbalanced by a high RF power source that maintains a sufficient deposition rate.

Table 3.II: Deposition parameters in the case of doping by target modification.

Installation	Triode	Magnetron
Total pressure [mbar]	1×10^{-3}	2.5×10^{-3}
O_2 partial pressure [%]	30	7
RF power [W]	700 - 1000	100
Substrates temperature [°C]	260 - 280	250
Substrates – target distance [cm]	25	9

The first titanium oxide thin films prepared with water vapor as reactive gas were prepared in the triode installation, shortly before its final breakdown. As a consequence, the reproducibility of the deposition procedure could not be verified. The major part of the study on TiO_{2-x} was made in the magnetron installation. At the beginning, a lot of deposition parameters had to be adjusted in order to obtain satisfactory layers, at which most parameters could be frozen. The DC current was monitored and set at value equal or less than 400 mA, as higher currents would damage the target. The total gas pressure was as low as possible to maintain a plasma discharge (2.5 x 10^{-3} mbar) in order to have parameters close to those of the triode installation. The main variations concerned the water vapor partial pressure and the substrate temperature (see Table 3.III).

Table 3.III: Deposition parameters with water vapor as reactive gas.

Installation	Triode	Magnetron
Total pressure [mbar]	1 x 10^{-3}	2.5 x 10^{-3}
H_2O partial pressure [%]	0 – 30%	0 – 100%
Source supply	RF: 700 – 1200 W	DC: 300 – 400 mA
Substrates temperature [°C]	260 - 280	20 - 300
Substrates – target distance [cm]	25	9

More detailed deposition parameters will be given in the chapters 5 and 6 for each type of thin films.

3.3 Thermal evaporation: contact deposition

Particles of the material to be deposited can sometimes be obtained by evaporation. The material is placed in a crucible that can be heated, by the Joule effect for example, to a temperature higher than its boiling or sublimation point (see Figure 3.6). The chamber is evacuated to a pressure of the order of 2 x 10^{-6} mbar to preserve the purity of material deposited. If a patterned deposition is needed, a mask in the form of a metal sheet with appropriate cutouts is placed close to the substrate.

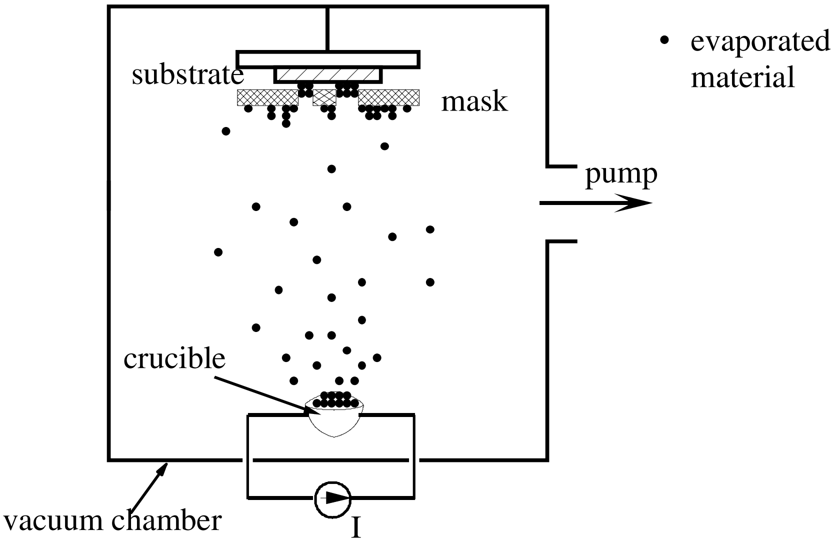

Figure 3.6: Thermal evaporation diagram.

Gold or aluminum electrical contacts were deposited by thermal evaporation.

Bibliography

[1] K. Wasa, and S. Hayakawa: “Handbook of sputter deposition technology”, Noyes Publications, New Jersey (1992).

[2] M. Ohring: “The materials Science of Thin Films”, Academic Press, San Diego (1992).

[3] S. M. Rossnagel, J. J. Cuomo, and W. D. Westwood: “Handbook of plasma processing technology”, Noyes Publications, New Jersey (1990).

[4] E. Kusano, Journal of Applied Physics 70 (1991), 7089.

[5] D. Wicaksana, A. Kobayashi, and A. Kinbara, Journal of Vacuum Science and Technology A 10 (1992), 1479.

[6] P. Löbl, M. Huppertz, and D. Mergel, Thin Solid Films 251 (1994), 72.

Chapter 4

Thin film characterizations

Each sample was characterized, first of all, by its chemical composition and its structure. The electrical properties were then investigated, since one of the goals of this work was to modify and stabilize the electrical conductivity of TiO_2. Finally, optical measurements provided useful information on phase composition and morphology, and on the electrical carrier concentration and its spatial distribution.

This chapter gives a rapid overview of the analysis techniques used to characterize our titanium oxide thin films.

4.1 Chemical composition

A rough estimate of the chemical composition of titanium oxide can be obtained by judging its color. When the ratio x in TiO_x varies from 0 to 2, the thin films display the following colors: gray, golden yellow, brown, black, dark blue and transparent [1]. Purple and blue colors can appear in thin films exhibiting a chemical composition gradient. Quantitative, bulk, chemical analyses were carried out by electron probe x-ray microanalysis (EPMA). Surface chemical bonding analyses could be obtained with x-ray photoemission spectroscopy (XPS). The presence of light atoms, hydrogen for example, was investigated with secondary ion mass spectroscopy (SIMS).

4.1.1 Electron probe x-ray microanalysis (EPMA)

Electron probe microanalysis is based on the measurements of characteristic x-rays emitted from a small region of a solid specimen bombarded by a beam of accelerated electrons. The characteristic x-ray photons, which are specific of the atomic number of the emitting atoms, are analyzed in EPMA. The photon energy identifies the emitting element, and after some corrective calculations and comparison with standards, the geometry of the volume emitting the characteristic photons can be defined, and in turn the concentration of the emitting atoms can be determined [2]. With incident electrons of 12 keV, the measured volume is about 1 $(\mu m)^3$ with a depth penetration around 700 nm, which is larger than the thickness of most thin films prepared in this work. The measured chemical composition is therefore a value averaged over the whole film thickness.

The chemical composition was analyzed on samples deposited on silicon substrates. To avoid electrical charging during the measurement, a thin carbon layer (200 Å) was deposited on top of the sample. Dr. François Bussy performed the measurements on a CAMECA SX50 installation at the Institute of Mineralogy, University of Lausanne, Switzerland. Si, Ti, O, Nb, Ce, Fe, and F atoms were quantified with the following standards: bare silicon substrate, rutile (TiO_2), β niobium oxide (Nb_2O_5), cerium phosphate ($CePO_4$), hematite (Fe_2O_3), and topaz (Al_2 Si O_4 (F O $H)_2$). A model was used to take into account the fact that the samples are thin films and to remove the silicon substrate contribution [3].

4.1.2 X-ray photoelectron spectroscopy (XPS)

Photoelectron spectroscopy is based on the measurement of the energy of electrons emitted from a surface bombarded by a beam of x-rays [4]. Like in the EPMA technique, each atom has its own signature. One of the most important capabilities of XPS is its ability to measure shifts in the binding energy of core electrons resulting from a change in the chemical environment of the emitting atom. In this way the degree(s) of oxidation of each atomic species can, in principle, be measured. The depth penetration of this chemical analysis is only a few nanometers, thus surface contamination and surface oxidation have a great influence on the results and samples must be carefully prepared to obtain valuable informations.

The XPS studies were performed on samples deposited on silicon using a SCIENTA ESCA 300 system equipped with a rotating anode, Al K_α x-ray source, an x-ray monochromator, and a hemispherical electron energy analyzer.

4.1.3 Secondary ion mass spectroscopy (SIMS)

In secondary ion mass spectroscopy, an energetic beam of focused ions is directed at the sample surface in a high vacuum environment. The transfer of energy from the impinging primary ions to the sample surface causes the sputtering of surface atoms and molecules. Some of the sputtered species carry positive or negative charges; they are called secondary ions. The secondary ions are mass analyzed using a mass spectrometer. This method can detect many trace elements and is sensitive to isotopes. For example, hydrogen and deuterium can be separated. SIMS is a destructive analysis technique [5].

The purpose of our secondary ion mass spectrometry (SIMS) analysis was the quantification of the residual hydrogen content. The measurements were performed at the Materials Department, EPFL, by Dr D. Léonard with a time-of-flight-SIMS spectrometer.

4.2 Structure and morphology determination

Thin films deposited by sputtering are made of small grains that can be crystalline or amorphous. The size, shape and stacking of the grains are part of the film morphology. For example, the films may show a compact or a columnar structure depending on deposition parameters like reactive gas pressure or substrate temperature [6]. X-rays diffraction was used to determine if the film is amorphous or polycrystalline. X-rays diffraction also gives information on grain size and phase composition. Atomic force microscopy was used to describe the film morphology with more details.

4.2.1 Film thickness

The thin film thickness was measured with an Alphastep 500, Surface Profiler (Tencor Instruments). The profiler scans a tip over the sample surface while recording its vertical position. The tip is pressed on the surface with a constant force. Measurements paths included sections on the bare substrate, which were under the mask during the deposition, and sections covered by the thin film. The film thickness is the average over 3 or 4 measurements.

4.2.2 X-ray diffraction

This technique uses the diffraction of x-rays by core electron of atoms. If the sample is a crystal, x-rays are diffracted only in directions verifying the Bragg condition:

$$2d\sin\theta = n\lambda$$

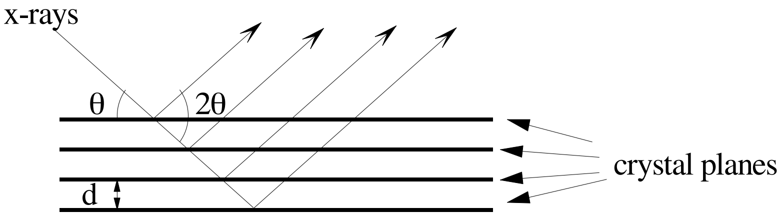

where d is the distance between crystal planes, θ the incidence angle, n an integer, and λ the wavelength of the x-rays.

In the case of our samples, which are polycrystalline thin films, measurements were made with a monochromatic x-ray beam. The diffraction angle 2θ was varied in an appropriate range and the diffracted intensity was recorded as a function of 2θ.

In principle, each crystal has is own signature: the position of the peaks depends on the crystal symmetry and on the size of the elementary cell of the lattice. Crystalline phases present in a sample can be identified by comparison with x-ray diffraction curves compiled in standard databases [7]. The shape of each Bragg peak results from a convolution of the crystallite size, of the experimental resolution function, and of internal stress. If we assume that stress is weak and if the resolution of the setup is good enough, the size can be calculated from the full width at half maximum (FWMH) of the peak with the Scherrer equation [8]:

$$\text{Size} = \frac{0.9\,\lambda}{width\,\cos(\theta)}$$

where $width = \sqrt{\text{FWMH}^2 - \text{GW}^2}$ in radian, and GW is the diffractometer broadening.

In mixed anatase-rutile TiO_2 thin films, the weight fraction W_a of the anatase phase was estimated from the relation:

$$W_a = \frac{1}{1 + 1.265\,\frac{I_R}{I_A}}$$

proposed by Spurr [9], where $\frac{I_R}{I_A}$ is the ratio between the most intense rutile peak ((110), $2\theta = 27.438$) and the most intense anatase peak ((101), $2\theta = 25.281$).

Measurements were performed on a Rigaku diffractometer, with a Cu X-ray tube (Cu K_α wavelength 1.54246 Å). Two types of diffraction configurations were used: grazing incidence and θ-2θ. In the first case, the angle between the thin film surface and the incident x-ray beam was kept constant at a low value, 5° typically. In the second case, the angle between the thin film moved in such a way that only reflections from atomic planes parallel to the film surface were measured.

4.2.3 Atomic force microscopy (AFM)

Atomic force microscopy is based on forces between two solids at atomic distances. In contact mode, a cantilevered tip is carefully brought into close vicinity of the sample, and when it is close enough, the cantilever bends. An optical system (comprising a laser and position detectors) coupled with piezoelectric motors keeps the tip at the same bending angle while the surface is scanned by moving the tip across the sample in a TV frame fashion. In this way a topographic image of the surface is obtained. In the non-contact mode, the tip is forced to vibrate at a resonant frequency. When the tip is close enough to the sample surface, the vibration is damped and its amplitude decreases. The tip is moved in such a way that the damping remains constant during the scan of the surface [10].

The morphology of our thin films was investigated by atomic force microscopy (AFM) with a “Topometrix AFM” by Dr. Christophe Ballif, Dr. Rosendo Sanjinés, and Dr. Cécile Zakri of our institute.

4.3 Electrical properties

Electrical impedance can be measured as a function of several parameters like temperature, applied voltage, atmosphere surrounding the sample, etc. Each type of measurement gives complementary information about the sample, providing that the electrical contacts are well defined. The contact material and the contact geometry must be chosen to minimize the contact contribution to the impedance of the system unless the object of the study is the contact itself. The contacts must remain stable during the measurement, especially when the sample is heated, since heat will accelerate diffusion or oxido-reduction processes. Gold is stable on TiO_2 regarding thermal treatments and it is easy to evaporate, thus most of the electrical measurements made use gold contacts. In some cases, aluminum replaced gold when the electrical barriers appearing between gold and titanium oxide had to be avoided. The electrical conductivity σ of the thin films studied varies between 10^{-10} S m^{-1} and 10^{6} S m^{-1}, so it was impossible to use the same contact geometry for all the samples.

When conductivity was less than 10^{-1} S m^{-1}, a transverse geometry was adopted (see Figure 4.1). The back contact was an indium-tin oxide (ITO) layer and typically the top contact surface S was 2 mm^{2}. In this geometry, electrical shorts could develop through pinholes, thus some 30 top contacts were deposited on each sample and measurements were carried out on the contacts that showed the highest resistance. An increase of the film thickness decreases the percentage of shorted samples. A thickness of 300 nm is a good compromise between deposition time (~3 hours) and shortcut prevention.

When conductivity is higher than 10^{-1} S m^{-1}, a coplanar geometry was used. To avoid contact contributions, a four-point geometry, either square or “Van der Pauw”, was used instead of two-point measurements. In this way, ideally, voltage was measured without current going through the voltage contacts, eliminating contact artifacts. In the case of four-point in a square geometry [11], contacts must be located far enough from the edges of the sample, whereas with Van der Pauw measurements, point contacts must located along the edge of the sample [11-12].

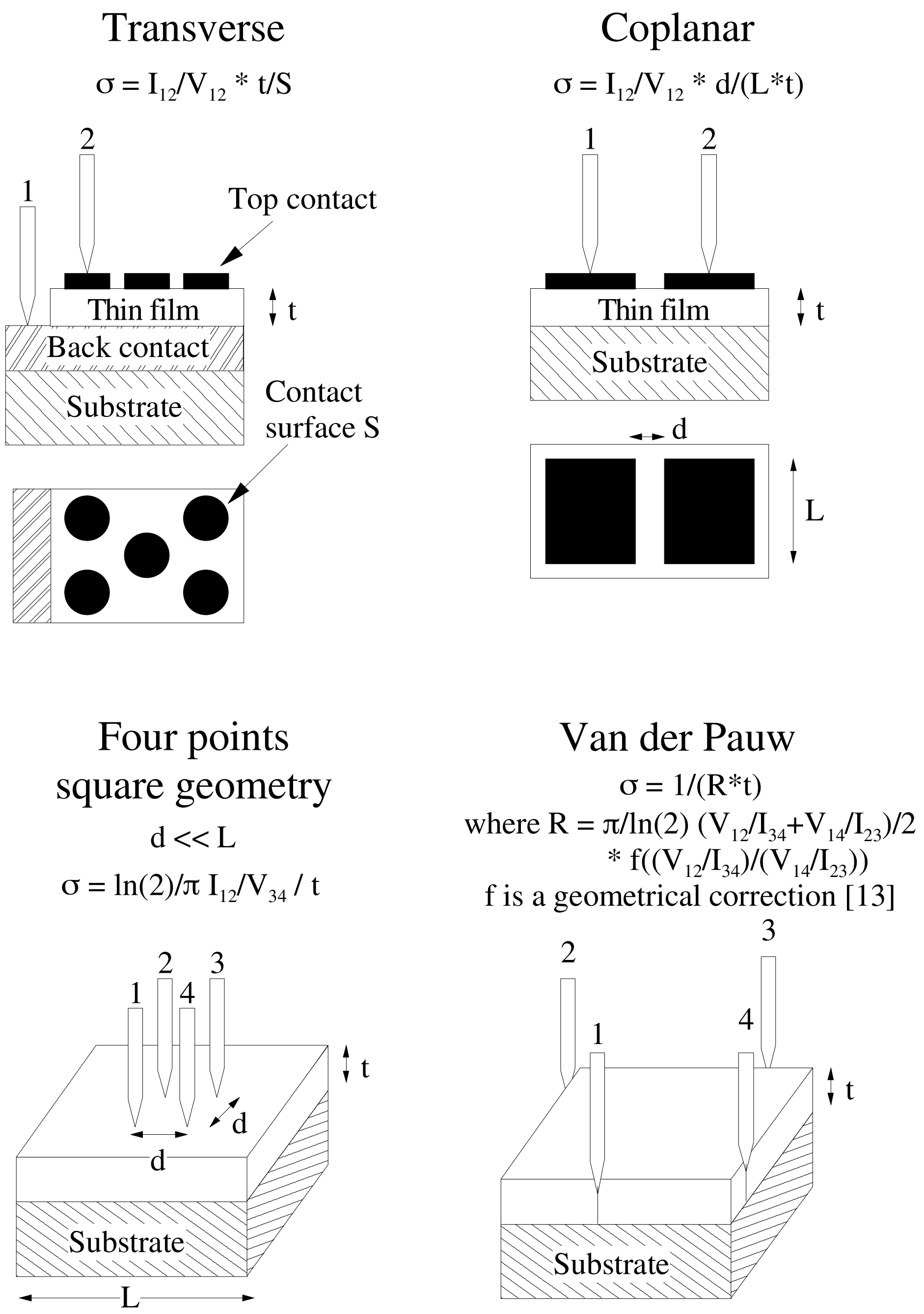

Figure 4.1: Geometry used for electrical measurements.

4.3.1 Current-voltage measurement

Current-voltage (I-V) characteristics are mainly used to characterize the electrical interactions between the electrical contacts and the sample to be measured. Metal-semiconductor contacts are typically Schottky barriers. If the barrier is high, the contact impedance is high when the contact is reverse polarized. If the barrier is sufficiently low (less than 500 meV at room temperature) the contact behaves like a linear resistor for both polarizations. Information on the barrier height can be obtained from I-V curves. When the semiconductor is highly resistive, non-linear, power-law I-V curves are often observed, which indicate various forms of carrier injection [13]. If the sample resistance is high enough, the contact resistance can be neglected. When Schottky contacts are formed, the barrier height between the metal and the semiconductor can be determined from the current/voltage measurements [14].

4.3.2 Temperature dependence of the conductivity

The evolution of the conductivity of the thin film as a function of temperature gives information on the conduction mechanisms. In the case of a metal, the electrical conductivity decreases when the temperature increases, while in the case of a semiconductor, the reverse phenomenon usually occurs. Donor or acceptor energy levels of impurities incorporated into a semiconductor material can be determined from the temperature dependence of the electrical conductivity (see Chapter 2).

4.3.3 Impedance spectroscopy

Measurements of electrical impedance as a function of frequency allow the determination of certain contact properties, and, with the help of models, of certain characteristics of polycrystalline or multi-phase samples, in particular the effects of grain boundaries [15].

4.3.4 Seebeck effect

When a sample is submitted to a temperature gradient, an electrical potential develops between the cold and the hot regions. This is called the thermoelectric or Seebeck effect [14]. The sign of the electrical potential is connected to the sign of the charge carriers and the amplitude is proportional to the temperature difference. To determine if the charge carriers are electrons or holes, qualitative measurements were made on thin films deposited on glass. The samples were placed on a heater in a way appropriate to establish a temperature gradient (see Figure 4.2). A thermal gradient of up to 25°C/mm could be obtained in this way over a distance of 2 mm. Layers with low conductivity were heated up to 350°C to decrease their resistance and to stabilize the voltage measurement.

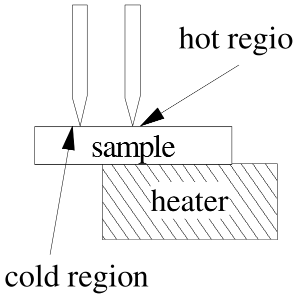

Figure 4.2: Geometry for Seebeck effect measurements.

4.4 Optical properties

With respect to the electronic properties of the sample, the optical properties in the near-infrared, visible, and ultra-violet ranges are a rich source of information. The infrared properties are sensitive to the free carrier concentration. In the far and middle infrared they reflect the vibrations of the atoms of the material (phonons), and also electronic transitions involving impurity levels. In the visible and UV range, interband transitions are predominant. For certain specific applications, the color is an important property of the thin film, for instance for transparent, conductive coatings or decorative coatings. It is necessary to quantify the light transmission, absorption, and/or reflection in order to gain insight into the electronic properties of the material.

4.4.1 Transmission and reflection

For transmission measurements, the sample (including the substrate) must be sufficiently transparent. In the infrared range, silicon wafers with both side polished were chosen, while glass (quartz) was used in the visible (ultra-violet) range. For reflection measurements, any substrate can be used. The determination of the optical constants, i.e. the refraction index *n* and the absorption coefficient *k*, requires a measurement of both transmission and reflection coefficients and a good knowledge of the sample structure (substrate optical properties, film thickness, film roughness,…).

Measurements in the near-infrared range (5000 cm^{-1} to 400 cm^{-1} or 0.05 eV to 0.62 eV) were performed on a Perking-Elmer 983G photospectrometer. For the near-infrared, visible and ultra-violet range (0.5 eV to 6 eV), a Cary-2300 UV-VIS-IR spectrophotometer was used.

Bibliography

[1] G. V. Samsonov: “The Oxide Handbook”, IFI/Plenum, New York, 2nd edn. (1982).

[2] K. F. J Heinrich, and D. E. Newbury: “Metal Handbook, volume 10: Materials characterization”, Chapter: “Electron probe X-Ray microanalysis”, American Society for Metals, Ohio, 9th edn. (1986).

[3] Software: “SAMx_Stratagem V1.3, Surface layers analysis”.

[4] J. B. Lumsden: “Metal Handbook, volume 10: Materials characterization”, Chapter: “X-ray photoelectron spectroscopy”, American Society for Metals, Ohio, 9th edn. (1986).

[5] C. G. Pantano: “Metal Handbook, volume 10: Materials characterization”, Chapter: “Secondary ion mass spectroscopy”, American Society for Metals, Ohio, 9th edn. (1986).

[6] R. F. Bunshah: “Deposition technology for films and coatings”, Noyes Publications, New Jersey (1982).

[7] Standard CPDS X-ray diffraction spectra database.

[8] P. Scherrer, Gött. Nachr 2 (1918), 98.

[9] R. A. Spurr, and H. Myer, Analytical Chemistry 29 (1957), 760.

[10] C. Ballif: “Propriétés électriques et optiques de couches minces de WS_2 et MoS_2 en vue d’applications photovoltaïques”, Thèse EPFL N° 1787, Lausanne (1998).

[11] W. R. Runyan: “Semiconductor and instrumentation”, Chapter 3: “Resistivity and carrier-concentration measurements”, Tosho Printing, Tokyo (1975).

[12] L. J. van der Pauw, Philips Research Reports 13 (1958), 1.

[13] M. A. Lampert and P. Mark: “Current injection in solids”, Academic Press, New York (1970).

[14] S. M. Sze: “Physics of Semiconductor devices”, Wiley, New York (1981).

[15] J. R. MacDonald: “Impedance spectroscopy”, John Wiley & Sons, New York (1987).

Chapter 5

Doping by target modification

This chapter discusses the effect of different impurities incorporated into TiO_2. Firstly, an explanation for the choice of the impurities studied will be given. Secondly, measurements on n-type, insulating, and p-type TiO_2, obtained with niobium, cerium, and iron doping respectively, will be presented. It will be shown that the introduction of impurities does not only give rise to donors and acceptors, but also changes the oxygen vacancy concentration in TiO_2 and the thin film structure. The electrical conductivity is the result of all these effects together.

5.1 Choice of the impurities

We are not only interested in the value of the electrical conductivity but also in its stability with respect to temperature cycling. For this reason, it is necessary to understand in detail the effects of doping with respect to electronic transport and morphology. These mechanisms are complex and complementary measurements are required, such as structural determination and chemical analysis. Only a small number of impurities could be studied in the time available for this study. The choice is large among all the possible atoms of the periodic table and one has to find selection criteria. The lack or abundance of reports available in the literature on a given impurity is not always an indication of potential usefulness of that particular dopant. For instance, germanium doping is reported to leave the TiO_2 resistivity unchanged [1]. Ge appears in the quoted article not for itself, but for the purpose of a comparison with Mg, Sb, Ta, and W doping. In our case, we dealt with thin films of TiO_2 deposited at temperature below 300°C in order to obtain the anatase phase of TiO_2. Anatase has a higher electronic mobility than rutile. Contrarily to the rutile phase of TiO_2, anatase has been much less studied until now, and little has been published on the doping of anatase. It would be interesting to obtain samples with different electrical characteristics, for example TiO_2 with a high n-type electrical conductivity, and TiO_2 with a high p-type electrical conductivity, provided that these properties are stable in time.

The effect on conductivity of residual impurities present in metallic titanium should, in particular, be understood if applications are considered. The chemical composition of two grades of titanium used as targets in the sputtering facilities is given in Table 5.I. In both cases, the major impurity is iron. The most common oxidation state of iron is +3 and in this oxidation state, its ionic radius of 0.64 Å is close to the ionic radius of Ti^{4+} (0.68 Å). Thus, if a Fe atom replaces a Ti atom, it could act as an acceptor just like the aluminum atom (see Chapter 2) and produce p-type TiO_2. Moreover, few studies have been realized on Fe-doped TiO_2 and most of them present measurements at high temperature on rutile or on single crystals [2-7]. For these reasons, iron was selected to prepare p-type TiO_2, although aluminum [8-10], chromium [11-13] or manganese [14] could also be good candidates.

Table 5.I: Typical impurity concentration in titanium targets

Atom	Ti grade 2 (99.5%) [15] Weight percent max	Ti 99.98% pure [16] ppm
Fe	0.30	95
O	0.25	-
C	0.1	-
N	0.03	-
H	0.015	-
Al	-	10
Si	-	10

In order to fabricate n-type TiO_2, we decided at first to use niobium: this impurity is one of the most often atom used to improve electrical properties of TiO_2 under all possible shapes (crystal, ceramic, thin films,…) [17-19]. We show below that the search for higher n-type conductivity can follow another route, which will be extensively described in Chapter 6. For this reason, the study of niobium doping was relatively limited compared to the other dopants investigated.

As was mentioned earlier, if TiO_2 is to be useful in applications, it has to be stable with respect to thermal cycling. Undoped TiO_2 does not fill this condition since it will loose or gain oxygen atoms when heated, and consequently change its conductivity. Doping with cerium was investigated with the purpose of obtaining TiO_2 thin films with stable insulating properties. This atom has the same most common oxidation state +3 as iron, but the Ce^{3+} ionic radius (1.13 Å) is much larger than the Fe^{3+} ionic radius (0.64 Å). As we will see, this size difference has the consequence that TiO_2:Ce becomes amorphous at high Ce concentration, and at the same time it becomes a stable insulator. Cerium doping will emphasize the importance of structure modification on the electrical conductivity of TiO_2. It is not possible to think in the same way as in the case of doping of monocrystalline silicon because high impurity concentrations are needed to exceed the native oxygen vacancy concentration and therefore modify the TiO_2 electrical conductivity. Such high impurity concentrations, which are beyond the solubility limit in the bulk material, have strong consequences on the structure and morphology of TiO_2 thin films.

5.2 Niobium-doped titanium oxide

5.2.1 Deposition parameters

Nb-doped TiO_2 thin films were prepared by reactive sputtering in both the triode and the magnetron facilities. The deposition parameters are reported in Table 5.II. Gold dots (2 mm^2) were evaporated on top of the film as electrical contacts. Electrical measurements were carried out in this transverse geometry (ITO / TiO_2:Nb / Au).

Table 5.II: TiO_2:Nb deposition parameters.

Facilities	RF power [W]	Substrate temperature [°C]	Nb concentration (at.%)
Triode	900	280	0
Triode	800	280	estimation 0.3
Triode	800	280	estimation 0.6
Magnetron	100	250	2.9

For more details, see chapter 3.

The Nb concentration of samples deposited in the triode installation is an estimation because no silicon substrates were used during these depositions, thereby preventing the EPMA analyses. The electrical conductivity of thin films deposited in same conditions, for which chemical analyses were available, could not be determined because all the contacts were electrical shorts. Shorts occur through pinholes, which were numerous in these samples. The deposition of many small contacts (~30 for each samples) reduced this problem, but it was not always successful.

5.2.2 Structure and oxidation state

The crystal structures of undoped TiO_2, niobium-doped TiO_2, and bare ITO, determined by x-ray diffraction, are reported on Figure 5.1. As expected, anatase is the dominant phase, (80 weight %) in undoped TiO_2 deposited on ITO, the average anatase crystallite size, determined with the Scherrer formula, is 22 nm, while the rutile crystallite size is smaller (10 nm). The weight fraction of anatase in thin films deposited on ITO increases as the film thickness increases [20]. The rutile-like structure of SnO_2, which is present in ITO, is likely to be at the origin of the nucleation of the rutile phase observed during the initial growth stages. With increasing film thickness, the anatase phase eventually predominates. The nucleation of the rutile phase is limited to the film/ITO interface, because it requires a high temperature to form [21]. At low Nb concentration the film structure is again anatase with the same crystallite size, while at higher concentration, the crystallite size decreases and the amount of rutile increases to 70 % of rutile with 2.9 at.% of niobium. This is consistent with the facts that niobium oxide can exhibit a rutile structure with an NbO_2 composition [22], and that NbO_2 and TiO_2 are mutually and completely soluble, forming a $Nb_xTi_{1-x}O_2$ solid solutions with the rutile structure for $0 < x < 0.85$ [23]. The NbO_2 phase has not been detected in the TiO_2:Nb samples.

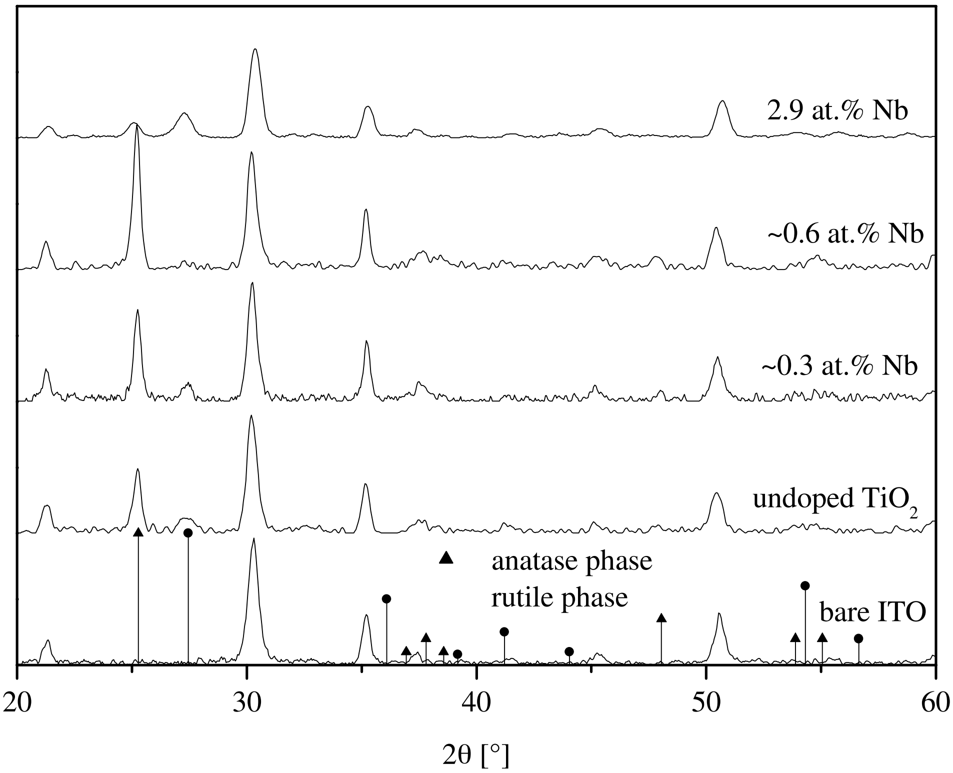

Figure 5.1: X-ray diffraction spectra of undoped and Nb-doped TiO_2 thin films.

An XPS spectrum of TiO_2:Nb is reported in Figure 5.2. The position of the Ti $2p_{3/2}$ peak (458.8 eV) is close to the value reported for Ti^{4+} (458.7 eV) [24]. As expected in TiO_2, the oxidation state of titanium is 4+. The Nb_2O_5 $3d_{5/2}$ peak can be modeled by a single gaussian peak centered at an energy of 207.4 eV. This energy is closer to the bonding energy reported in the case of Nb-doped TiO_2 deposited by molecular beam epitaxy (207 eV), than to the binding energy in the case of Nb_2O_5 prepared in the same way (208.0 eV) [19]. This indicates that niobium atoms replace titanium atoms and assume the same oxidation state of 4+ as titanium atoms. Thus they can increase the electrical conductivity as donors impurities as it shown by the following chemical reaction already given in chapter 2:

$$Nb_2O_5 \leftrightarrow 2\ Nbi_{Ti}^{\cdot} + 4\ O_O + 2\ e' + \tfrac{1}{2}\ O_2$$

Seebeck measurements confirm that Nb-doped TiO_2 is an n-type semiconductor.

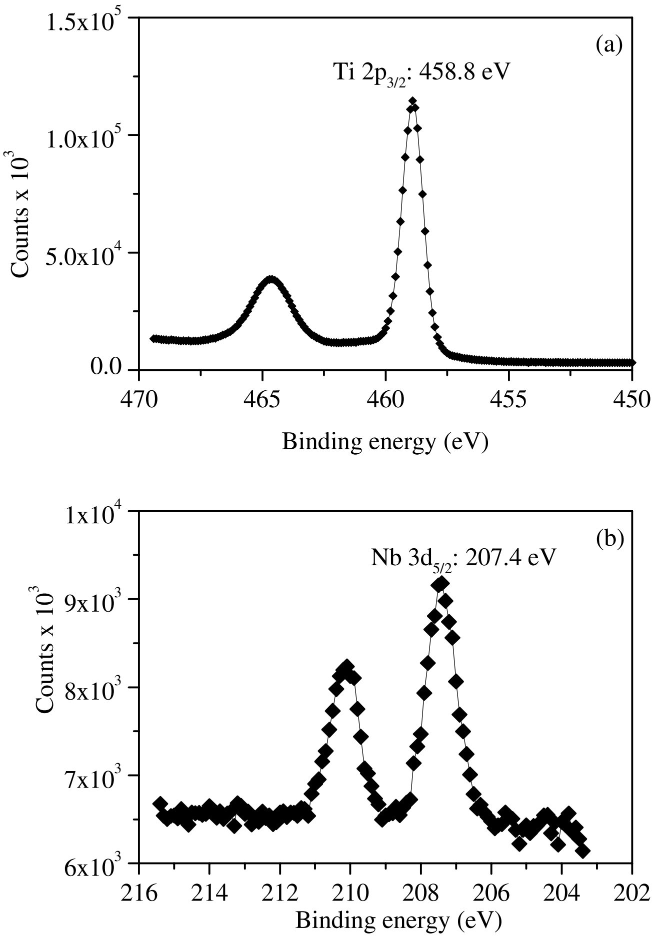

Figure 5.2: XPS spectrum of TiO_2:Nb. (a) Ti 2p core level, (b) Nb 3d core level.

5.2.3 Electrical properties

The dc electrical conductivity of undoped TiO_2 and Nb doped TiO_2 is reported in Figure 5.3. Both small polaron hopping and band conduction have been observed in TiO_2, depending on temperature and doping. Hopping conduction occurs at low temperature in poorly conducting or disordered material [25]. It is characterized by a low electron mobility, typically less than 10^{-5} m^2/Vs. In rutile TiO_2, the temperature of transition between band conduction and hopping conduction is situated around 300 K according to N. Tsuda [26]. H. Tang has shown that the conductivity of anatase thin films is due to band conduction rather than small polarons conduction [27]. In our case, the less conducting samples have the anatase structure and we can verify that the activation energy of the electrical conductivity is well defined. As the measurements were made at temperature higher than 300 K, we assume that the dc electrical conductivity is due to band conduction. Hopping type conduction could only be seen in insulating, amorphous TiO_2 sample doped with Ce which are presented in the next section. The frequency dependence of hopping and band conduction is different. The band conductivity is frequency independent, whereas the hopping conductivity is proportional to ω^p with $0 < p < 1$ and increases with frequency [28]. Depending on the temperature, if the frequency is high enough, hopping conduction can take over the electrical conductivity even if the band conduction is the dominant mechanism at low frequency.

The activation energy of undoped TiO_2 (0.65 eV) is much larger than the activation energy of shallow donor levels created by oxygen vacancies. This can be understood if we assume that intrinsic impurities produce trap or acceptor levels below the shallow donor levels of TiO_2. This intrinsic impurity is possibly iron which is always present in titanium as can be seen in chemical analyses of the targets. If we suppose that iron has a similar deposition rate as titanium [29] to simplify the calculation, 0.3 weight % in the target (the maximum expected value in the targets used in this study) correspond to 0.08 at.% in TiO_2 thin films, which is below the detection level of EPMA measurements. Iron has never been observed by EPMA in undoped TiO_2 samples. This allows an iron concentration in the range between 10^{25} and 10^{26} m^{-3}, close to the intrinsic impurity concentration inferred in reference 20. A similar compensation of the native shallow donors could also result from other impurities or complex defects such as an oxygen vacancy associated with interstitial oxygen. We do not have enough evidences to determine the origin of the trap level, but it is important to know that it exists to understand the electrical conductivity of TiO_2.

When the niobium concentration increases, the conductivity increases while the activation energy decreases. At high niobium concentration, the resulting activation energy (0.17 eV) is close to the activation energy measured in the case of ceramic TiO_2 doped with 4 at.% of niobium (0.14 eV) [17], while the conductivity is much less (1.3×10^{-3} S m^{-1} instead of 100 S m^{-1}). If we estimate the electrical conductivity with an electron mobility of 0.3×10^{-4} m^2/Vs [27], assuming that all the niobium atoms act as a donor impurities (concentration: 2.8×10^{27} m^{-3}), and assuming the same concentration of oxygen vacancies and intrinsic traps as in undoped TiO_2, we obtain a conductivity of 7 S m^{-1} at room temperature. The difference between the calculated and measured value is so important that we have to reconsider the role of niobium inside our thin films. One possible explanation could be that 99.9% of the niobium atoms are not active donors because they are located in the grain boundaries. A better explanation is that the electrons given by the niobium atoms are trapped by defects generated by the introduction of niobium into the titanium oxide structure. A model that considers each niobium atom as donor with ionization energy of 0.14 eV compensated at 99.85% by electron traps gives the conductivity represented by the solid line on the Figure 5.3 in the case of the most conducting sample. If the charge compensation required for niobium incorporation is provided by a lattice defect (interstitial oxygen or titanium vacancy) instead of electron liberation, such a trap defects is created (see Chapter 2)

$$\mathrm{Nb_2O_5} \leftrightarrow 2\ \mathrm{Nbi}^{\bullet}_{\mathrm{Ti}} + \mathrm{O}_{\mathrm{i}}^{\prime\prime} + 4\ \mathrm{O_O}$$

$$2\ \mathrm{Nb_2O_5} \leftrightarrow 4\ \mathrm{Nbi}^{\bullet}_{\mathrm{Ti}} + \mathrm{V}_{\mathrm{Ti}}^{\prime\prime\prime\prime} + 10\ \mathrm{O_O}$$

The result is an increase of the electrical conductivity respectively to undoped TiO_2, in a much less important proportion than in the case of electron emission [30]. The fact that the oxidation state of niobium, measured by XPS, is between 4+ and 5+ might indicate that interstitial oxygen is created by niobium incorporation, but a deeper investigation is necessary to prove or to disprove this statement.

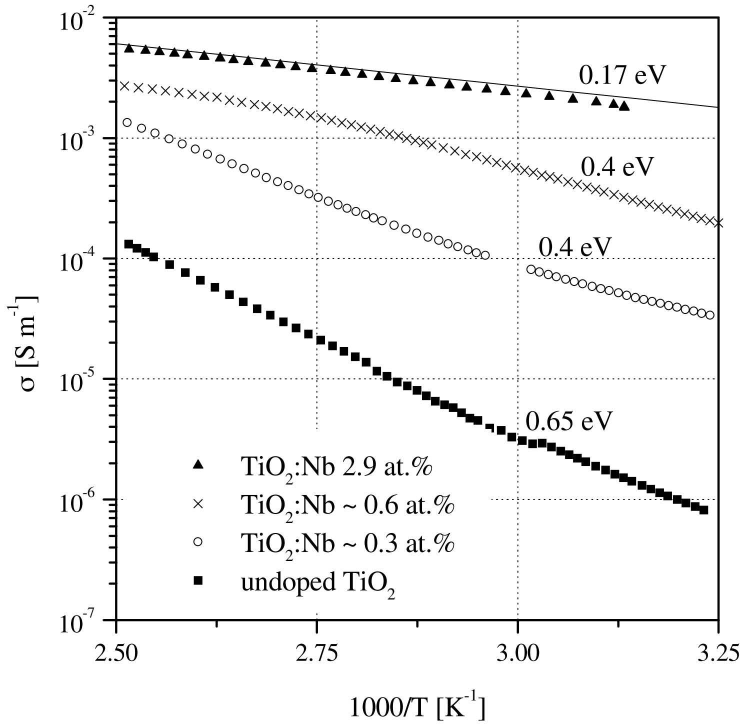

Figure 5.3: Influence of Nb doping on the DC conductivity of TiO_2 thin films. The solid line represents the calculated conductivity modeled above.

5.2.4 Summary

The investigation shows that the niobium does not act as a donor impurity only, contrary to many reports found in the literature. The incorporation of more than 0.6 % of niobium induces a phase transition from anatase to rutile, and it was shown that defects are created by the introduction of niobium atoms resulting in a conductivity much lower than the conductivity obtained in doped ceramic, where 100 S m^{-1} was measured on TiO_2:Nb with 4 at.% of niobium. Nevertheless, the electrical conductivity of undoped titanium is improved by a factor 1000 by a 2.9 at.% niobium doping.

5.3 Cerium-doped titanium oxide

For certain applications, it is important to have insulator with high dielectric constant. For example thin film electroluminescent devices (TFELD) provide an attractive alternative to solid-state, LCD, flat panel displays [31]. Dielectric materials play a decisive role in the performance of these Metal – Insulator - Semiconductor (phosphor) – Insulator - Metal (MISIM) structure. Under actual operating conditions, very high electrical fields of the order of 1-2 x 10^8 V/m are applied to the phosphor layer. The role of the dielectric is to prevent the device breakdown under these high fields and to keep charges suitably trapped in interface states so that they do not leak out into the phosphor at lower fields. Most important of all, a dielectric with high permittivity lowers the operation threshold voltage as it increases the electric field in the emitting layer for a same applied voltage. It leads to lower power consumption in both devices and addressing circuits, which in turn can be controlled by lower voltage drivers.

A number of studies have reported attempts at finding suitable dielectrics for TFELD applications having the highest figure of merit, which is defined as the product of dielectric constant and breakdown electric field $\varepsilon_O\ \varepsilon\ E_{bd}$ [32]. This figure of merit, which indicates the maximum trapped charge density for an insulator material, is of the order of 4-6 μC/cm^2 in classical TFELD [33]. Because of its high permittivity, TiO_2 is a potential candidate provided its electrical properties can be controlled. A figure of merit of only 1 μC/cm^2 has been reported corresponding to a high permittivity ε (60) but very low breakdown field Ebd (20 x 10^6 V/m) [33].

We will show that the Ce-doping improves the resistivity and stability of TiO_2. A 2.1 at.% Ce concentration leads to an increase of the resistivity of TiO_2 by a factor 300, an increase of the breakdown voltage by a factor 10, and a reduced variation of the permittivity with frequency. A frequency independent constant value between 35 and 45 is obtained for the permittivity. Electrical and structural characterization of TiO_2:Ce are discussed below, while a complete analysis of electroluminescent properties of the devices made with TiO_2:Ce is reported in references [20,34].

5.3.1 Deposition parameters

Ce-doped TiO_2 thin films were deposited by reactive RF sputtering in the triode facility. A fraction of the surface of the Ti target was replaced by compressed CeO_2 powder disks. The deposition temperature was set between 260°C and 280°C. The deposition conditions, which varied from one deposition to the next, are reported in Table 5.III. Gold or aluminum dots (2 mm^2) were evaporated on top of the film as electrical contacts. Electrical measurements were carried out in this transverse geometry (ITO / TiO_2:Ce / Au or Al).

Table 5.III: TiO_2:Ce deposition parameters.

RF power [W]	CeO_2 area / total target area [%]	Deposition Rate [Å/s]	Ce concentration [at.%]
900	0	0.50	0.0
900	1.8	0.66	0.3
1000	0.36	0.14	0.4
750	1.44	0.08	1.2
900	2.56	0.21	1.8
900	2.56	0.17	2.1

For more details, see chapter 3.

The evolution of the cerium concentration is not a monotonic function of the fractional area of the target composed of CeO_2 powder, especially for sample containing 0.3 at.% of cerium. This is not related to cerium oxide itself, but to the difference in deposition rate of each deposition. After a few hundred hours of deposition, the targets tend to deform slightly, and their temperature increases during the deposition. As a result, the total deposition rate increases, affecting mostly the deposition rate of titanium oxide. Thus the cerium concentration incorporated in the thin film decreases compared to a deposition with a lower total deposition rate. We can see that with this kind of composite target, the deposition rate is an important parameter and that a compromise between the deposition rate and the impurity concentration must be reached.

5.3.2 Structural characterization and morphology

The mixed-phase morphology of the undoped films (see Figure 5.1) is also observed on Ce-doped films deposited on ITO as long as the concentration of Ce remains below 1.2 at.%. No significant change is observed in the crystallite size of the anatase phase compared to that of undoped films. A further increase of the Ce concentration leads to an amorphization of the films. On highly Ce-doped films (>1.2 at.%), the mismatch between the ionic radii of Ti^{4+} (0.68 Å) and of Ce^{4+} (1.01 Å) or Ce^{3+} (1.13 Å) is suspected to be at the origin of the amorphization. The amorphous morphology of these films persists in spite of high-temperature thermal treatments such as rapid or long thermal annealing (RTA or LTA) up to 873 K. At intermediate Ce-doping concentrations (0 - 1.0 at.%), amorphous films can also be obtained by deposition at 373 K. Upon thermal treatment up to 673 K such films transform into pure anatase even on top of an ITO substrate.

5.3.3 DC electrical properties

The dc electrical conductivity of TiO_2:Ce (cf. Table 5.III for preparation conditions) was measured between 300 and 600 K. Its dependence on the Ce concentration is reported in Figure 5.4. Ce doping decreases the TiO_2 conductivity so that samples doped with 2.1 at.% of Ce have a conductivity 300 times lower than undoped samples. The experimentally determined activation energy of the conductivity decreases slightly from 0.65 eV for light doping to 0.60 eV for heavy doping. If Ce were acting as a simple electron trap or as a simple acceptor, the activation energy would actually increase with increasing compensation, which is contrary to observation. Since the Ce ion is much larger than the Ti^{4+} ion (1.01 Å versus 0.68 Å) it is quite unlikely that Ce can act as a substitutional impurity. For steric reasons, however, the formation of a complex defect comprising a Ce atom and an oxygen vacancy in close proximity should be energetically more favorable. The model we have developed in reference [20] can be summarize with the following chemical reaction:

$$CeO_2 \leftrightarrow Ce_{Ti}^{\prime} + V_O^{\bullet\bullet} + O_O + \tfrac{1}{2}\, O_2 + e^{\prime}$$

Kofstad has proposed several models [35] of defect equilibria in which the concentration of an intrinsic defect (here, the oxygen vacancy) becomes equal to the concentration of the extrinsic impurity.

If one assumes that the electron mobility $\mu \cong 0.3 \times 10^{-4}$ Vs/m^2 is less dependant on the temperature that the electron concentration (exponential behavior) [27], one obtains the conductivity $\sigma = q\ \mu\ n$ reported as solid lines in Figure 5.4. The numerical values are given in Table 5.IV.

The conductivity drop between polycrystalline films (Ce concentration < 1.2 at.%) and amorphous films indicates that the mobility is 3000 times lower in amorphous samples than in polycrystalline material. As expected, electronic conduction in the amorphous films appears to be a hopping process rather than a band process. The progressive decrease of the activation energy at low temperature is another telltale sign of hopping conduction [36].

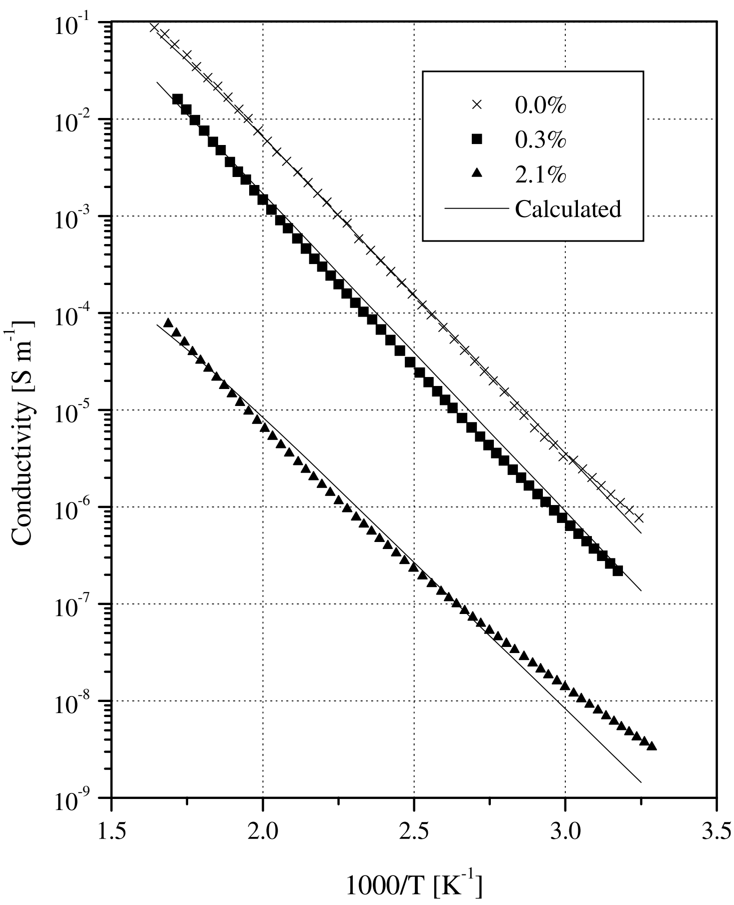

Figure 5.4: Influence of Ce doping on the dc conductivity of TiO_2 films. The solid lines represent the dc conductivity calculated using values given in Table 5.IV.

Table 5.IV: Numerical values for dc conductivity.

Ce concentration [at.% // m^{-3}]	0 // 0	0.3 // $2.6\text{x}10^{26}$	2.1 // $1.9\text{x}10^{27}$
O vacancy concentration [m^{-3}]	$1\text{x}10^{25}$	$2.58\text{x}10^{26}$	$1.9\text{x}10^{27}$
O vacancy shallow level [eV] [27]	<0.2 eV		
O vacancy deep level [eV]	0.65	0.65	0.6
Intrinsic trap concentration [m^{-3}]	$1.01\text{x}10^{25}$		
Energy gap [eV] [27]	3.20		
Mobility [10^4 m^2/Vs]	0.3	0.3	0.0001
Conduction band density of states [m^{-3}]	10^{26}		

5.3.4 Dielectric properties

The dielectric properties of Ce-doped films have been investigated in the frequency range extending from 10^2 to 10^6 Hz. The effects of the Ce concentration on the dielectric properties of an anatase (0.4 at.%) and an amorphous (2.1 at.%) films are shown in Figure 5.5. Ce doping shifts the ac conductivity towards lower values while the maximum value of the ac permittivity and the frequency dispersion of heavy doped films are much weaker than that of lightly doped films. The film with the largest Ce doping (2.1 at.%) exhibits a frequency independent permittivity. The temperature dependence of the ac permittivity and ac conductivity of heavily Ce-doped films have been investigated over the temperature range from 300 to 573 K. The results of the measurements performed on a 230-nm-thick, 2.1 at.%, Ce-doped amorphous film are shown in Figure 5.6.

The frequency dependence of the permittivity and conductivity of all the films discussed here obey a simple power law, viz. $\sigma(\omega) = \sigma_0 + \sigma_1\,\omega^p$ and $\varepsilon(\omega) = \varepsilon_\infty + \varepsilon_1\,\omega^{(p-1)}$, with $0 < p < 1$ and $\varepsilon_0\,\varepsilon_1 = \sigma_1 \tan(p\,\pi/2)$, where ε_0 is the permittivity of vacuum and σ_0 the dc conductivity. The solid curve in Figure 5.5 and Figure 5.6 represents the values obtained with this power law. This behavior is commonly observed on a wide range of insulating or poorly conducting materials [37-40]. In the particular case of $4.5TiO_{2-x}{\cdot}2P_2O_5$ glass [37], it has been shown to ensue from hopping conduction. When the Ce concentration increases, the exponent p increases from 0.65 (undoped) to 0.86 (2.1 at.% Ce). In several hopping theories [37], the increase of p at a given temperature indicates that the typical distance between hopping sites decreases. In our case, it indicates that distance between hopping sites varies like the distance between Ce impurities. The decrease of p with temperature (strong frequency dispersion at high temperature) is consistent with Springett's hopping model [37]. At high temperature, the electronic transport is dominated by conduction band conductivity that results in an almost frequency-independent resistivity. As a result, σ_1 becomes much smaller than σ_0.

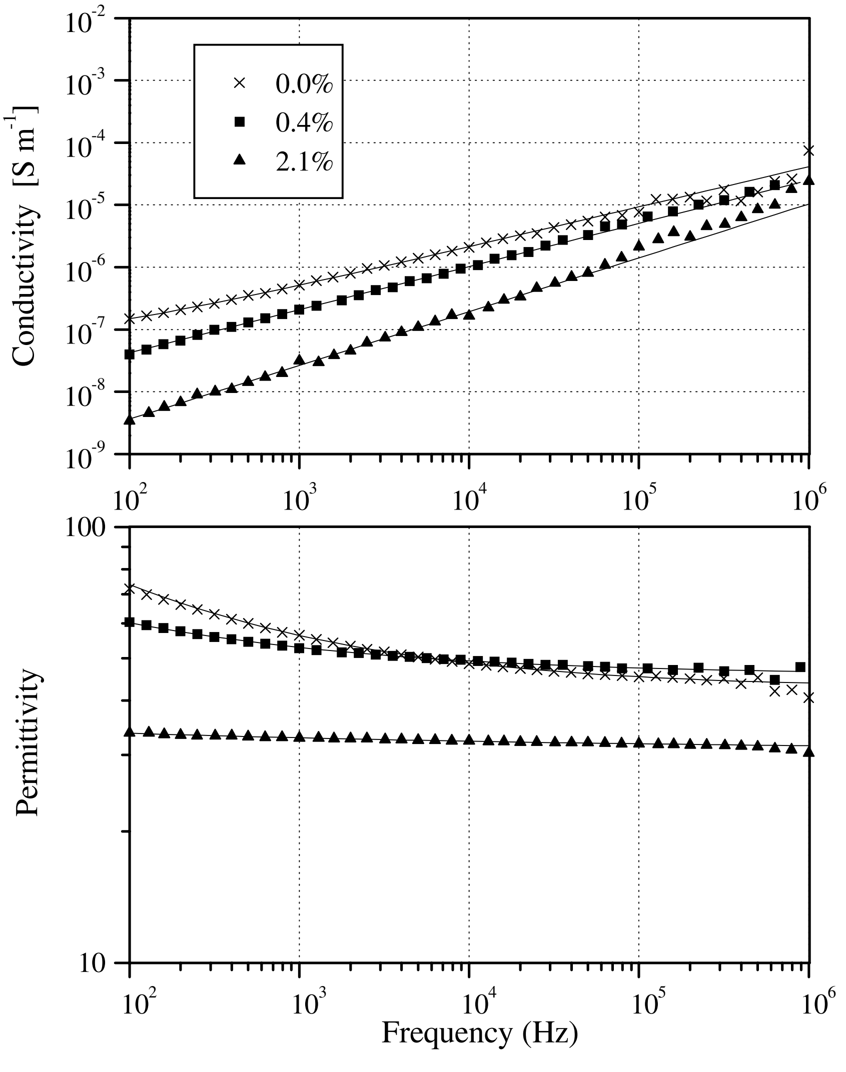

Figure 5.5: Influence of Ce doping on the dielectric properties of TiO_2 films. a) conductivity vs. frequency, b) permittivity vs. Frequency. The solid lines represent the calculated conductivity and permittivity.

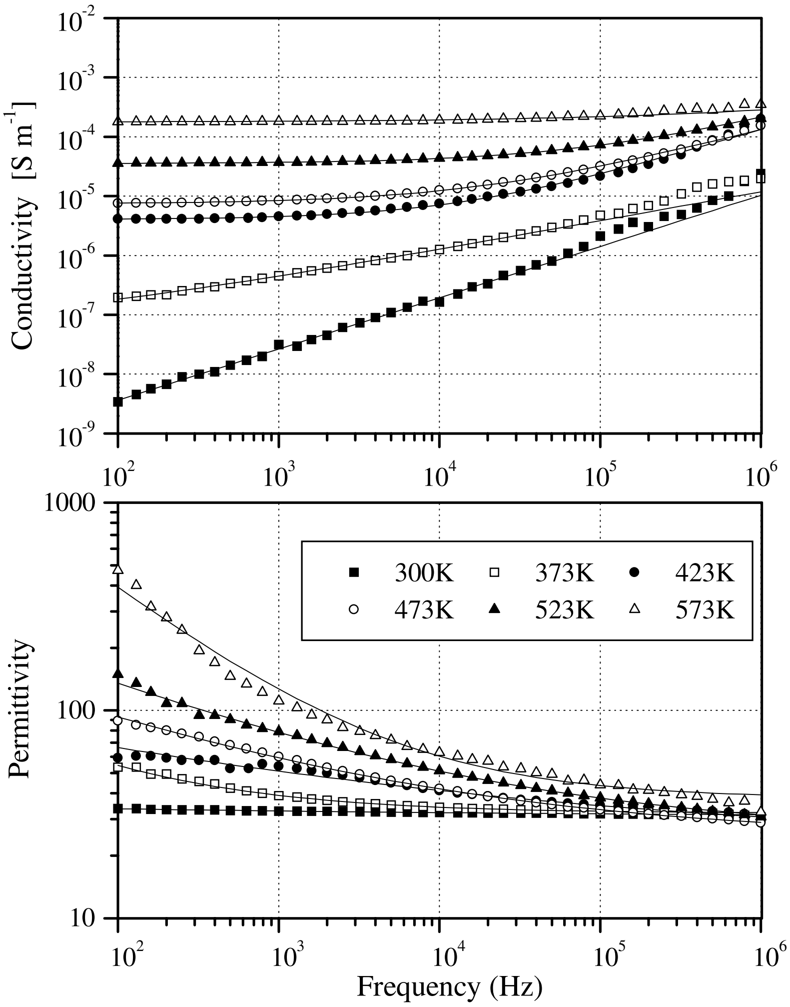

Figure 5.6: Temperature dependence of the dielectric properties of 2.1 at.% Ce-doped TiO_2 films. a) conductivity vs. frequency, b) permittivity vs. frequency. The solid lines represent the calculated conductivity and permittivity.

5.3.5 Insulator breakdown characteristics

Figure 5.7 shows the current density as a function of the electric field for TiO_2 thin films having different Ce concentrations (cf. Table 5.III for preparation conditions). In doped films the current at low fields is more than two orders of magnitude lower than in the undoped films. This confirms the higher resistivity of the doped material. The breakdown threshold is identified as the abrupt bending off (knee) of the curve at a field of about $3x10^6$ V/m. Beyond the knee an avalanche-like current increase results in a destructive breakdown of the insulator. In films containing 0.4 at.% Ce, the current at low fields is lower than in the undoped films, but the breakdown knee is not modified. A further increase in Ce concentration induces a shift of the breakdown knee towards higher electric fields: it is located at 7x10^6 V/m for films containing 1.2 at.% of Ce and above 10^7 V/m for the most heavily doped sample (2.1 at.%). The breakdown field increase is due to both the introduction of cerium traps and to the transformation from crystalline anatase to an amorphous structure. The breakdown mode depends on the metal used for electrical contacts. With Al contacts, the typical top contact used for electroluminescent devices, a propagating breakdown occurs, while with Au contacts, breakdown is self-healing. This property can be used to repair shorted devices. Using high voltage (~10 V) for a small time (~1 s), the short current path can be eliminated by Joule heating, and the remaining contact, with a smaller surface, can be used for electrical measurements.

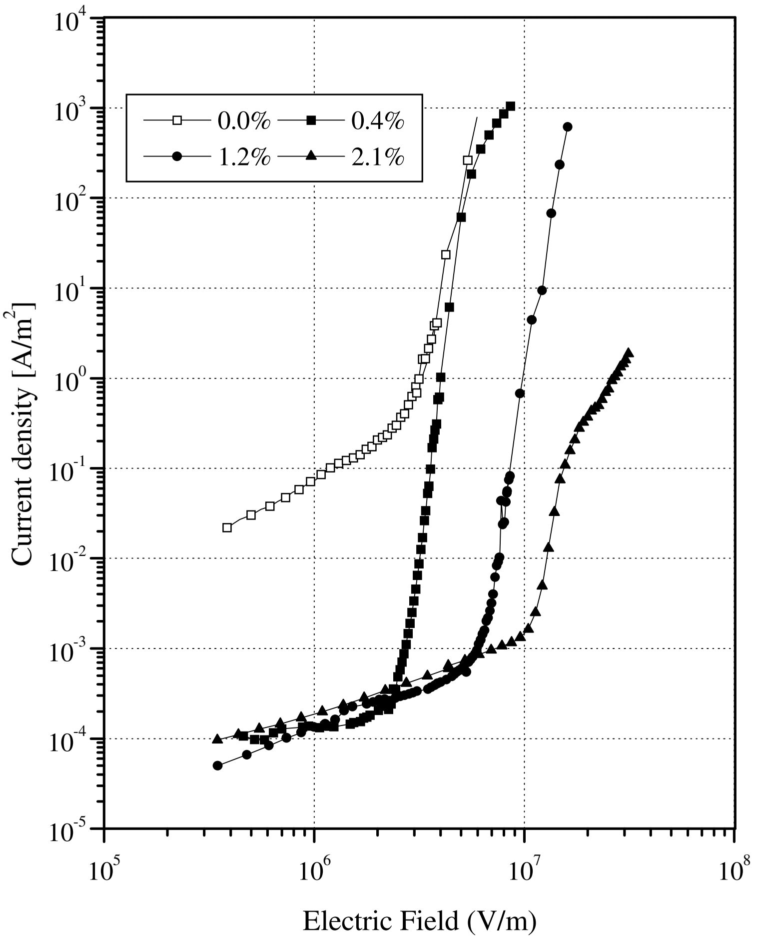

Figure 5.7: Ce-doped TiO_2 thin films. Electrical current density vs. electrical field for several levels of doping.

5.3.6 Electroluminescent devices

Electroluminescent devices using TiO_2:Ce as insulators have been prepared in collaboration with the team of Professor P. Benalloul from the Laboratoire d'Accoustique et d'Optique de la Matière Condensée at the Paul and Marie Curie University in Paris. Some results are presented in the following section, more details can be found in appendix A. A CeO_2 layer was added to the second TiO_2:Ce insulator to increase the breakdown voltage from 10^7 to 10^8 V/m, with a slight decrease of the mean dielectric constant of the second insulator to about 35. The brightness of our device is compared with a standard device in Figure 5.8. The high permittivity of the TiO_2:Ce/CeO_2 insulator compared to the Y_2O_3 insulator results in a substantial decrease of the threshold voltage for device B. In this case, the threshold voltage goes down from 88 Vrms to 40 Vrms. The highest brightness saturation of device B and the steep increase of the brightness show that the interface between TiO_2:Ce and ZnS:Mn does not leak carriers, as seen in the well-defined curve of Figure 5.8. The incorporation of a CeO_2 layer in the insulators protects the device against breakdown, so that it can be driven to brightness saturation.

device	A	B
transparent electrode	ITO	ITO
bottom insulator	Y_2O_3 330nm	TiO_2:Ce 270 nm
phosphor	ZnS:Mn 520nm	ZnS:Mn 520nm
top insulator	Y_2O_3 360nm	TiO_2:Ce 200 nm CeO_2 200 nm
reflecting electrode	Al	Au

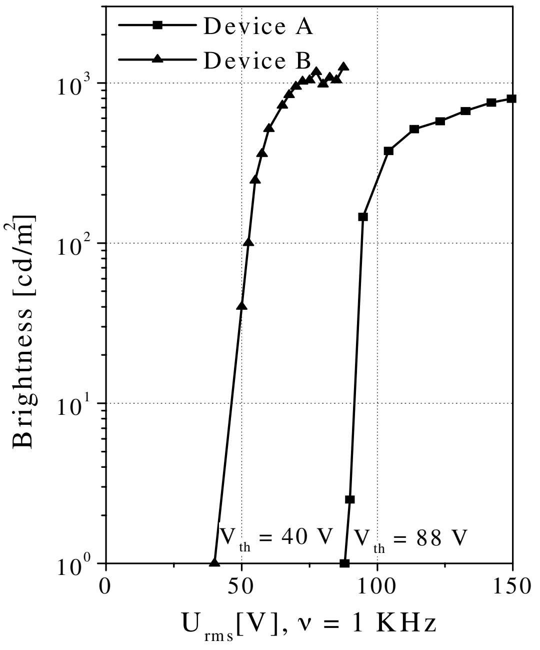

Figure 5.8: Brightness versus applied voltage for electroluminescent devices having Y_2O_3 and TiO_2:Ce as insulators.

Cerium doped TiO_2 is suitable as an insulator in electroluminescent devices. The combination of TiO_2:Ce and CeO_2 insulators have a figure of merit of 3.1 μC/cm^2 comparable to Y_2O_3 (3-5 μC/cm^2 [33]) and improve in a significant manner the luminescent properties of such devices.

5.3.7 Summary

The TiO_2 electrical properties have been stabilized and improved by cerium doping, resulting in a lower conductivity (10^{-9} S m^{-1}), a higher electrical breakdown strength (2×10^7 V/m), and a high value of the permittivity (45±5). The film structure is anatase at low doping (<1.2 at.%) and becomes amorphous for higher Ce concentration. The dc conductivity measurements show that cerium incorporation into TiO_2 has two effects. Due to the large Ce ionic radius, new oxygen vacancies are created into the oxide and electron traps are simultaneously introduced. The combination of these two effects results in a decrease of the TiO_2 conductivity with Ce doping. The ac conductivity and ac permittivity can be explained by including a hopping contribution in the electron conduction process. At high Ce concentration, the permittivity is frequency independent. The performance of TiO_2:Ce as insulator is demonstrated in the case of electroluminescent devices.

5.4 Iron-doped titanium oxide

5.4.1 Deposition parameters

Fe-doped TiO_2 thin films were prepared by reactive RF sputtering in the triode apparatus. Silicon, glass, and ITO-coated glass substrates were heated to 260°C during the deposition. The RF power was 700 W, and the deposition rate was between 0.2 and 0.4 Å/s. Table 5.V summaries the properties of the films.

Gold contacts were evaporated on top of the thin films deposited on ITO coated glass and electrical measurements were performed in a transverse geometry.

Table 5.V: TiO_2:Fe thin film properties.

name	thickness [nm]	# holes	Fe concentration [at.%]	conductivity [S m^{-1}]	E_{act} [eV]
A	300	0	0	3.15×10^{-6}	0.65
B	290	1	trace	4.11×10^{-5}	0.51
C	240	3	0.13	3.30×10^{-7}	0.59
D	290	5	0.32	4.28×10^{-9}	0.63
E	190	7	0.51	1.82×10^{-8}	0.65
F	200	9	0.72	1.81×10^{-7}	0.56
G	240	13	0.97	2.68×10^{-6}	0.54
H	350	19	1.30	3.47×10^{-6}	0.51

For more details, see chapter 3.

The dependence of iron concentration in the films on the number of holes filled with iron oxide powder in the titanium target is reported in Figure 5.9. It varies from 0.1 to 1.3 at.% in the most heavily doped sample. The concentration evolution is monotonic with the number of holes filled. The use of a lower power in the case of iron doping (700 W) than in the case of cerium doping (900 W) allow a better control of the doping concentration by preserving the target from overheating. The first part is linear and when more than 9 holes are filled, the resulting iron concentration increases more slowly. This can be explained by the fact that the holes are filled from the center to the edge of the target and that the plasma is denser in the center of the target. Therefore, the contribution of the outside holes during the deposition is less important.

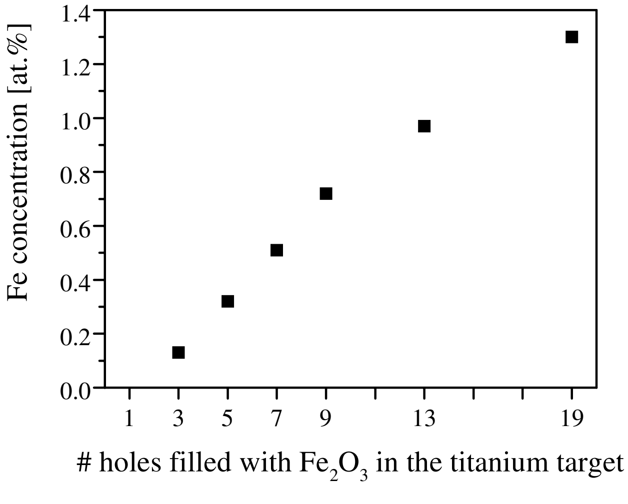

Figure 5.9: Iron concentrations vs. number of holes filled in the titanium target.

5.4.2 Structural characterization and morphology

The thin film structure was investigated by x-ray diffractometry in a θ / 2θ angle configuration. X-ray diffraction spectra (Figure 5.10) reveal the influence of Fe doping on the structure of the TiO_2 thin film. For Fe concentration lower than 0.32 at.%, the rutile phase is not present in the films. When the Fe concentration increases, the weight percentage of the rutile phase becomes more and more important, it reaches 60 % for the sample with 1.3 at.% Fe, that are the thicker samples (see Table 5.V), thus the fact that the rutile phase is the most important in these samples is not due to the influence of the ITO substrate. The increase of the rutile phase weight percentage is accompanied by a decrease of the anatase grain size. Values calculated with the Scherrer formula applied on the most intense anatase peak (110) (shown in Figure 5.10), indicate that the crystallite size decreases from 22 to 11.5 nm. No tendency to amorphization has been observed with Fe doping, whereas samples doped with more than 1.2 at.% Ce are consistently amorphous (see chapter 5.3). This can be explained by the fact that the Fe^{3+} ionic radius (0.64 Å) is close to the Ti^{4+} ionic radius (0.68 Å). The transformation from the anatase to the rutile structure with Fe doping is consistent with Bregani's observations [41], who noted that impurities like Cu, Mn, Cd, Fe, Co, Zn favor the transformation from anatase to rutile structure.

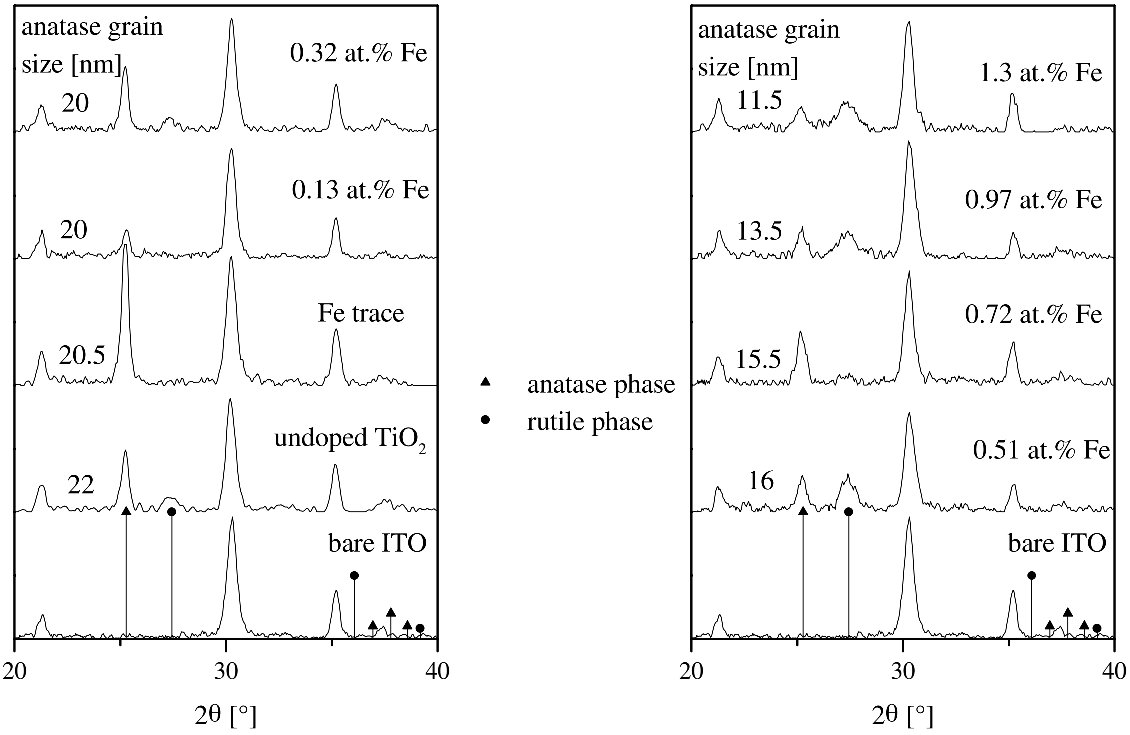

Figure 5.10: X-ray diffraction spectra of the Fe-doped TiO_2 thin films.

An AFM image from sample D (0.32 at.% Fe) is reported in Figure 5.11. It shows that the thin films are composed of small crystallites. The crystallite diameter, around 35 nm, is larger than the size measured with XRD (10 to 20 nm). As XRD, in θ/2θ diffraction configuration, is sensitive to the crystallite thickness perpendicularly to the film and AFM image shows the film surface, this means either that the grains are not spherical or that the grains are larger at the film surface than in the inner region.

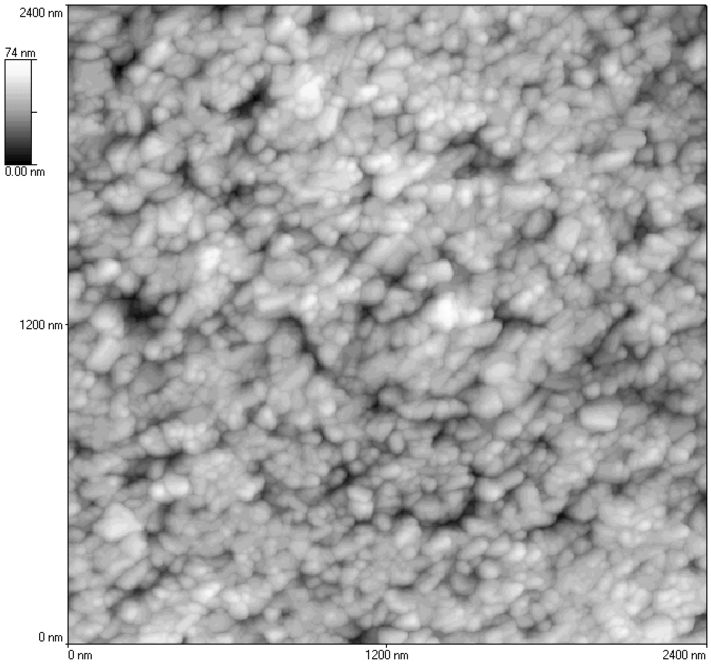

Figure 5.11: AFM image of sample D (0.32 at.% Fe).

5.4.3 Electrical properties

The dc electrical conductivity versus temperature was measured for various Fe concentrations (Figure 5.12). For a fixed temperature, as the Fe concentration increases, the conductivity at first decreases, goes through a minimum for an Fe concentration between 0.13 and 0.32 at.% and then increases again (see Figure 5.13 (a)). This kind of behavior, already reported in the literature for the case of Mn-doped TiO_2 [14], suggests a transition from n-type to p-type electrical conduction. Thermoelectric power measurements made at 350°C show that samples A and B have n-type conductivity (negative thermoelectric power) and that other samples have p-type conductivity (positive thermoelectric power). The thermoelectric power is lower in sample C than in samples D to H where it is nearly constant. This means that the transition between n-type and p-type TiO_2:Fe occurs for an Fe concentration near 0.13 at.%. It has been reported in the literature that Fe impurities act as acceptor impurities in TiO_2 [4]. But it must be noted that sample B, the sample with the lowest Fe doping, shows an n-type conductivity higher than that of the undoped or, more accurately, not intentionally doped sample A at room temperature. This indicates that new oxygen vacancies are induced by the presence of iron atoms as proposed by Sayle et al. [3]. The activation energy E_{act} is lower in the case of low Fe doping (sample B, 0.51 eV) than in the case of the undoped sample A (0.65 eV). This confirms that the oxygen vacancy surroundings are different in each case. The ratio between the Fe-induced oxygen vacancy concentration and the iron concentration must be greater than 0.5 so as to account for the fact that all the acceptors created by the iron atoms are compensated by electrons given up by the oxygen vacancies (two electrons are available from each vacancy). As the iron concentration increases the donor (vacancy) over acceptor (iron) ratio decreases and when it becomes lower than 0.5, switching from n-type to p-type conductivity becomes possible.

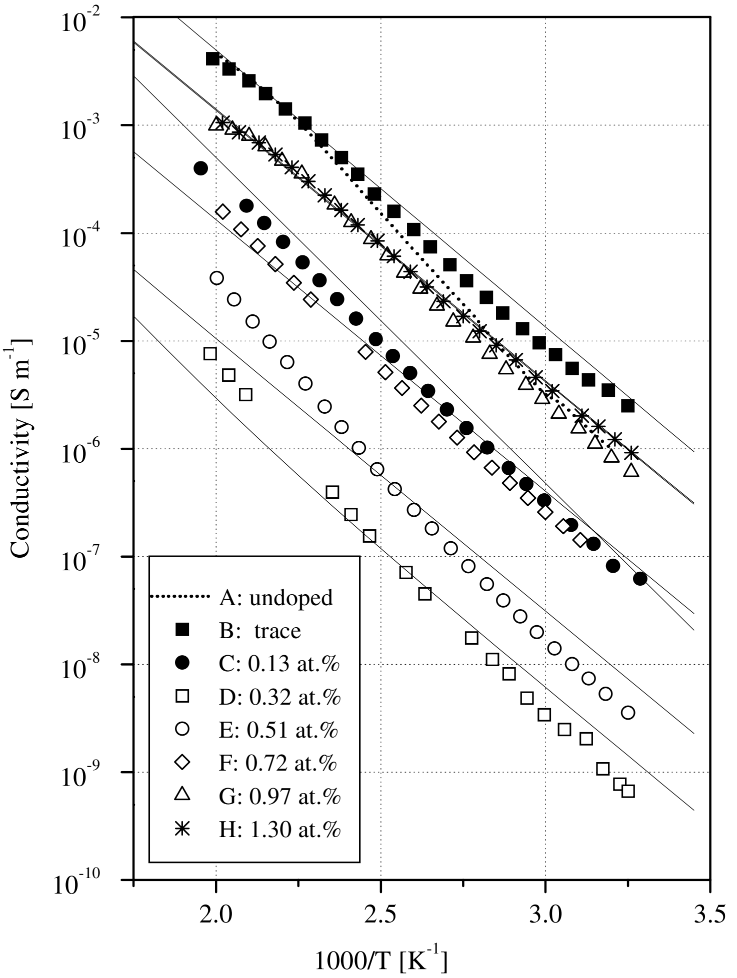

Figure 5.12: Influence of Fe doping on the DC conductivity of TiO_2 thin films. The solid lines represent the dc conductivity calculated using the values given in Table 5.VI.

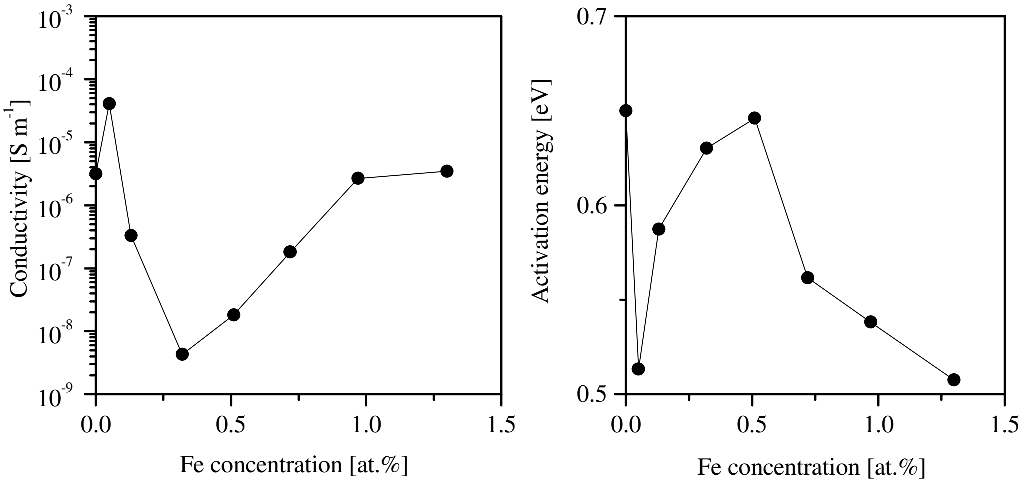

Figure 5.13: The evolution of the conductivity at 333 K (a) and the activation energy (b) versus the Fe concentration. Lines are guide for the eyes.

Numerical values given in Table 5.VI quantify the above discussion; the corresponding conductivities are reported in Figure 5.12. A maximum number of parameters were kept constant to make the interpretation of the results easier. In fact only the ratio between the iron impurities and the oxygen vacancies was changed from one fit to the next. The unknown p-type mobility was assumed to be 0.1 x 10^{-4} m^2/Vs and a reasonable value of the valence band density of states of 9 x 10^{25} m^{-3} was chosen. Each iron atom produces an acceptor level fixed at 0.5 eV above the valence band in these fits, but it might be different in rutile and anatase. The other parameters are the same as those used in the analysis of the TiO_2:Ce conductivity (see Table 5.IV).

Table 5.VI: Numerical values for dc conductivity.

name	Fe concentration [at.%]	V_O/Fe ratio
A	0	-
B	Trace ~ 0.05	0.75
C	0.13	0.75
D	0.32	0.47
E	0.51	0.47
F	0.72	0.40
G	0.97	0.15
H	1.30	0.15

The ratios of oxygen vacancy concentration over iron concentration given in Table 5.VI, indicate that TiO_2 thin films with 0.13 at.% Fe (V_O/Fe = 0.75 > 0.5) have n-type conductivity contrary to the prediction derived from Seebeck measurements performed on samples deposited on glass substrates. This means that the deposition is not uniform in the chamber and that there is a little more iron on glass substrate than on ITO substrates. As Si substrates used for the chemical analyses were on the same support in the deposition chamber as the ITO substrates, we must hope that iron concentration is thin films deposited on ITO is the same as the iron concentration measured on top of silicon.

The fact that the iron atoms create fewer oxygen vacancies at high concentration is consistent with the transformation from the anatase to the rutile structure when the iron concentration increases. Oxygen vacancies are necessary to stabilize the anatase structure [41] but iron can crystallize in a rutile-like structure as FeS_2 or $(Ta,Ti,Fe)O_2$ compounds [42] for example. Therefore, Fe atoms create fewer oxygen vacancies in the rutile structure than in the anatase structure.

The permittivity versus frequency was measured for different Fe concentrations (Figure 5.14). At low doping, the permittivity exhibits a high value, which varies with frequency. Although the permittivity of the most heavily doped samples (> 0.72 at.%) is lower than that of sample B (see Table 5.V), it also decreases with increasing frequency. The lowest permittivity values are observed in highly resistive thin films, for which the permittivity is frequency independent. The values (around 40) are quite the same as the value reported for Ce-doped TiO_2. It is interesting to check if the hopping model is suitable to interpret the electrical conduction in Fe-doped TiO_2 thin films. The fits using the hopping model, represented by solid lines in Figure 5.14, show that this model is satisfactory. At low Fe doping (sample B), the exponent p associated with hopping conduction is higher than in the case of an undoped sample. Contrary to the case of cerium doping, p decreases down to 0.45 when the iron concentration increases as shown in Figure 5.15. The different behavior between iron and cerium doping, even at low doping when anatase thin films are produced in both cases, emphasize the different impurity insertion mechanism. The difference is probably related to the number of oxygen vacancy introduced together with the impurity. High ratio between impurities and oxygen vacancy concentration results in a high exponent p.

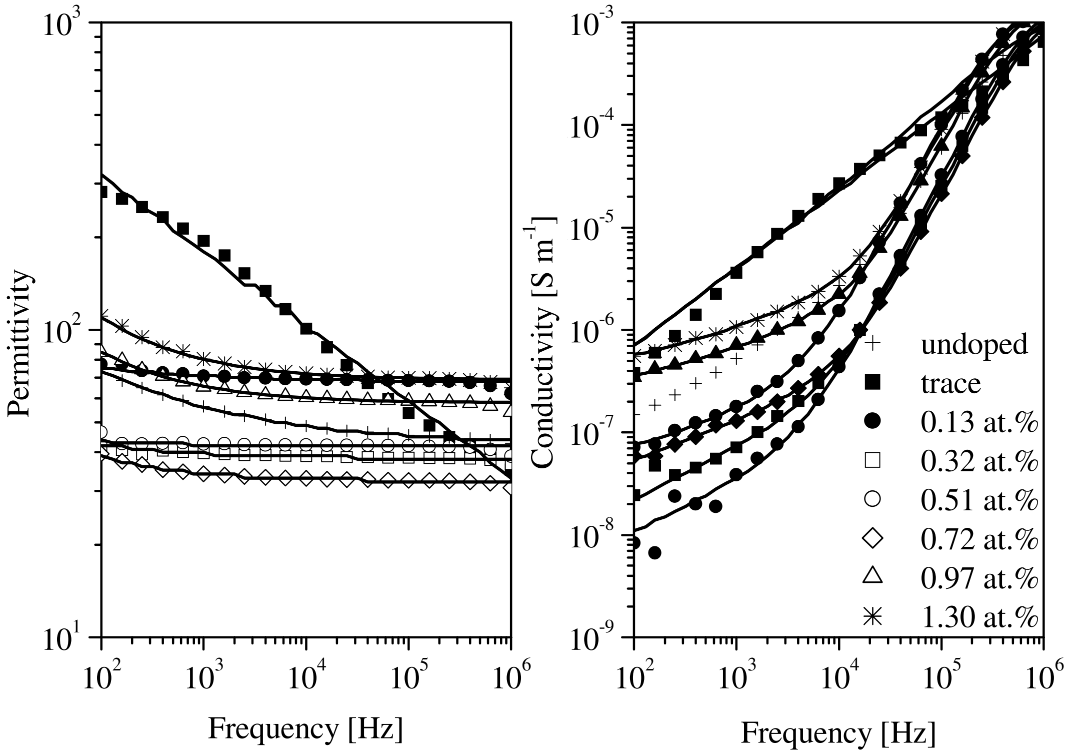

Figure 5.14: Influence of Fe doping on the permittivity of TiO_2 thin films. The solid lines represent the calculate permittivity and conductivity.

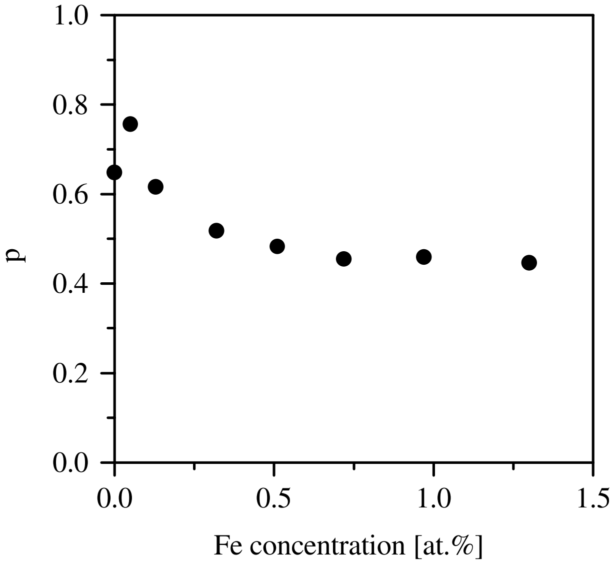

Figure 5.15: Evolution of hopping conduction exponent versus the iron concentration.

5.4.4 Optical properties

All TiO_2:Fe thin films are transparent in the visible range. The optical transmission of thin films deposited on glass is presented in Figure 5.16. The absorption edge for interband transitions appears at a lower energy in highly Fe-doped samples than in undoped samples. This behavior reflects the increased proportion of rutile in heavily doped samples; and our analysis of the optical properties must take into account the heterogeneous nature of the samples composed of nanocrystalline grains. To describe this behavior, a model based on an effective medium theory has been used to take into account the presence of both anatase and rutile phase in the films.

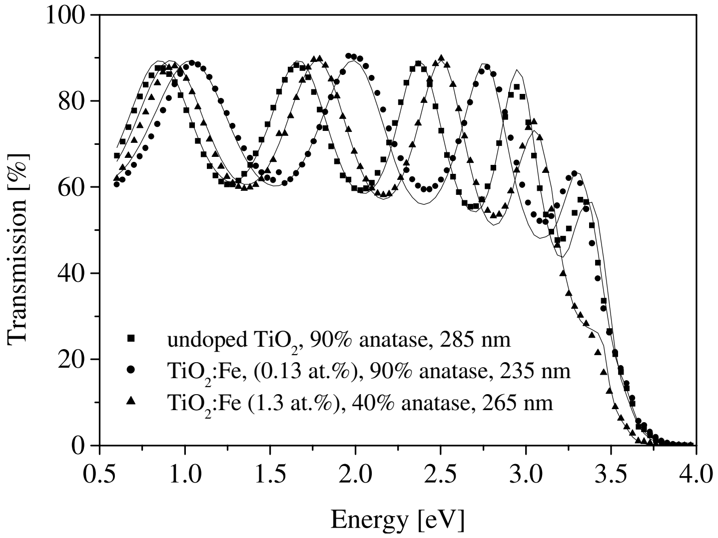

Figure 5.16: Optical transmission of Fe-doped TiO_2 thin films deposited on a glass substrate. The solid lines represent the calculated optical transmission.

Effective medium theories propose that the dielectric constant of a heterogeneous system is a function of the dielectric constant of the constituents and of the morphology. The theories apply if the characteristic size of the inhomogeneities is smaller than the wavelength of light. The best-known effective medium models are the Maxwell Garnett [43] and the Bruggeman [44] model. An excellent review of the effective model approximation has been published by D. E. Aspnes [45].

The Maxwell Garnett theory considers a sample composed of spherical inclusions with dielectric constant ε_i embedded in a medium with dielectric constant ε_m. The fraction of volume of the inclusions is noted p_i. The model considers that the inclusion have no interactions, so that the distance between them must be large enough. This model applies for small amounts of inclusions. The effective dielectric constant ε_{eff} is given as:

$$\frac{\varepsilon_{eff} - \varepsilon_m}{\varepsilon_{eff} + 2\ \varepsilon_m} = \sum_i\ p_i \frac{\varepsilon_i - \varepsilon_m}{\varepsilon_i + 2\ \varepsilon_m}$$

The Bruggeman effective medium approximation considers that the medium that embeds each constituant particle is the effective medium itself. The Bruggeman effective dielectric constant ε_{eff} as:

$$\sum_{\mathrm{i}} p_i \frac{\varepsilon_i - \varepsilon_{eff}}{\varepsilon_i + 2\ \varepsilon_{eff}} = 0$$

where p_i is the fraction of volume of material i with a dielectric function ε_i. The Bruggeman model is expected to apply when $\mathrm{p} \approx 0.5$.

G. W. Milton has calculated the regions of ε_{eff} in the complex plane that are available for a two–component material [46]. These regions are shown in Figure 5.17. Depending on what is known about the composite, the bounding region is

- $\Omega(\varepsilon_1, \varepsilon_2)$ if we have no knowledge of the geometry of the composite.
- $\Omega'(\varepsilon_1, \varepsilon_2; p_1, p_2)$ if the volume fractions p_1 and $p_2 = 1 - p_1$ of the components are known.
- $\Omega''(\varepsilon_1, \varepsilon_2; p_1, p_2; d)$ if p_1 and p_2 are known and if the structure of the composite is isotropic. Here d is the dimensionality of the system we are considering ($d = 2$ or 3).

The bounds for the effective dielectric constant in the case of a mixture of metal titanium ($\varepsilon_1 = -2.2 + 6.9\ \mathrm{i}$) and transparent rutile ($\varepsilon_2 = 7.2$) for a photon energy of 2 eV [47], are presented in Figure 5.17. In this figure the chosen volume fraction of rutile is $p_1 = 1 - p_2 = 0.01$, and

$\mathrm{A} = p_1\ \varepsilon_1 + p_2\ \varepsilon_2$ corresponds to needles parallel with electric field

$\mathrm{B} = (p_1/\varepsilon_1 + p_2/\varepsilon_2)^{-1}$ corresponds to plates perpendicular to electric field

$\mathrm{X}_3 = \varepsilon_1 + \dfrac{3\ p_2\ \varepsilon_1\ (\varepsilon_2 - \varepsilon_1)}{3\ \varepsilon_1 + p_1\ (\varepsilon_2 - \varepsilon_1)}$ corresponds to sphere of component 2 coated by component 1

$\mathrm{Y}_3 = \varepsilon_2 + \dfrac{3\ p_1\ \varepsilon_2\ (\varepsilon_1 - \varepsilon_2)}{3\ \varepsilon_2 + p_2\ (\varepsilon_1 - \varepsilon_2)}$ corresponds to spheres of component 1 embedded in component 2

The dashed lines delimit the region Ω which contains the effective dielectric constant of all possible mixtures of titanium and rutile. It is situated between the straight line joining the dielectric constants of rutile and titanium and the arc $\varepsilon_1 B \varepsilon_2$. The dotted lines delimit the region Ω' in the case of $p_1 = 0.01$. They correspond to arcs AX_3B and AY_3B. The region Ω'' is delimited by the solid lines. The square represents the effective constant calculated with the Bruggeman effective approximation. As expected, it is included in the smaller region of effective dielectric function. In this case, it is close to Y_3, which correspond to small Ti spheres in the Maxwell Garnett approximation.

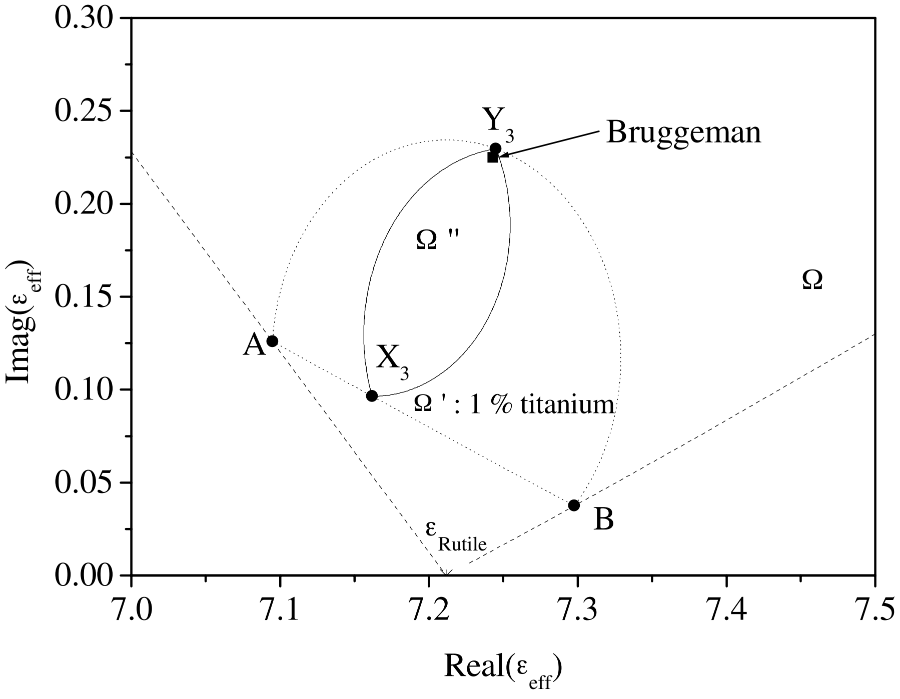

Figure 5.17: Bounds of the effective dielectric constant ε_{eff} in the case of a mixture of metal titanium ($\varepsilon_1 = -2.2 + 6.9$ i) and rutile ($\varepsilon_2 = 7.2$) calculated for a photon energy of 2 eV. The regions Ω, Ω', and Ω'' are delimited by dashed lines, dotted lines, and solid lines respectively. The square represents the effective dielectric constant of a mixture containing 1 % of titanium calculated with the Bruggeman effective medium approximation. A, B, X_3 and Y_3 are calculated with the formulae given in the previous page.

Similar calculations applied to anatase and rutile mixtures lead to smaller regions of the complex plane available for the effective dielectric function because rutile and anatase have similar optical properties. The largest difference occurs around the band gap energy which is different in each phase, namely 3.0 eV for rutile at room temperature and 3.4 eV for anatase. If we apply Milton's limits for the case of the dielectric constant of a mixture of anatase ($\varepsilon_1 = 10.4 + 0.3$ i) [48] and rutile ($\varepsilon_2 = 14.1 + 1.8$ i) [47] at 3.5 eV, we obtain the curves presented in Figure 5.18. At low rutile volume fraction, the Bruggeman effective theory gives results similar to the value calculated with the Maxwell Garnett approximation as shown by the solid lines. Therefore, the Bruggeman approximation was used to model the measured optical transmission given in Figure 5.16 for all values of the rutile fraction.

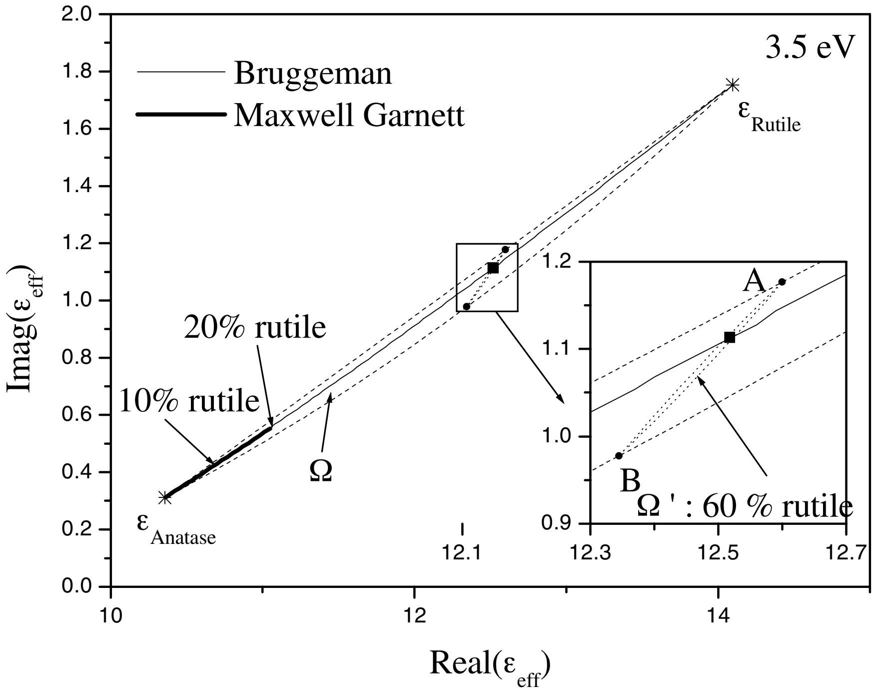

Figure 5.18: Bounds of the effective dielectric constant ε_{eff} in the case of a mixture of anatase (ε_1 = 10.4 + 0.3 i) and rutile (ε_2 = 14.1 + 1.8 i) calculated for a photon energy of 3.5 eV. The regions Ω and Ω' are delimited by dashed lines and dotted lines respectively. The square represents the effective dielectric constant of a mixture containing 60 % of rutile calculated with the Bruggeman effective medium approximation. The solid lines represent the effective dielectric constant calculated with the Bruggeman and Maxwell Garnett effective medium approximation.

The optical transmission of the thin films was calculated using the weight percent of anatase calculated from the XRD spectra. The dielectric constants of rutile and anatase were taken from reference 47 and 48. The anisotropic rutile dielectric constant was averaged with the Bruggeman effective medium approximation considering that 1/3 of the rutile particles have their optical axis parallel to the incident beam. The result is represented by solid lines in Figure 5.16. This calculation shows that the change in the absorption spectrum in not actually related to the iron concentration, it simply reflects the change of structure from anatase to rutile induced by the iron atoms.

5.4.5 Summary

We have shown that iron doping induces a transformation from anatase to rutile, without amorphization for doping concentrations lower than 1.3 at.%. Electrical measurements confirm that iron is an acceptor impurity. The introduction of iron generates more oxygen vacancies in anatase than in rutile. A large fraction of the acceptors created by the iron atoms is compensated by the oxygen vacancies created by the same iron atoms. Thus, in spite of high doping concentration, the p-type electrical conductivity of TiO_2:Fe is not much greater than the n-type electrical conductivity observed in undoped TiO_2. The transition from n-type to p-type electrical conduction occurs for an iron concentration around 0.13 at.%. The highest p-type conductivity reached at room temperature is 10^{-6} S m^{-1}. The influence of the iron atom depends on the crystal structure of the oxide.

5.5 Conclusion

We have seen that the incorporation of high concentration of impurities induces structure modifications in TiO_2 thin films. Therefore, it is difficult to predict the electrical properties of doped TiO_2. The electrical conductivity measured in the case of n-type TiO_2 obtained with niobium (1 x 10^{-3} S m^{-1}) doping is 1000 higher than the conductivity of undoped TiO_2. This can appear as a great step, but we are dealing with percent concentrations of impurities and if we compare this result with what is happening in the case of the doping of silicon, we find that a majority of these impurities are compensated by defects created by the impurity itself. The large amount of defects, with concentrations close to that of the incorporated impurity, seems usual in the case of transition metal ions, but it may also be due to the low temperature of deposition, less than 300°C. Ceramic Nb-doped TiO_2 with a resistivity of 100 S m^{-1} can be prepared at higher temperature around 1000°C [17][49]. In the case of p-type conductivity, with iron doping an electrical conductivity similar at most to that of undoped TiO_2 can reached.

To increase the conductivity of TiO_2, different approaches can be used. It is difficult to increase the charge carrier mobility. Firstly, as mentioned in Table 2.I, the mobility is lower in thin films than in single crystals (up to 100 times lower), because they are composed of small crystallites (~25 nm) separated by grain boundaries that impede the movement of the charge carriers.

We have seen that the introduction of impurities in TiO_2 induces a structural degradation resulting in grains smaller than in undoped TiO_2. The impurities also act as scattering centers that decrease the mobility. A significant increase of the mobility is an unrealistic enterprise. In order to increase the charge carrier density the total number of donors or acceptors can be increased, but it is better to try to find an impurity with a lower activation energy. At room temperature, if the activation energy decreases from 0.5 eV to 0.2 eV, the charge carrier density is increased by a factor 10^5. It is also important to find impurities that do not create defects when they are incorporated in TiO_2 in our deposition conditions. In our experiments, we have found no such impurity.

Table 5.VII summarizes the conductivity and activation energy obtained for several dopants. In the case of conductive TiO_2 the highest electrical conductivity achieved at room temperature is reported, and in the case of insulating TiO_2 the lowest electrical conductivity is reported. It is important to notice that the highest electrical conductivity in the case of n-type and p-type conductivity were obtained when the rutile phase was the dominant phase, even though the electrical mobility is lower in rutile than in anatase.

Table 5.VII: Summary of TiO_2 thin film electrical conductivity.

material	structure on ITO	conductivity [S m^{-1}]	activation energy [eV]
TiO_2:Nb	rutile + anatase	n-type, 1 x 10^{-3}	0.17
TiO_2:Fe	rutile + anatase	p-type, 2 x 10^{-6}	0.51
Undoped TiO_2	anatase + rutile	n-type, 1 x 10^{-6}	0.65
TiO_2:Ce	amorphous	n-type, 3.5 x 10^{-9}	0.6

Though interesting results were obtained with niobium doping, our subsequent efforts were focussed on a different attack of the problem. TiO_2 with an n-type electrical conductivity around 100 S m^{-1}, 10^5 time higher than the better electrical conductivity measured on our thin films deposited using a composite target, have been obtained by using water vapor instead of oxygen as a reactive gas. The description of these thin films is the subject of Chapter 6.

Bibliography

[1] E. C. Akubuiro and X. E. Verykios, Journal of Physics and Chemistry of Solids 50 (1989), 17.

[2] K. Mizushima, M. Tanaka, A. Asai, S. Iida, and J. B. Goodenough, Journal of Physics and Chemistry of Solids 40 (1979), 1129.

[3] D. C. Sayle, C. R. A. Catlow, M.-A. Perrin, and P. Nortier, Journal of physics and chemistry of solids 56 (1995), 799.

[4] M. Radecka, M. Rekas, and K. Zakrzewska, Solid State Phenomena 39-40 (1994), 113.

[5] J. Sheng, T. Fukami, and J. Karasawa, Journal of the Electrochemical Society 145 (1998), 1592.

[6] F. C. Gennari and D. M. Pasquevich, Journal of Materials Science 33 (1998), 1571.

[7] A. Bernasik, M. Rekas, M. Sloma, and W. Weppner, Solid State Ionics 72 (1994), 12.

[8] K. Hatta, M. Higuchi, J. Takahashi, and K. Kodaira, Journal of Crystal Growth 163 (1996), 279.

[9] S. Vemury and S. E. Pratsinis, Journal of the American Ceramic Society 78 (1995), 2984.

[10] G. A. Acket and J. Volger, Physica 32 (1966), 1680.

[11] A. Bernasik, M. Radecka, M. Rekas, and M. Sloma, Applied Surface Science 65/66 (1993), 240.

[12] J.-L. Carpentier, A. Lebrun, and F. Perdu, Journal of Physics and Chemistry of Solids 50 (1989), 145.

[13] N. G. Eror, Journal of Solid State Chemistry 38 (1981), 281.

[14] S. Fujitsu and T. Hamada, Journal of the American Ceramic Society 77 (1994), 3281.

[15] Siber Hegner Rohstoff AG.

[16] Kurt J. Lesker Compagny.

[17] B. Poumellec, J. F. Marucco, and F. Lagnel, Journal of Physics and Chemistry of Solids 47 (1986), 381.

[18] S. R. Kurtz and R. G. Gordon, Thin Solid Films 147 (1987), 167.

[19] Y. Gao and S. A. Chambers, Journal of materials research 11 (1996), 1025.

[20] K. Prasad, A. R. Bally, P. E. Schmid, F. Lévy, J. Benoit, C. Barthou, and P. Bénalloul, Japanese Journal of Applied Physics 36 (1997), 5696. Paper reported in Appendix A.

[21] D. Wicaksana, A. Kobayashi, and A. Kinbara, Journal of Vacuum Science and Technology A 10 (1992), 1479.

[22] R. W. G. Wyckoff: "Crystal Structure", vol. 1, 2nd ed., Wiley, New York, 1963.

[23] K. Sakata, Journal of Physical Society of Japan 26 (1969), 1067.

[24] D. Briggs and M. P. Sheah: "Practical Surface Analysis", Wiley, New York, 1983.

[25] M. Pollak and B. I. Shklovskii: "Hopping Transport in Solids", North-Holland, Amsterdam (1991).

[26] N. Tsuda, K. Nasu, A. Yanase, and K. Siratori: "Electronic Conduction in Oxides", Springer-Verlag, Berlin (1983).

[27] H. Tang, K. Prasad, R. Sanjinés, P. E. Schmid, and F. Lévy, Journal of Applied Physics 75 (1994), 2042.

[28] A. K: Jonscher, Journal of Non-Crystalline Solids 8-10 (1972), 293.

[29] K. Wasa, and S. Hayakawa: "Handbook of sputter deposition technology", Noyes Publications, New Jersey (1992).

[30] G. Levin and C. J. Rosa, Zeitschrift für Metallkunde 70 (1979), 601. G. Levin and C. J. Rosa, Zeitschrift für Metallkunde 70 (1979), 646.

[31] T. Inoguchi and S. Mito> "Topic in Applied Physics 17: Electroluminescence", J. I. Pankove, Springer, New York, 1982.

[32] Y. Fujita, J. Kuwata, M. Nishikawa, T. Tohda, T. Matsuoka, A. Abe, and T. Nitta, Japan display (1983), 76.

[33] Y. Ono: "Series on information display: Electroluminescent Display", World Scientific Publication Co.,

London, 1995.

[34] A. R. Bally, K. Prasad, R. Sanjines, P.E. Schmid, F. Levy, J. Benoit, C. Barthou, and P. Benalloul, MRS 1996 Spring Meeting, Material Research Society Symposium Proceeding Vol. 424 (1997), 471. Paper reported in Appendix A.

[35] P. Kofstad: “Nonstoichiometry, Diffusion, and Electrical Conductivity in Binary Metal Oxides”, Publishing Compagny, Malabar, 1983.

[36] J. Zarzycki: “Materials Science and Technology volume 9: Glasses and Amorphous Materials”, VCH, Weinheim (1991).

[37] B. E. Springett, Journal of Non-Crystalline Solids 15 (1974), 179.

[38] A. K. Jonscher, Nature 267 (1977), 673.

[39] F. Argall and. A. K. Jonscher, Thin Solid Films 2 (1968), 185.

[40] D. L. Sidebottom, P. F. Green, and R. K. Brow, Physical Review B 51 (1995), 2770.

[41] F. Bregani, C. Casale, L. E. Depero, I. Natali-Sora, D. Robba, L. Sangaletti, and G. P. Toledo, Sensors and Actuators B 31 (1996), 25.

[42] J. F. Banfield, B. L. Bishoff, and M. A. Anderson, Chemical Geology 110 (1993), 211.

[43] J. C. M. Garnett, Philosophical Transaction of the Royal Society of London 203 (1904), 385.

[44] D. A. G. Bruggeman, Annal of Physics 24 (1935), 636.

[45] D. E. Aspnes, Thin Solid Films 89 (1982), 249.

[46] G. W. Milton, Applied Physics Letters 37 (1980), 300.

[47] E. D. Palik: “Handbook of Optical Constants”, Academic Press, New York, 1985.

[48] R. J. Gonzales, R. Zallen, and H. Berger, Physical Review B 55 (1997), 7014.
R. H. French, R. M. Cannon, L. K. DeNoyer, and Y. M. Chiang, Solid State Ionics 75 (1995), 13.

[49] J. F. Marucco, B. Poumellec, J. Gautron, and P. Lemasson, Journal of the Physics and Chemistry of Solids 46 (1985), 709.

Chapter 6

TiO_{2-x} deposited with H_2O as reactive gas

One of the important goals of our work on sputtered TiO_2 is the obtainment of conductive, n-type TiO_2 films that are stable up to 300°C or more. In the past, a commonly explored approach has been the addition, either as interstitials or as Ti-substitutes, of many metal atoms, and to a lesser degree, the addition, either as interstitials or as O-substitutes, of halogen atoms. We have chosen the option to attempt to change the stoichiometry of TiO_2 directly, i.e. by a modification of the sputtering gas that would affect the way oxygen is incorporated into the oxide thin film. We have obtained remarkable results by replacing the O_2/Ar mixture of the usual sputtering gas by an H_2O/Ar mixture

Other transparent conducting oxides (TCO) have been deposited by sputtering with an addition of water to the reactive gas already. In many cases, the conductivity of indium tin oxide [1-2], ZnO [3] or WO_3 [1] decreases slightly when H_2O is added to the reactive gas, but in a recent publication, the conductivity of amorphous ITO was shown to double when water vapor was used [4]. In all cases, the thin film morphology (grain size, texture or density) is modified by the addition of water vapor. To our knowledge, the deposition of TiO_2 with water vapor as reactive gas has not been attempted yet. Preliminary tests with oxygen and a small addition of water vapor as reactive gas do not modify in a significant manner the properties of the deposited thin films. For this reason it was decided that our work would concentrate on the deposition of TiO_x either with a mixture of argon and oxygen (type O TiO_x), or with a mixture of argon and water vapor (type W TiO_x).

6.1 Preliminary results

The first step consisted in verifying that TiO_2 thin films can be deposited with water vapor. Depositions made in the triode installation showed that the full stoichiometry range of TiO_x can be obtained as presented in Figure 6.1. The H_2O partial pressure must be higher than the corresponding O_2 partial pressure to obtain a given chemical composition, which can be explained by the fact that for a given pressure there are more oxygen atoms available with O_2 gas than with H_2O. Indeed, in a plasma composed of water vapor, the main species are H_2O, H and OH. The pressure ratio between oxygen and water vapor necessary to obtain a given chemical composition is less than 2 and decreases from 1.7 to 1.3 when the stoichiometry increases. A detailed plasma analysis should be undertaken to understand quantitatively the evolution of this ratio. Changes in oxygen concentration in the films are accompanied by color changes from golden yellow for nearly cubic TiO films to transparent for TiO_2 films, passing through brown and dark blue.

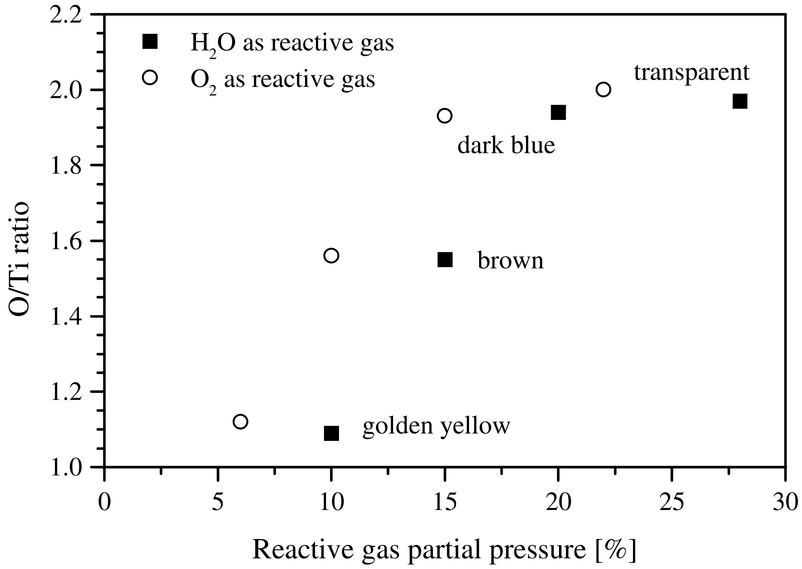

Figure 6.1: Chemical composition of TiO_x thin films versus reactive gas partial pressure in the triode installation.

The corresponding XRD spectra, reported in Figure 6.2, reveal that transparent TiO_x films ($1.95 \leq x \leq 2$) are composed of a mixture of the anatase and rutile phases. When the oxygen concentration decreases, in both cases the rutile phase dominates with a grain size smaller than 10 nm. At lower oxygen concentration, type W TiO_x amorphous films are obtained, while type O TiO_x x-ray diffraction spectra show Ti_2O_3 and Ti_3O_5 diffraction patterns. No amorphous type O TiO_x thin films were observed. Golden yellow TiO_x ($0.9 \leq x \leq 1.25$) have the same *fcc* NaCl structure as TiN. The lattice parameter *a* is 0.422 nm in the case of type W TiO_x, which is considerably larger than the lattice parameter of Type O TiO_x $a = 0.419$ nm that closely matches the values reported in the literature for$TiO_{1.12}$ crystals $a = 0.418$ nm [5].

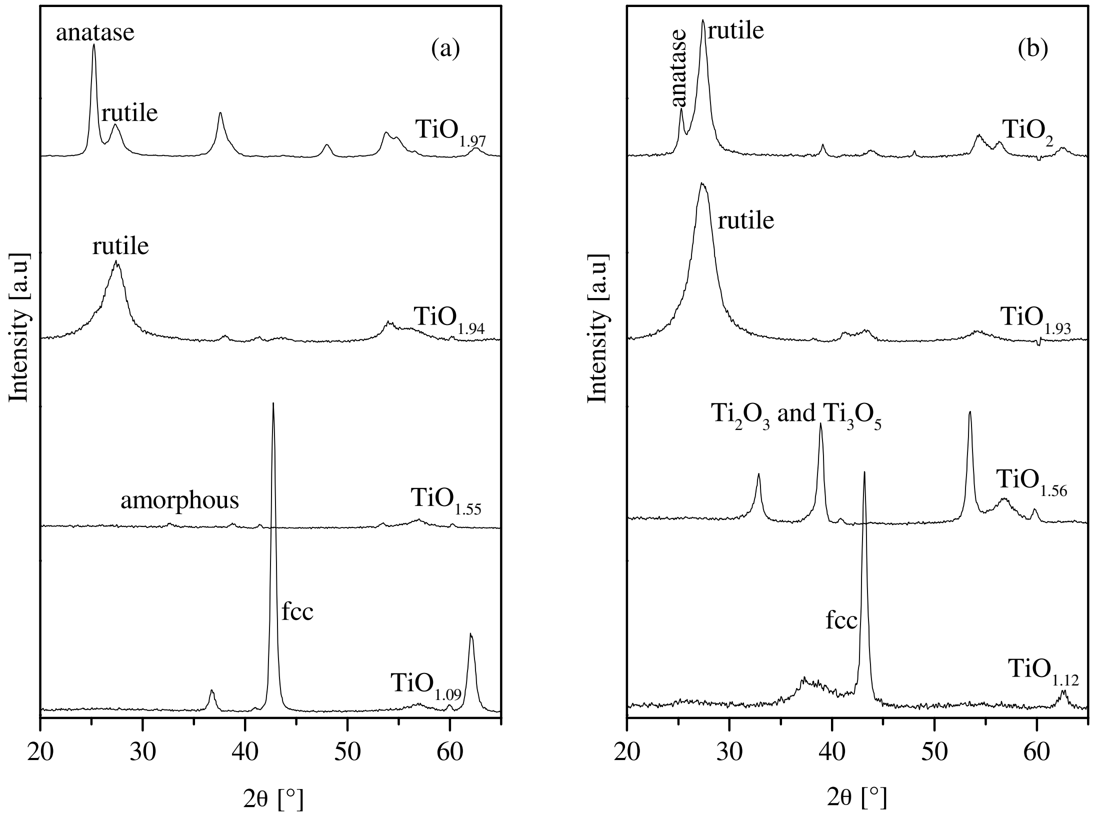

Figure 6.2: X-ray diffraction spectra of TiO_x deposited with (a) H_2O and (b) O_2 as reactive gas.

In a recent work, we have shown that the mechanical properties (hardness) of cubic TiO_x is improved when oxygen is replaced by water vapor as reactive gas during the sputtering deposition [6]. In the case of the electrical conductivity, the improvement is situated in the stoichiometry region close to TiO_2 (see Figure 6.3). Transparent, rutile, type W TiO_x thin films with electrical conductivity as high as 300 S m^{-1} could be obtained. In the case of type O TiO_x, either black conductive thin films or transparent insulating thin films were produced. Thus, a more detailed analysis of TiO_x properties in the region $1.9 < x < 2$ was undertaken.

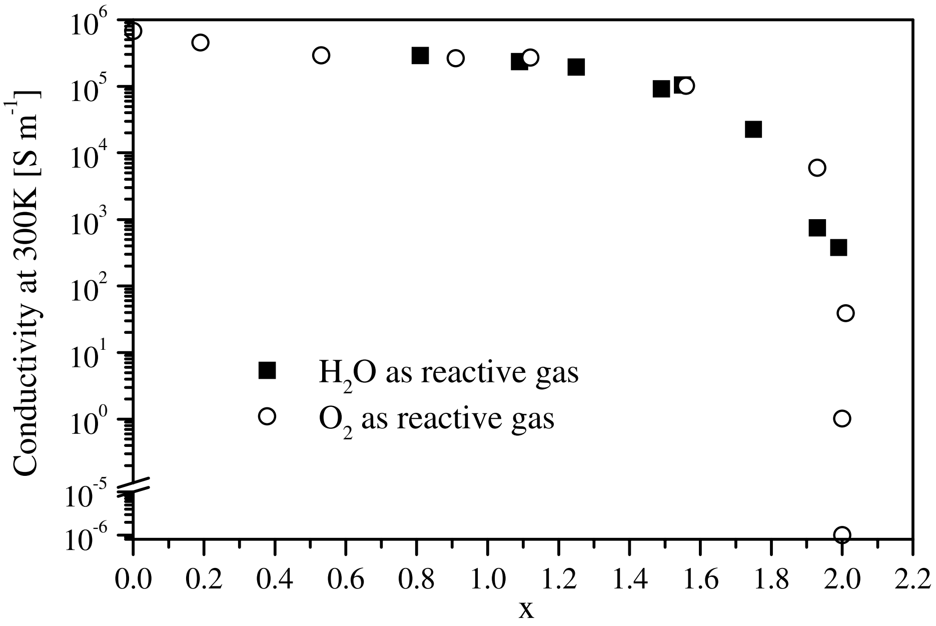

Figure 6.3: Electrical conductivity of TiO_x thin films deposited with oxygen or water vapor as reactive gas.

The following results were obtained with thin films prepared in the magnetron installation because, at that time, the triode installation had broken down. As the sample stoichiometry was always close to TiO_2, the term TiO_{2-x} will replace the generic term TiO_x used above.

6.2 Deposition conditions

When titanium oxide is deposited by sputtering, important reactive gas instabilities can occur affecting the stoichiometry of the thin films for a given set of deposition parameters [7]. It is important to work in well-controlled deposition conditions with a strict starting procedure. The deposition rate as a function of the water vapor or oxygen partial pressure is reported in Figure 6.4. Depositions were made either from a target cleaned during 5 min in a pure argon atmosphere or from targets oxidized in the respective reactive gas (H_2O or O_2). The relation between deposition rate and reactive gas partial pressure is similar in both cases. At the beginning, the deposition rate increases as the chemical composition evolves from metal titanium to *fcc* titanium monoxide. Beyond this point, the deposition rate decreases rapidly while titanium dioxide is deposited. The deposition rate depends on the target oxidation. When the reactive gas pressure increases a competition between target oxidation and target sputtering is established. If the pressure is high enough, the target oxidized abruptly and the deposition rate drops significantly. In a reverse way, when the target is oxidized and the reactive gas partial pressure is decreased, the target oxidation is removed and the deposition rate increases. The pressure necessary to oxidize the target is higher than the pressure required to reduce the target surface. This phenomenon leads to a hysteresis loop in the deposition rate and chemical composition of the thin films versus reactive gas partial pressure. A hysteresis loop appears only in the region where the deposition rate is maximum. Thin films deposited at this high deposition rate are composed of *fcc* titanium oxide. TiO_{2-x} is obtained using a higher reactive gas partial pressure where no hysteresis effects are observed The fact that the hysteresis covered only a small portion of reactive gas partial pressure, compared to other installations, comes from the high pumping speed available in this installation: 170 l s^{-1} at a pressure of 2.5 x 10^{-3} mbar (25 standard cubic centimeter per minute). If the pumping speed increases, the incoming gas flow must also be increased to maintain the same total pressure. The reactive gas flow gettered by sputtered atoms becomes less important relatively to the total gas flow and thus the hysteresis loop shrinks and finally disappears [8]. A high pumping speed provides more stable and reproducible depositions even if it is to the detriment of the deposition rate.

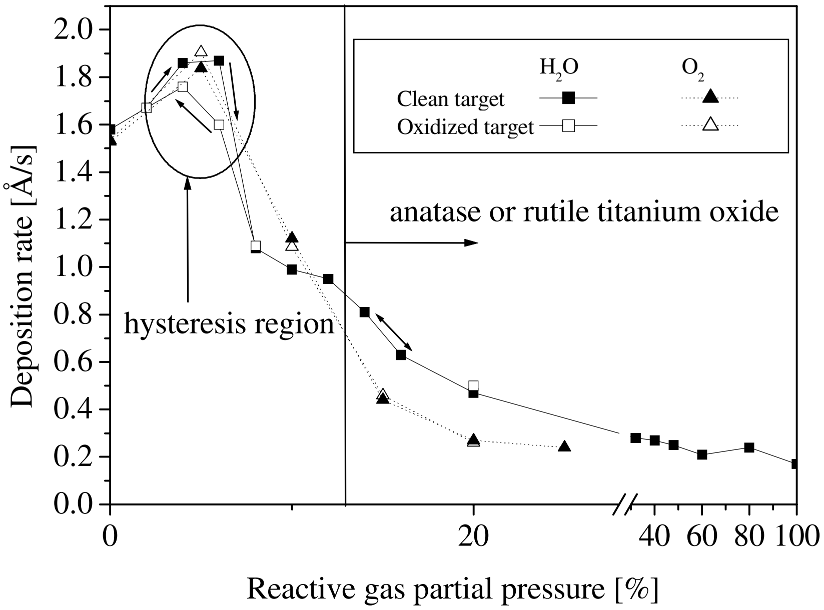

Figure 6.4: Deposition rate of TiO_x thin films versus water vapor or oxygen partial pressure.

Analyses by mass spectrometry of the reactive gas during the deposition show the presence of H_2O, OH, H, H_2 and O when H_2O is used. The O_2 species is only present when titanium dioxide thin films are deposited. It is a good indicator to be sure that there is enough water vapor inside the chamber to produce TiO_{2-x} with small x values.

Two series of samples were deposited with H_2O using different dc current and substrate temperatures, the total gas pressure being 2.5 x 10^{-3} mbar in both cases. Deposition parameters and several thin film properties are reported in Table 6.I. The deposition rates presented in Figure 6.4 belong to the second series.

Table 6.I: TiO_{2-x} thin films deposited with water vapor.

	P_{H_2O} [%]	deposition rate [Å/s]	conductivity at 300K [S m^{-1}]	rutile weight [%]	rutile crystallite size [nm]	anatase crystallite size [nm]
1st series: I = 400 mA Tsubstrate = 185 °C	25	0.72	350	79%	9.8	10.3
	30	0.72	109	57%	9.4	10.9
	35	0.53	36.7	46%	8.8	12
	40	0.44	1.07	52%	10	12.6
	45	0.39	3.1	48%	15.1	14.5
	50	0.42	15.3	0%	-	12.8
2nd series: I = 300 mA Tsubstrate = 250 °C	10	0.99	34900	amorphous	-	-
	12	0.95	1910	100%	7.8	-
	14	0.81	300	100%	9.3	-
	16	0.63	179	100%	9	-
	20	0.47	77	100%	10	-
	32	0.28	26	97%	8.9	29.4
	40	0.27	18.7	100%	11	-
	48	0.25	18.8	100%	11.9	-
	60	0.21	64.9	100%	11	-
	80	0.24	95.7	100%	12.9	-
	100	0.17	67	100%	13.2	-

6.3 Chemical composition and structure

It is important to ascertain the amount of hydrogen inside thin films deposited with water vapor if one wants to understand the role of water in the deposition process and in the doping process. The hydrogen concentration was determined by secondary ion mass spectroscopy. The same hydrogen content was measured in thin films deposited with either H_2O or O_2. The origin of this small and constant hydrogen concentration is attributed to contamination of the films by atmospheric water after their removal from the deposition chamber. A five-minute cleaning by ion bombardment in the SIMS chamber was enough to remove all hydrogen in the film surface. To make sure that there was no additional hydrogen in type W TiO_2 thin films, heavy water (D_2O) was used for several depositions. Deuterium atoms were detected only when the hydrogen signal was high, i.e. measured on “contaminated” thin films. The ratio between hydrogen and deuterium was the isotopic ratio. Infrared measurements and nuclear magnetic resonance, which are less sensitive methods, also failed in detecting hydrogen inside thin films. Therefore we can conclude that there is no hydrogen incorporated in the thin films. This can be due to the fact that the substrates were heated at temperature higher than 180°C during the deposition. The oxygen/titanium ratio in the sample was measured by EPMA. It varies from 1.9 in the case of dark blue samples to 2 for transparent TiO_2.

XRD spectra were obtained at grazing incidence on thin films deposited on glass, the typical substrate used for electrical and optical measurements. When samples contain rutile, the (110) rutile peak is always visible whereas all other rutile peaks are either much smaller than in the standard X-ray diffraction pattern, less than 5% the intensity of the (110) peak, or not present at all. When samples contain anatase, all anatase peaks are visible. It can be concluded that rutile samples deposited with the magnetron installation are textured. Rutile fraction and rutile grain size in the films were calculated from the X-ray diffraction spectra. The results are reported in Table 6.I. If the substrate temperature is low enough, the anatase fraction increases as in the case of type O TiO_2 when the reactive gas partial pressure increases. Except for samples deposited with 32% of water vapor, at 250°C, only the rutile phase is present in the type W TiO_{2-x} samples. The sample deposited with 32% of water vapor is the thickest one (410 nm) whereas 250 nm is the maximum thickness for the other samples. The appearance of the anatase phase is related to the larger thickness as has already been reported in numerous studies [9-10]. The rutile grain size increases with the water vapor partial pressure. In each case, the rutile (110) peak is shifted to a lower angle, corresponding to a larger unit cell. The maximum shift is measured on samples deposited with 16% of water vapor: they show a (110) inter-planar distance 0.5% larger than in the case of stoichiometric, single crystal, rutile. Samples prepared with more than 40% of water vapor exhibit a (110) inter-planar distance increase of less than 0.05%.

Thin film morphology was investigated by atomic force microscopy (AFM). Mixed anatase-rutile sample (50%-50%) and pure rutile sample images are presented in Figure 6.5. The crystallite size, larger in the case of samples containing anatase phase, corresponds to the crystallite size determined by XRD. In mixed anatase-rutile sample, the crystallite size was 18 and 12 nm for anatase and rutile respectively, whereas the rutile sample has smaller grain size of 10 nm. Similar pictures are observed on the different type W TiO_{2-x} samples.

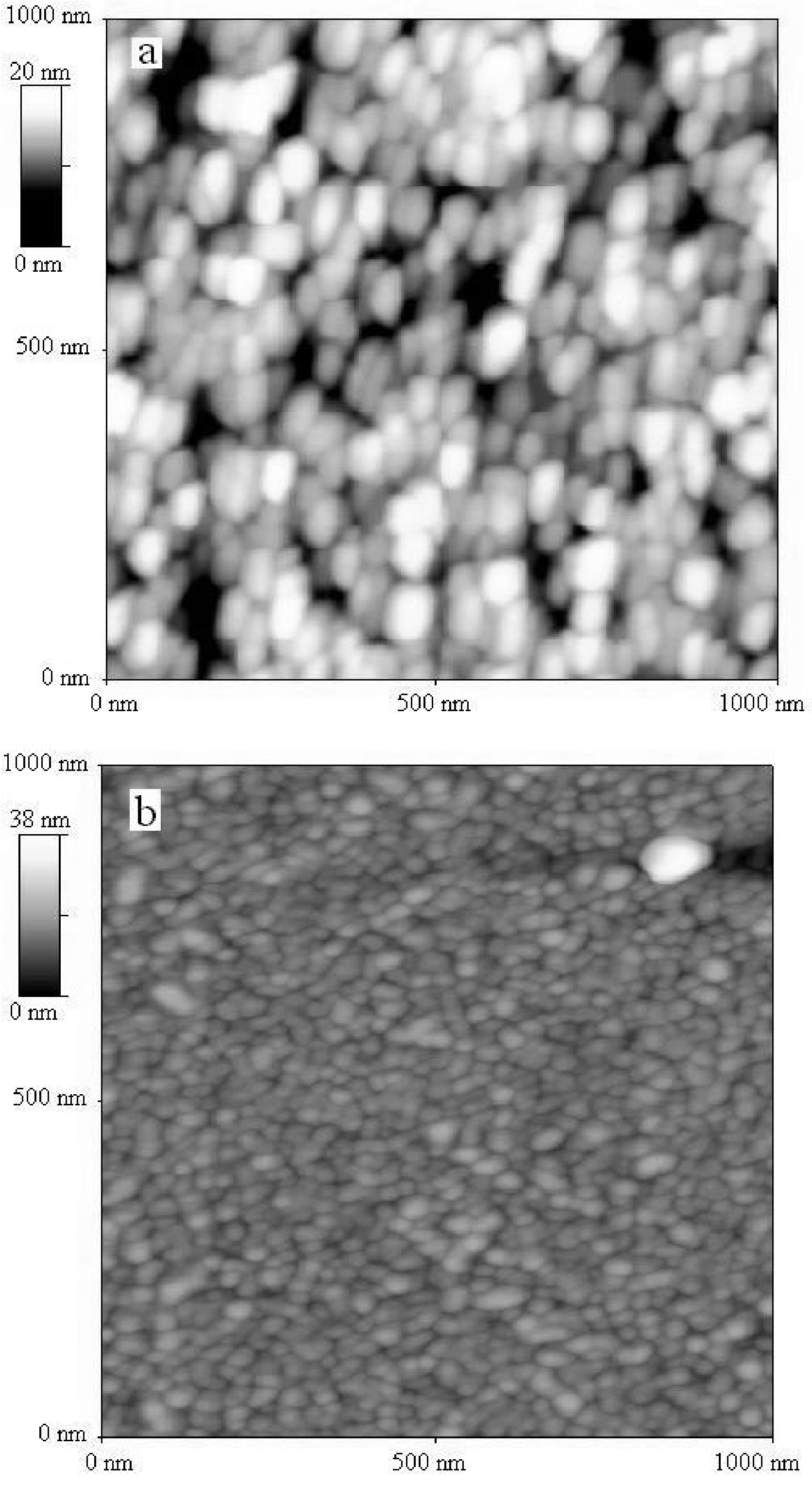

Figure 6.5: AFM non-contact mode images.

a) mixed anatase-rutile (50%-50%) TiO_{2-x} thin film

b) pure rutile TiO_{2-x} thin films.

6.4 Electrical properties

The resistance of type W TiO_{2-x} measured in the transverse geometry in the same way as doped TiO_2 (see Chapter 5) is lower than the series resistance of the ITO substrate (40 – 100 Ω), thus the electrical measurements were made along the films on glass substrate. In the case of type O TiO_2 the resistivity is high so that measurements on glass are not possible with standard electrodes distant of half a millimeter. Current-voltage curves measured on a film deposited on glass with top gold or aluminum contacts are reported in Figure 6.6. Ohmic contacts are obtained with aluminum, while a power law I-V relationship indicates that gold, which has a higher work function than aluminum, forms hole-injecting contacts [11-12]. The conductivity was measured with a four point geometry (see Chapter 4) so as to evaluate (and eliminate) the Al contact impedances. As reported in Figure 6.7, the resistance measured with aluminum contacts is the same as the resistance calculated from the thin film conductivity and contact geometry at temperatures higher than room temperature. Thus if electrical contacts are needed for a specific application, aluminum is suitable for ohmic contacts with negligible resistance. In the following, the dc electrical measurements were made in the van der Pauw geometry, because the samples required less preparation, no contact evaporation, and they could be used afterwards to make other measurements such as optical measurements.

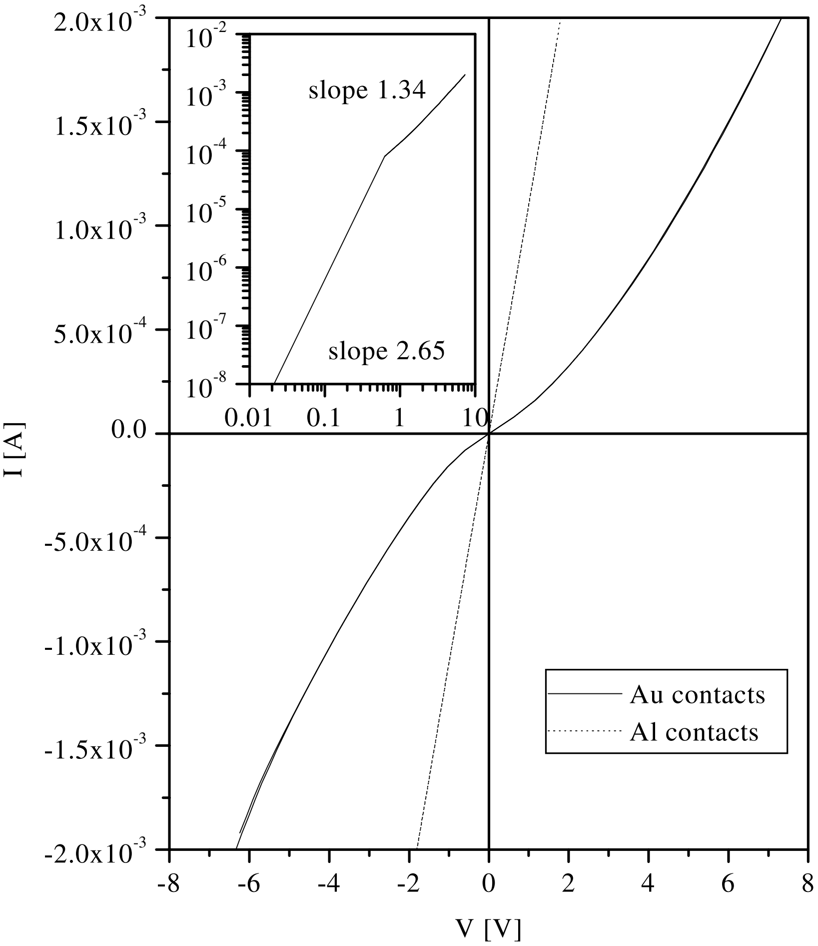

Figure 6.6: Current-voltage curves measured on rutile type W TiO_{2-x} thin film deposited with H_2O as reactive gas.

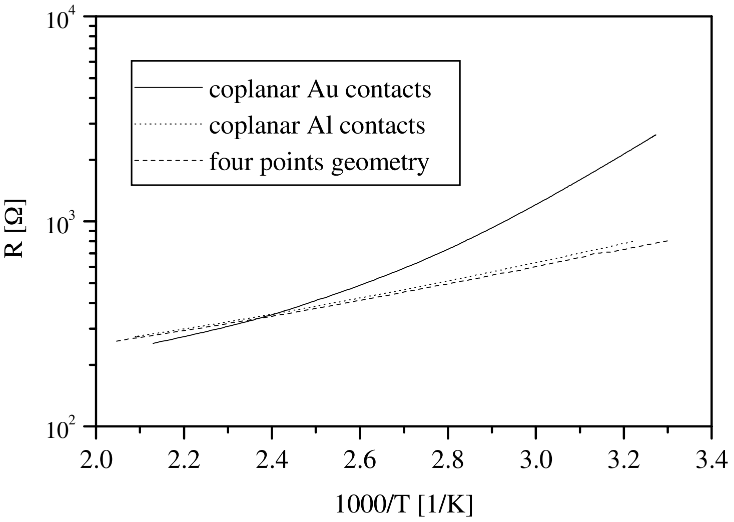

Figure 6.7: Comparison of resistance measured on rutile type W TiO_{2-x} with three different electrical configurations.

The room temperature electrical conductivity of TiO_{2-x} thin films prepared in the magnetron installation is reported in Figure 6.8. The most striking result is that the electrical conductivities obtained are very high, comparable with heavily reduced titanium dioxide [13]. TiO_2 thin films deposited with oxygen as reactive gas are usually insulating with a conductivity close to 10^{-6} S m^{-1} (see Chapter 5), 10^6 time lower than the lowest conductivity measured on the present series of samples. No insulating layer has been obtained in whole range of water vapor partial pressure (0% to 100%). The second striking feature of Figure 6.8 is that the conductivity has a minimum for an H_2O concentration around 40%. When oxygen is used as reactive gas, the electrical conductivity decreases continuously with the increase of the oxygen partial pressure [14]. The minimum of the conductivity is not related to a change of morphology. The grain size and the anatase/rutile ratio follow a monotonic behavior. This indicates that x-rays diffraction measurements are not enough to describe all the sample properties that are relevant to determine the electrical conductivity. Grain boundary and composition changes are the likely candidates to explain the remarkable transport properties of type W TiO_2 samples.

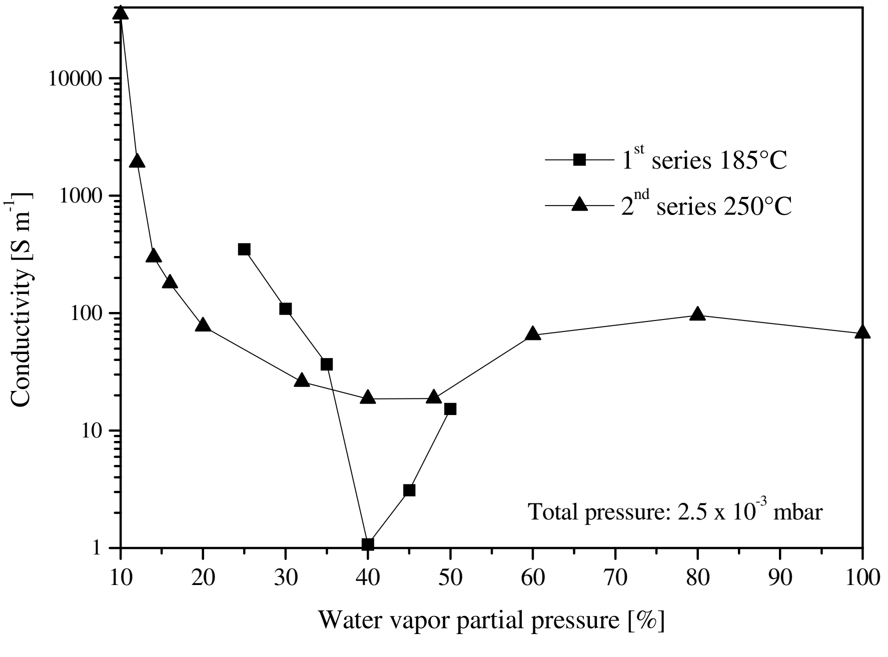

Figure 6.8: Room temperature electrical conductivity at of TiO_{2-x} thin films versus the water vapor partial pressure. The lines are a guide to the eye.

The evolution of the electrical conductivity as a function of temperature in air has been measured by the Van der Pauw method for thin films of series number 2 deposited with 20%, 40%, 60%, and 100% of water vapor. A less conducting film (40%, series number 1) was also measured. The heating rate was as low as possible, 1°C/min, in order to determine the temperature at which the thin film degrades, i.e. the temperature at which the conductivity starts to decrease. In Figure 6.9, we can see that among the samples measured, the highest degradation temperature is 300°C in air. It is obtained with a sample showing a medium electrical conductivity, deposited at medium water vapor partial pressure (60%). The activation energy is low, less than 0.1 eV, compared to doped TiO_2 presented in Chapter 5 (more than 0.5 eV). The differences between the conductivities of type W TiO_{2-x} and type O TiO_{2-x} are too large to be the result of a mobility improvement only, it more likely due to a different type of donor or to a localization of the donors in different regions of the films. If we suppose that charge carriers come from donors, a rapid calculation using a mobility of 0.1×10^{-4} Vs/m^2 for rutile (see chapter 2) indicates a donor concentration of 3 at.% in the case of the most conducting layer presented in Figure 6.9 (20% H_2O). If the donors were bulk oxygen vacancies, x-ray diffraction should show a significant decrease of the volume of the unit cell. As seen in the XRD measurements, the unit cell is actually slightly larger in the case of type W TiO_{2-x} than in the case of pure, stoichiometric, rutile TiO_2. Thus it can be excluded that the donors are bulk oxygen vacancies.

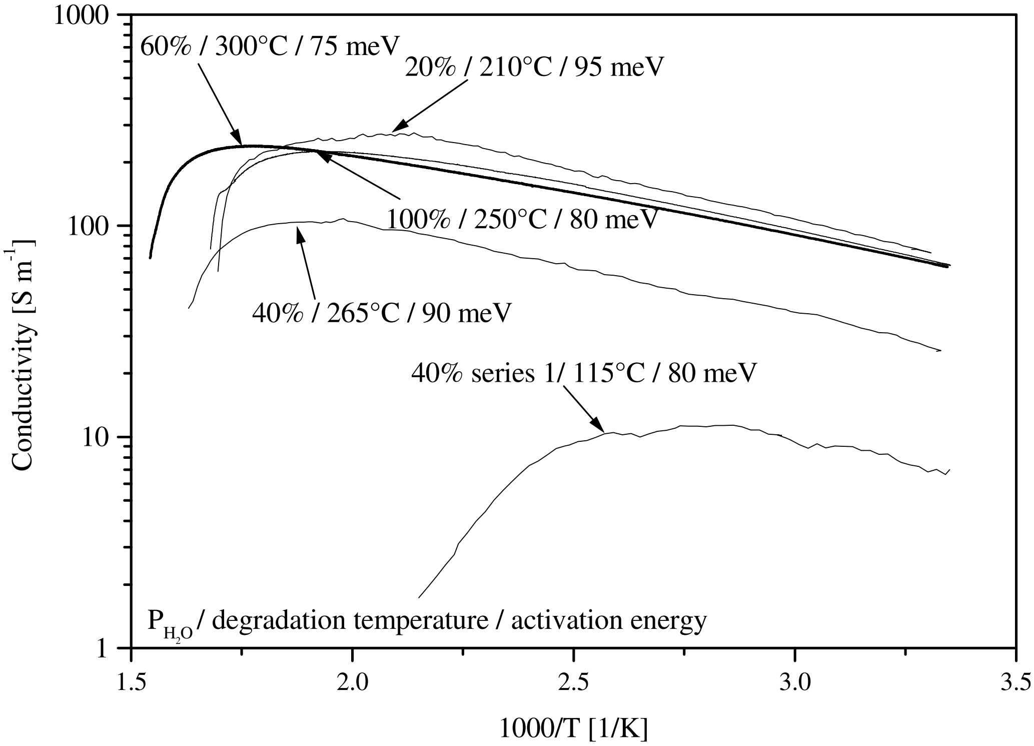

Figure 6.9: Evolution of electrical conductivity as a function of the temperature of TiO_{2-x} thin films deposited with different water vapor partial pressures.

The question, now, is to elucidate the nature and location of the donors. We are looking for an atomic donor concentration of up to 5 % which is related neither to chemical impurities, i.e. to atoms different from Ti and O, nor to point defects inside the bulk of the grains. Extended defects on the grain surfaces are most likely responsible for the high carrier concentrations that can be obtained. Water vapor, by the way of OH radicals, might interfere with the grain growth by blocking oxygen sites during the deposition and thereby modifying the grain boundaries, even if hydrogen eventually disappears before the end of the deposition. Hydrogen could also favor the presence of incompletely oxidized titanium ions at the grain surfaces, and the partially reduced Ti ions may be the electron donors we are looking for.

To investigate the film morphology, impedance measurements were performed in the coplanar geometry. As demonstrated by the current-voltage curves, aluminum contacts should be chosen in order to have ohmic, low resistance contacts. But when ac impedance is measured, its real part (resistance) at 100 Hz is greater than the dc resistance measured with the same contacts, 3200 Ω against 800 Ω. Probably a time longer than the oscillation time used during impedance measurements is necessary to stabilize the electrical contacts and then have ohmic contacts. This time could be related to oxydo-reduction reactions at the titanium oxide/aluminum interface. With gold contacts, which are Schottky contacts, the dc resistance and real part of the ac resistance at 100 Hz are equal. Thus impedance measurements were obtained with gold contacts at voltages low enough to prevent hole injection. The typical dependence of the impedance versus frequency is presented in Figure 6.10. The representation of the imaginary part versus the real part of the impedance is often used when sets of resistances in parallel with capacitors are connected in series, because each contribution is a circle with is center lying on the X-axis. If we try to model this kind of curves, at least three distinct impedances are required to describe the sample measured: one series resistance R_S that shifts the measurements along the X-axis, a complex phase element $R_H\ (i\omega)^{-p}$ in parallel with a resistance $R_{//H}$ (typical of hopping conduction, for example) which gives a circle with its center below the X-axis, and finally a resistance R_P in parallel with a capacity C_P These three impedances were used to model the ac measurements. Measurement obtained at different temperatures are presented in Figure 6.11.

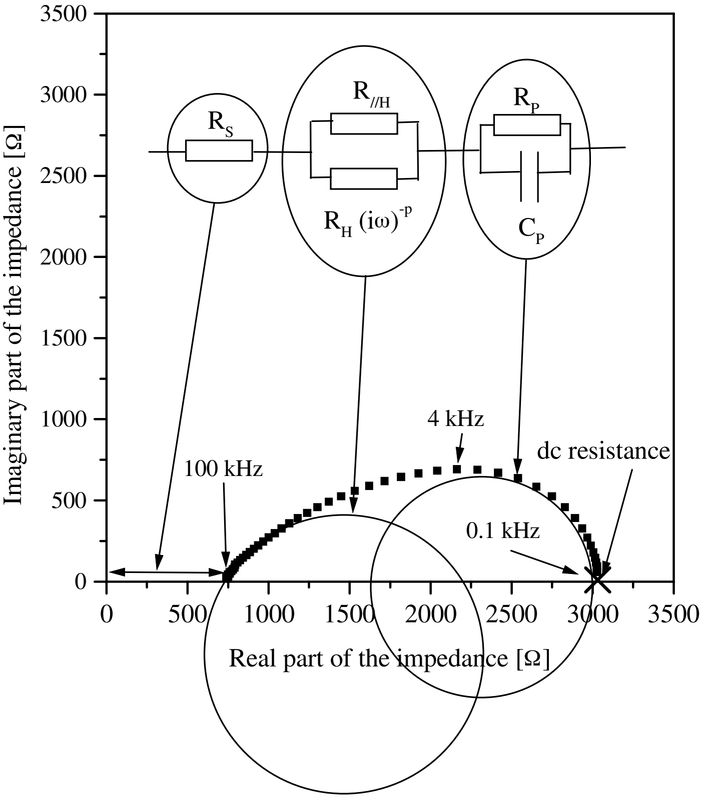

Figure 6.10: Typical ac impedance measurements and corresponding model.

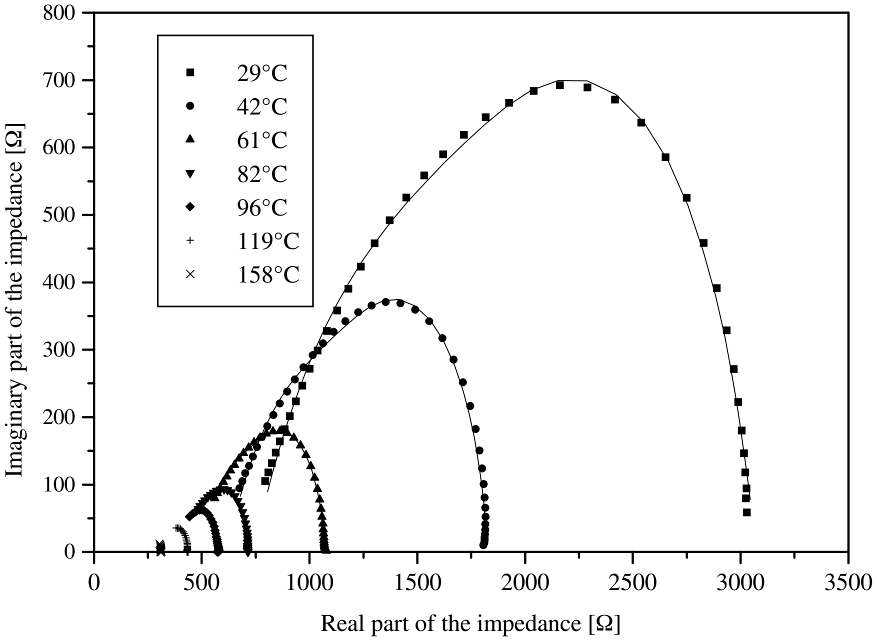

Figure 6.11: ac impedance versus temperature of type W TiO_{2-x} thin film. Lines represent the model fitted to the data.

The evolution of R_S and of the sum of the ac resistances are compared with the dc resistance in Figure 6.12. As mentioned above, the total ac resistance is the same as the dc resistance in the case of gold contacts in a two-contact geometry. The series resistance agrees with the resistance obtained from four-point measurements, therefore it can be assigned to the film resistance, the other impedances being related to the gold contacts. The determination of fit parameters at high temperature is difficult, because the major part of the impedance curve is missing. A capacity is naturally associated with Schottky contacts [15], but the appearance of a complex phase element is unusual. At room temperature, the exponent p value is 0.64, quite the same value as the value obtained in the case of hopping conduction in undoped TiO_2 (0.65, see Chapter 5). This means that in the depletion layer near the contacts, type W TiO_{2-x} behaves as traditional, insulating TiO_2. Depletion layer effects indicate that electrical conduction occurs through the grains rather than along the grain boundaries. The difference between type W TiO_{2-x} and type O TiO_2 indicates therefore the presence of additional charge carriers in the TiO_2 grains. This hypothesis will be corroborated below by optical measurements showing plasmon absorption and a shift of the absorption edge towards high energy in the case of most conducting TiO_{2-x} samples.

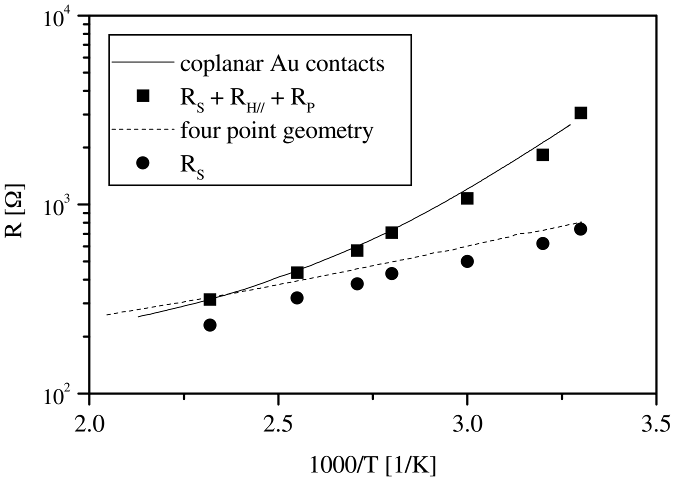

Figure 6.12: dc and ac resistance versus temperature.

6.5 Optical properties

Optical transmission was measured on samples deposited on glass in order to investigate the electronic properties of the films in correlation with electrical measurements. When the electrical conductivity increases the transparency of thin film decreases and finally is lost as the samples turn dark blue. Transmission spectra of type W TiO_{2-x} samples belonging to series 2 are presented in Figure 6.13. Samples with conductivity up to 300 S m^{-1} have a transmission higher than 50% in the whole visible range. It should be noted that 10% of the transmission is lost by reflection. V. N. Bogolomov has described the optical properties of reduced, grey-bluish TiO_2 crystals [16]. He has assigned the color to a broad absorption band whose maximum is near 0.8 eV due to interaction of photons with small polarons. The following relation between the conductivity and the absorption α at 0.82 eV was established: $\alpha\ [cm^{-1}] / \sigma\ [\Omega^{-1}\ cm^{-1}] = 5 \times 100\ \Omega$. This relation predicts a value of $\alpha = 1.5 \times 10^3\ cm^{-1}$ for a sample having a conductivity of 300 S m^{-1}. The observed absorption at 0.82 eV ($1.9 \times 10^4\ cm^{-1}$) is much larger. Therefore the absorption of our conductive samples cannot be accounted for by the polarons described by Bogolomov. The increase of the electrical conductivity of our thin films is accompanied with two modifications of the optical transmission. Firstly the transmission decreases at low energy and secondly the energy absorption edge due to band-gap transitions is shifted to higher energy. In particular, the only sample containing anatase (32% water vapor, 26 S m^{-1}) has the lowest absorption edge energy, while pure, undoped anatase has a larger energy band-gap (3.4 eV) than rutile (3.0 eV).

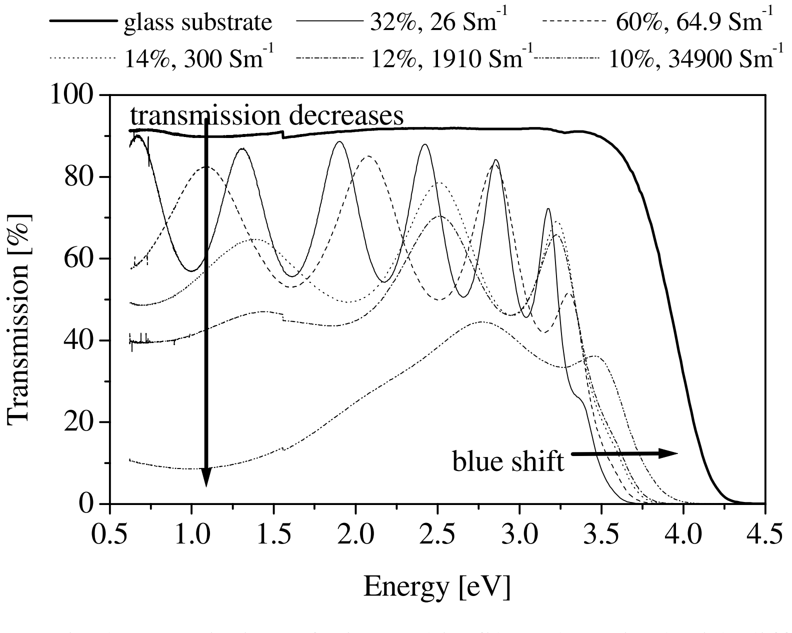

Figure 6.13: Optical transmission of TiO_{2-x} thin films deposited with different water vapor partial pressure.

The optical properties of type W TiO_{2-x} were analyzed in the framework of the effective medium theory, presented in Chapter 5.4.4. The optical properties of anatase, rutile, and titanium, are known. For certain simple morphologies, the effective dielectric constant of thin films can be calculated. The optical properties, in particular the optical transmission, which is most sensitive to any changes in the dielectric constant, can be predicted and compared to the actual measurements. If the predicted values are far from the measured values, the model is declared unsuitable to represent the samples and must be changed.

The four following morphologies have been considered:

A) Spherical, insulating TiO_2 grains coated with metal (Ti or metallic TiO for example)

B) Spherical, metallic precipitates, Ti or TiO, embedded in insulating TiO_2.

C) Spherical grains composed of an insulating TiO_2 nucleus surrounded by a TiO_2 shell containing mobile charge carriers.

D) Spherical TiO_2 grains uniformly filled with mobile charge carriers.

The dielectric constant of spherical insulating TiO_2 (ε_2) grains coated with a volume fraction p_1 of metal (ε_1) can be calculated with the formula given in Chapter 5.4.4 for X_3, see also reference [17]:

$$\varepsilon_{eff} = X_3 = \varepsilon_1 + \frac{3\,(1 - p_1)\,\varepsilon_1\,(\varepsilon_2 - \varepsilon_1)}{3\,\varepsilon_1 + p_1\,(\varepsilon_2 - \varepsilon_1)}$$

the dielectric constant of titanium and rutile are given in reference [18]. The dielectric constant of spherical metallic precipitates (ε_1) in insulating TiO_2 (ε_2) can be calculated with the formula given in Chapter 5.4.4 for Y_3:

$$\varepsilon_{eff} = Y_3 = \varepsilon_2 + \frac{3\,p_1\,\varepsilon_2\,(\varepsilon_1 - \varepsilon_2)}{3\,\varepsilon_2 + (1 - p_1)\,(\varepsilon_1 - \varepsilon_2)}$$

In the cases of morphology C and D we must first calculate the dielectric function of a medium containing free band electrons. The dielectric function is given by the sum the complex susceptibilities associated to the free carriers, the interband transitions and core transitions

$$\varepsilon = 1 + \chi_{free} + \chi_{interband} + \chi_{core}$$

The free carrier susceptibility is modeled here by a simple Drude term as already done in the case of TiN_x thin films [19]. This is an approximation and furthermore one can expect that a small, non-Drude, part of the interband susceptibility may remain buried in the low region of the susceptibility that is dominated by the intraband transitions. According to Drude's theory, for free electron gas, χ_{free} can be expressed as

$$\chi_{free}(\omega) = - \frac{\omega_{free}^2}{\omega\,(\omega + \mathrm{i}\,\Gamma_{free})}$$

where ω_{free}, the plasma frequency of free carriers, is given by

$$\omega_{free}^2 = \frac{n\,q^2}{\varepsilon_0\, m_e^*}$$

where n is the carrier concentration and m_e^* an effective mass describing properties of the Fermi surface. Γ_{free} is the damping term equal to the inverse of the relaxation time. When the carrier concentration increases, ω_{free} also increases, and the reflection region is shifted from the near infrared into the visible resulting in a decrease of the transmission. The dielectric function of TiO_2 single crystals is used to model the interband and core parts of the susceptibility. It is modified around the band-gap energy to take into account the modifications induced by heavy doping. In this study, the modification consists simply in a shift ΔE_g of the absorption edge to higher energy.

The energy shift of the absorption edge has been observed in the case of conducting oxide as SnO_2 already [20]. It results from the competition between the Burstein-Moss effect, i.e. the widening of the optical band-gap resulting from the filling of the bottom of the conduction band by free carriers, and a downward shift of the conduction band which occurs as a consequence of electron-electron and electron-impurity scattering [21]. The band-gap E_g is given by, for a simple electron gas,

$$E_g = E_{go} + \Delta E_{BM} - \Delta E_{ee} - \Delta E_{ei}$$

where E_{go} is the band-gap of undoped semiconductor, ΔE_{BM} the Burnstein-Moss shift, ΔE_{ee} and ΔE_{ei} are the self-energies due to electron-electron and electron-impurity scattering. For a simple electron gas, ΔE_{BM} is given by [21]

$$\Delta E_{BM} = \hbar^2/2m_C^* \,(3\pi^2 n)^{2/3}$$

$$\Delta E_{ee} = q^2 \hbar^2/\pi\varepsilon_o\varepsilon \,(3\pi^2 n)^{1/3}$$

$$\Delta E_{ei} = q^3\, m_C^{*1/2}/(6\,\pi^{1/2}\,(\varepsilon_o\varepsilon)^{3/2}\,\hbar\,)\,(3\pi^2 n)^{1/6}$$

where m_C^* is the conduction band, density-of-states, effective mass, and n the free carrier concentration.

In the case of morphology C, the effective dielectric constant ε_{eff} of the mixture of nucleus insulating TiO_2 (ε_1, p_1) and shell TiO_2 (ε_2, p_2) filled with charge carriers is calculated with the

Bruggeman effective medium approximation [22]:

$$\sum_{\mathrm{i}} p_i \frac{\varepsilon_i - \varepsilon_{eff}}{\varepsilon_i + 2\,\varepsilon_{eff}} = 0$$

The four morphology models were tested in the case of rutile sample prepared with 60% of water vapor belonging to series 2. The results are presented in Figure 6.14. The optical constants of rutile and titanium are given in reference 23. The transmission calculated with insulating rutile grains (solid line) is too large and the absorption edge arises at a lower energy than the measured absorption edge. The model of spherical insulating TiO_2 grains coated with a volume of 3% of titanium produces a transmission (dashed line) lower than the measured transmission. As expected, the absorption edge is lower than in the case of pure a rutile grains. The same behavior is obtained if titanium is replaced by metallic TiO. Similar results were obtained in the case of the B model. Therefore, the A and B models are not valid to interpret the measured transmission. The shift of the absorption edge is the critical point to test the models. In the case of morphology C, if the volume fraction of the insulating nucleus is larger than 70%, the absorption edge shift cannot be reproduced whatever the band-gap shift one imposes on the rutile shell material. We can obtain a satisfactory fit of the measured transmission with model C (dotted line) using a nucleus volume of 70%, but the band-gap shift of 0.5 eV necessary to produce this result is too large and unrealistic. Model D gives a transmission similar to model C with a reasonable shift of 0.1 eV. Thus model D, which corresponds to spherical TiO_2 grains uniformly filled with additional electrons, is the model adopted to describe our system. The charge carriers are supposed to originate from unsaturated titanium bonds at the grain surfaces.

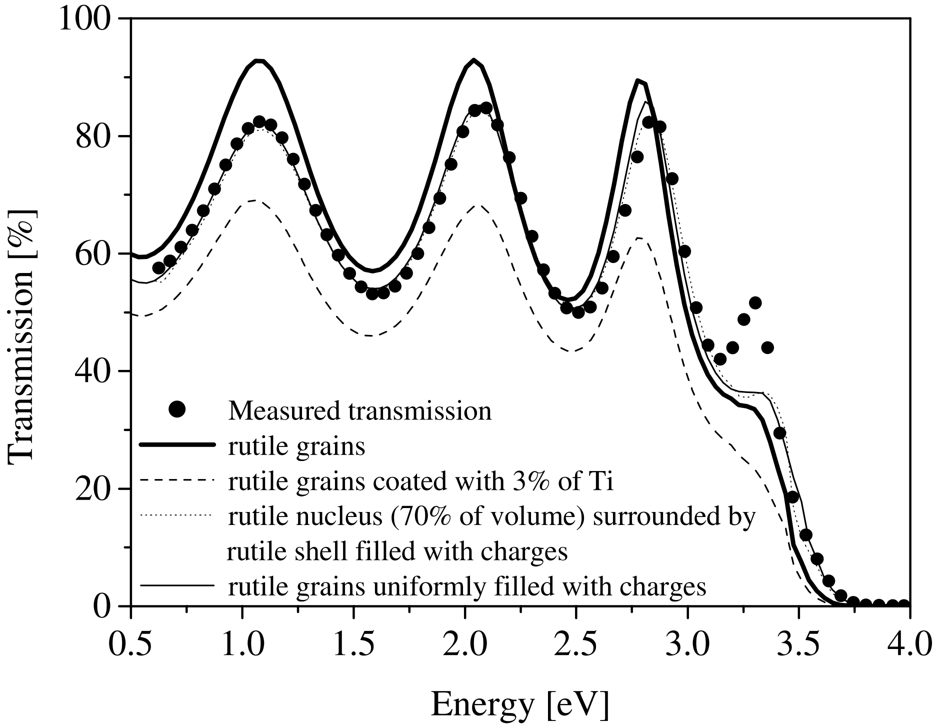

Figure 6.14: Comparison between measured transmission (circles) of a sample 225 nm thick prepared with 60% of water vapor and transmission calculated with pure rutile grains (thick solid line); model A with 3% of Ti (dashed line); model C with 70% of TiO_2 nucleus, ω_{free} = 1.5 eV, Γ_{free} = 2.4 eV, ΔE_g = 0.5 eV (dotted line); model D with ω_{free} = 0.8 eV, Γ_{free} = 2.4 eV, ΔE_g = 0.1 eV (thin solid line).

A few transmission spectra calculated with this model are reported in Figure 6.15. The model is satisfactory in the case of samples having conductivity lower than 1000 S m^{-1}, excepted near the band-gap energy where a more detailed description is necessary to model the first interference fringe. The shift of the absorption edge is one of the effects of heavy doping, but an accurate model should also contain a description of a tail at the bottom of the conduction band that results from fluctuations in the doping concentration. In the case of highly conductive samples, the model is not entirely successful, but we have to remember that a) the most conductive sample is amorphous b) the sample which has a conductivity of 1910 S m^{-1} may also contain a significant fraction of an amorphous phase with unknown optical properties and c) in heavily doped, metallic samples new interband transitions take place between occupied conduction band states and higher, unoccupied conduction states.

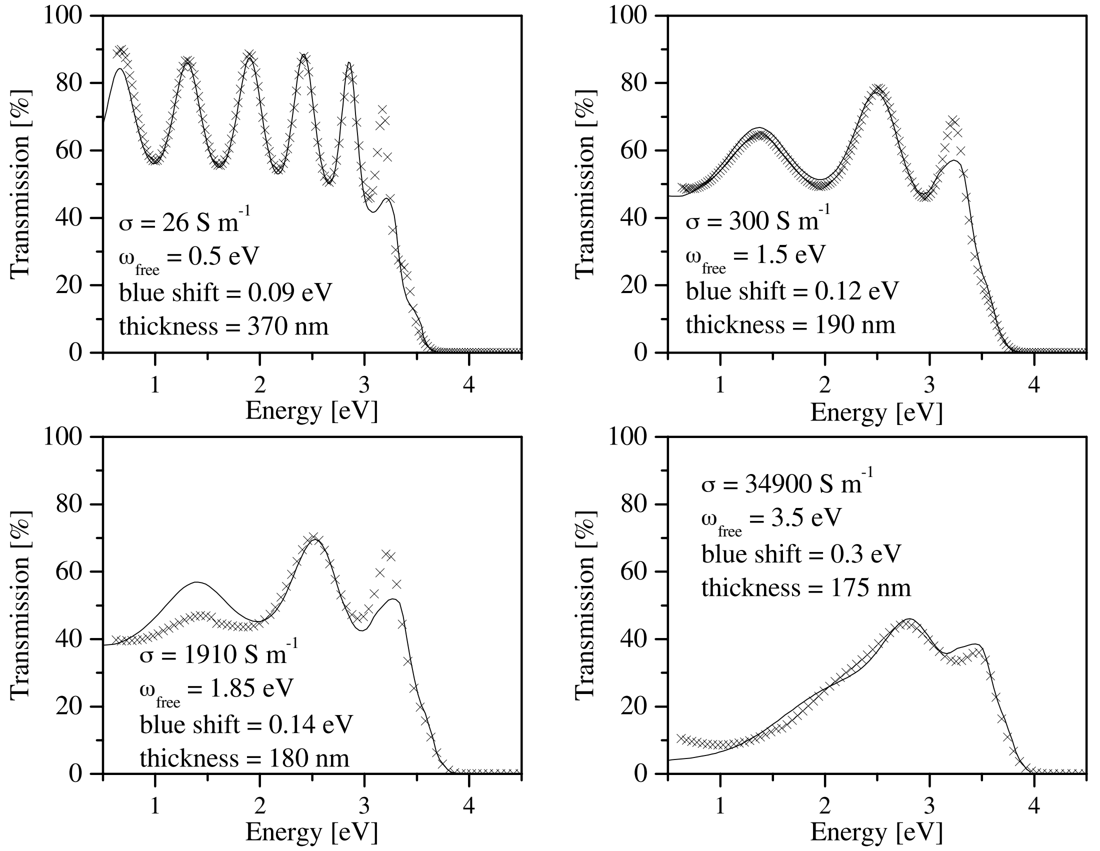

Figure 6.15: Comparison between measured transmission (crosses) of type W TiO$_{2-x}$ and predicted value from the model described above (solid line).

The optical conductivities $\sigma(\omega) = \varepsilon_0\ \varepsilon_2\ \omega$, where ε_2 is the imaginary part of the dielectric function, corresponding to the transmission calculated above are reported in Figure 6.16. The influence of the plasmon on the electrical conductivity can clearly be seen at low energy where the optical conductivities (solid lines) are equal to the plasmon contribution (dotted lines). At higher energy, the interband transition contributions become the dominant term of the optical conductivity. The blue shift of the absorption edge is visible at high energy.

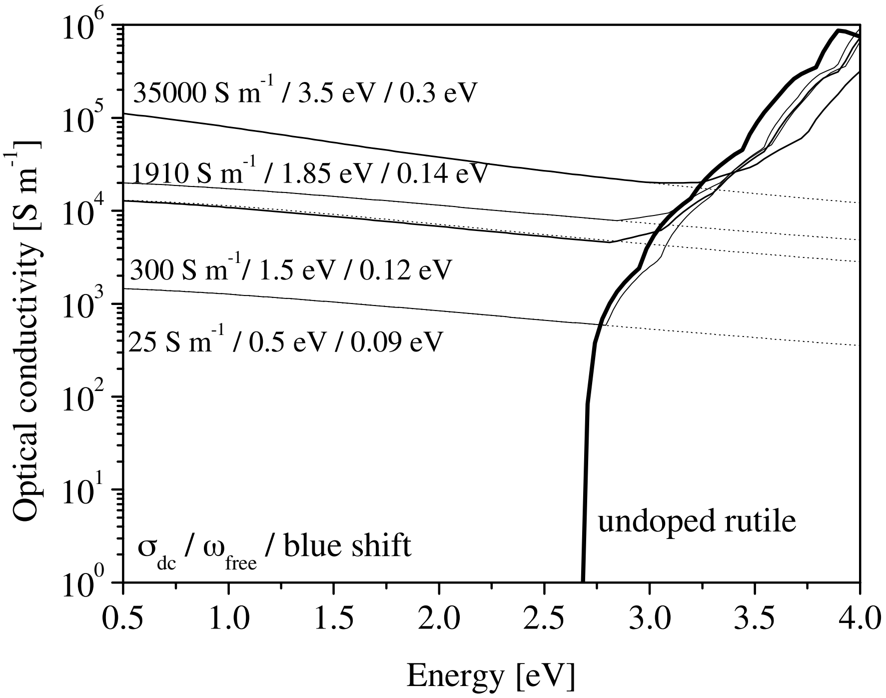

Figure 6.16: Comparison between the optical conductivity of undoped rutile and type W TiO_{2-x} with different electrical conductivity. The dotted lines represent the plasmon contribution to the optical conductivity.

In principle the donor concentration can be modeled from the stoichiometry, and the electrical conductivity provides the product of the charge carrier concentration times the mobility. Figure 6.17 shows conductivity against chemical composition for several samples. It turned out to be difficult to find a simple relation between chemical composition and electrical conductivity. Clearly there was a problem with the standards using for EPMA measurement. Indeed EPMA measurements sometimes gave strange results such as overstoichiometric $TiO_{2.12}$. This proves that the standard samples were actually reduced from prolonged electron bombardment. The oxygen content measured appeared to increase from one measurements session to the next, as if the standard were reduced with time. For these reasons the evolution of the plasma frequency was compared to the electrical conductivity rather than to the chemical composition.

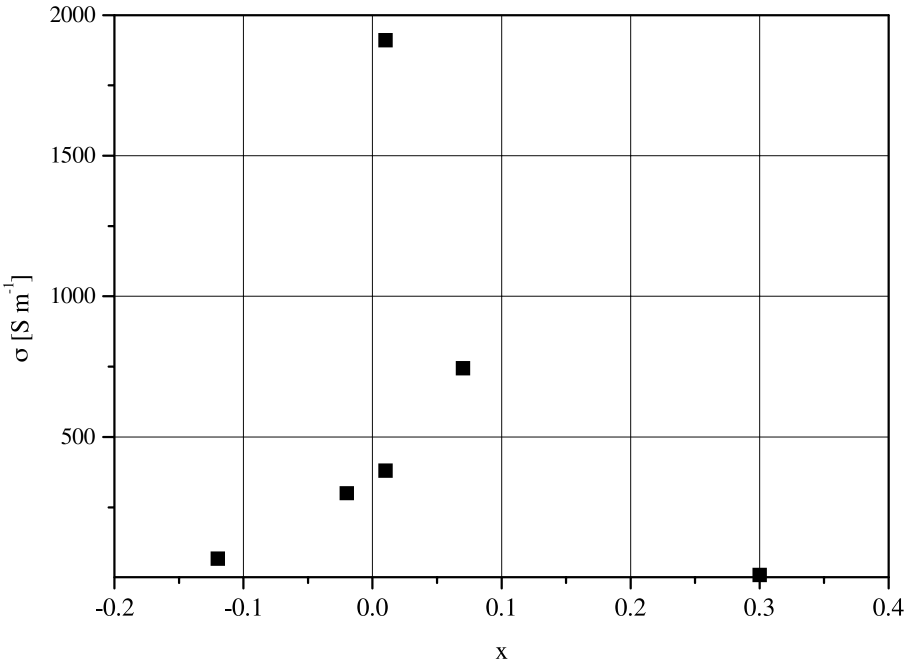

Figure 6.17: Electrical conductivity versus the EPMA chemical composition for type W TiO_{2-x}.

The square of the plasma frequency varies linearly with the carrier concentration. It is also a linear function of the conductivity when it is lower than 1000 S m^{-1} as shown in Figure 6.18 (a). If we consider a particular sample having a reliable chemical composition $TiO_{1.93}$, which corresponds to a carrier density of 4.5 x 10^{27} m^{-3}, and the associated plasma frequency ω_{free} = 1.7 eV, we can calculate the effective mass m_e^* = 2.2 m_e. This value of m_e^* is lower than values usually reported by some authors for effective mass of rutile crystals, namely 9-13 m_e [24]. The optical conductivity $\omega_{free}^2/\varepsilon_0\Gamma_{free}$ is higher than the dc electrical conductivity as reported in Figure 6.18 (b). Under optical electric fields, electrons move over small distances, much smaller than the grain size and therefore the observed conductivity reflects the conductivity of the grain bulk material. On the contrary, during dc measurements, the electrons must cross the grain boundaries and the conductivity appears to be smaller because of the presence of interfacial energy barriers. The dumping term Γ_{free} used to model the optical transmission varies between 2.0 and 2.5 eV. This value corresponds to an optical mobility $\mu_{opt} = q / (\Gamma_{free}\ m_e^*)$ varying between 0.21 and 0.26 x 10^{-5} m^2/Vs in accordance with mobility values measured in rutile TiO_2 thin films [24]. According to Orton and Powell, if the charge density inside the grain is larger than the density of charge trapped in surface states, the apparent mobility can be thermally activated taking into account barriers encountered by the charges at grain boundaries [25]. Therefore the picture of heavily doped grains by donors situated in the grain boundaries is reasonable. The scattering effect of grain boundary is visible on the dc electrical conductivity. The activation energy of the electrical conductivity varies between 20 meV and 95 meV. The lowest values are obtained in the most conductive samples in accordance with the decrease of the barrier height when the charge density increases. The lost of the linear relation between ω_{free}^2 and the dc conductivity can be attributed to the increase of the mobility with the carrier concentration.

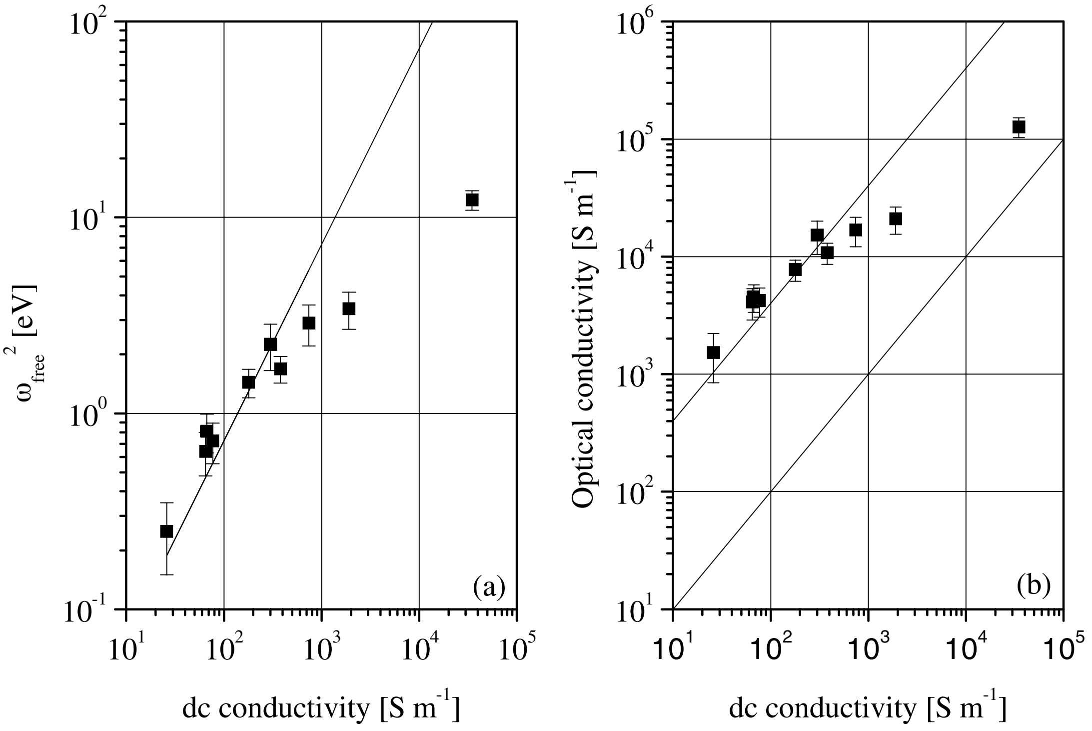

Figure 6.18: (a) Square of plasma frequency ω_{free}, (b) optical conductivity versus dc electrical conductivity.

The blue shift of the forbidden gap absorption edge is plotted versus ω_{free}^2 in Figure 6.19. The straight line represents the Burnstein-Moss shift calculated with the charge density deduced from the plasma frequency. The observed blue shift is smaller than the calculated Burnstein-Moss shift indicating that self-energies due to electron-electron ΔE_{ee} and electron-impurity scattering ΔE_{ei} give important contributions to the shift of the absorption edge. Attempts to interpret the shift with electron gas expressions of ΔE_{ee}, ΔE_{ei} calculated for a parabolic conduction band [21] failed. The formation of a tail due to disorder effects and/or amorphicity below the conduction band must be taken into account to estimate the absorption edge shift of heavily doped material [26].

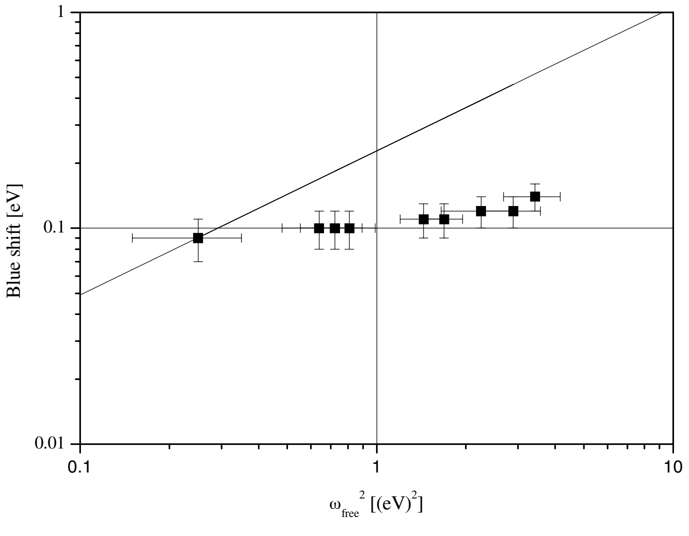

Figure 6.19: Shift of the absorption edge versus the square of the plasma frequency.

6.6 Conclusion

Transparent, conductive TiO_2 thin films, with conductivity close to 100 S m^{-1}, which can withstand 300 °C, can be produced by replacing oxygen by water vapor as reactive gas. This is a great step comparing to the TiO_2:Nb discussed in Chapter 5 where only 0.001 S m^{-1} have been reached. The essential difference between thin films deposited with water vapor and oxygen can be assigned to the grain boundary composition. It is proposed that water vapor creates unsaturated titanium bonds at the grain surfaces. Partly reduced, surface Ti atoms in turn inject electrons into the bulk of the crystallites, increasing in this way the electrical conductivity of TiO_{2-x}. An essential ingredient that makes such films possible is the nanometric grain size. Indeed in a thin film formed of 5 nm spherical grains, nearly 15% of the Ti atoms are located on the grain boundaries. This is how it is possible to reach much higher doping levels (10^{28} m^{-3}) than in bulk doping. More detailed structure, morphology and chemical analyses are necessary to elucidate the electrical conduction mechanisms. Open areas for further work also include using O_2 and H_2 mixtures as reactive gas, and further investigations of chemical doping coupled with sputtering under water vapor.

Probably, this study shows that when the grain size is very small, new properties can appear compared to bulk material.

Bibliography

[1] Y. Shigesato, Y. Hayashi, A. Masui, and T. Haranou, Japanese Journal of Applied Physics 30 (1991), 814.

[2] E. Nishimura, M. Ando, K.-I. Onisawa, M. Takabatake, and T. Minemura, Japanese Journal of Applied Physics 35 (1996), 2788.

[3] T. Nakada, Y. Ohkubo, and A. Kunioka, Japanese Journal of Applied Physics 30 (1991), 3344.

[4] K.-I. Onisawa, E. Nishimura, M. Ando, T. Satou, M. Takabatake, and T. Minemura, MRS 1996 Spring Meeting, Material Research Society Symposium Proceeding Vol. 424 (1997), 341.

[5] K.-H. Hellwege, Landolt-Börnstein III/7b1, Springer Verlag, Berlin (1975), 289.

[6] A. R. Bally, P. Hones, R. Sanjinés, P. E. Schmid, and F. Lévy, Surface and Coatings Technology 108-109 (1998), 166. Paper reported in Appendix C.

[7] N. Martin and C. Rousselot, Journal of Vacuum and Science Technology A 17 (1999), 2869.

[8] S. Kadlec, J. Musil, and J. Vyskocil, Vacuum 37 (1987), 729.

[9] J. D. DeLoach and C. R. Aita, Journal of Vacuum Science & technology A 16 (1998), 1963.

[10] X. Wei-Xing, Z. Shu, and F. Xian-Cai, Journal of Physics and Chemistry of Solids 59 (1998), 1647.

[11] T. W. Hickmott, Journal of the Electrochemical Society 113 (1966), 1223.

[12] T. W. Hickmott, Journal of Applied Physics 37 (1966), 4380.

[13] J. B. Goodenough, A. Hammett, G. Huber, F. Hulliger, M. Leiss, S. K. Ramasesha, and H. Werheit, Landolt-Börnstein III/17g, Springer Verlag, Berlin (1984).

[14] M. Kitao, Y. Oshima, and K. Urabe, Japanese Journal of Applied Physics 36 (1997), 4423.

[15] S. M. Sze: “Physics of Semiconductor devices”, Wiley Interscience, New York (1981).

[16] V. N. Bogomolov, E. K. Kudinov, D. N. Mirlin, and Y. A. Firsov, Soviet Physics - solid State 9 (1968), 1630.

[17] G. W. Milton, Applied Physics Letters 37 (1980), 300.

[18] E. D. Palik: “Handbook of Optical Constants”, Academic Press, New York, 1985.

[19] P. E. Schmid, M. S. Sunaga, and F. Lévy, Journal of Vacuum Science and Technology A 16 (1998), 2870.

[20] G. Sanon, R. Rup, and A. Mansingh, Physical Review B 44 (1991), 5672.

[21] B. I. Shklovskii and A. L. Efros: “Electronic Properties of Doped Semiconductors”, Solid-State science 45, Springer Verlag, Berlin (1984).

[22] D. A. G. Bruggeman, Annal of Physics 24 (1935), 636.

[23] E. D. Palik: “Handbook of Optical Constants”, Academic Press, New York (1985).

[24] H. Tang: “Electronic properties of anatase TiO_2 investigated by electrical and optical measurements on single crystals and thin films”, Thèse EPFL N° 1311, Lausanne (1994).

[25] J. W. Orton and M. J. Powell, Reports on Progress in Physics 43 (1980), 81.

[26] P. E. Schmid, Physical Review B 23 (1981), 5531.

Chapter 7

Conclusions and perspectives

The present work was based on titanium oxide thin films deposited by reactive sputtering. The first part of the work consisted in finding appropriate impurities to improve the electrical properties of TiO_2 thin films, thereby producing more insulating or more conducting films than the films produced without intentional doping. The second part consisted in characterizing the sample properties in order to explain the modifications of the electrical properties, and to isolate the factors limiting the conductivity. From the physicist's point of view the second part is the most rewarding part of the work, but it could start only after interesting samples were produced.

The attempts to modify TiO_2 followed two axes: the modification of the target used as starting material, and the modification of the reactive gas used during the deposition. Niobium, cerium, and iron doping have been achieved with oxide powders incorporated in the metal titanium target. Water vapor has been used as reactive gas. The results obtained with the different doping methods are summarized below:

- Niobium doping produces conducting TiO_2 with an n-type conductivity of 10^{-3} S m^{-1} for 2.9 at.% of niobium, three orders of magnitude higher than undoped TiO_2 (10^{-6} S m^{-1}). The niobium atoms act as donors impurities, but the weak increase of the conductivity compared to the large amount of atoms incorporated inside TiO_2 indicates that a majority of the electrons are trapped by defects created by the niobium dopant itself. The crystalline structure changes from anatase to rutile when the niobium concentration increases.

- Cerium doping decreases the conductivity of TiO_2. The film structure changes from anatase to amorphous for cerium contents higher than 1.2 at.%. It has been demonstrated that cerium atoms act as electron traps and that the same amount of oxygen vacancies as cerium atoms is created so as to accommodate the large size of the cerium atoms. The size mismatch and the multivalence of Ce are responsible for the amorphization of the thin films at high cerium concentration. Insulator thin films made of TiO_2:Ce present a high dielectric constant at rf frequencies ($\varepsilon = 45$), a low electrical conductivity (10^{-9} S m^{-1}), and an electrical breakdown at electric field three times higher than in undoped TiO_2 (2 x 10^{-7} V/m). The incorporation of such insulators in electroluminescent devices decreases the threshold voltage of the luminescence, because the dielectric constant of TiO_2 is higher than that of the traditional insulator Y_2O_3 ($\varepsilon = 12$), and the use of TiO_2 increases the brightness saturation. The use of TiO_2:Ce can surely be spread out to other devices that can benefit from insulators with a high dielectric constant.

- Iron doping produces TiO_2 with p-type electrical conductivity if the iron content is large enough. Iron atoms act as electron acceptors. The iron concentration must be larger than twice the oxygen vacancy concentration (0.13 at.% of iron in enough in our case) before the electrical conductivity changes to p-type When the iron concentration increases, the structure changes from anatase to rutile and at the same time, the ratio of oxygen vacancies created per iron atom decreases. The highest p-type conductivity obtained with iron doping was only 2 x 10^{-6} S m^{-1}. The major problem comes from the high oxygen vacancy concentration which produces too many electrons. Co-doping with iron and fluorine was attempted and a sample with p-type conductivity of 10^{-4} S m^{-1} was realized.

- Depositions made with water vapor as reactive gas produce conductive, transparent TiO_{2-x}. Samples with transmission higher than 50% in the visible range with an electrical conductivity around 300 S m^{-1} were routinely obtained in this way. It is far away from the conductivity of transparent conducting oxides such as ITO, SnO_2 or ZnO that lie around 10^6 S m^{-1}. Nevertheless, it is a great step compared to undoped TiO_2 deposited with oxygen which culminated at 10^{-4} S m^{-1}. The conductivity increase in not the result of traditional doping. It is made possible by the very large grain boundary area available on nanometric-grain materials, on which unsaturated titanium bonds could act as donors. A high carrier concentration is possible when the grains are small, say, less than 15 nm, in which case more than 5% of the atoms are located on the grain surface. The better samples are stable on heating in the air up to 300°C, which can be of use in many applications, such as gas sensors, in photocatalysis or photoelectric devices.

N-type, p-type, and insulating TiO_2 could be produced by impurity incorporation or morphology modification. It is important to mention that among all titanium dioxide samples produced, the electrical conductivity varied from 10^{-10} to 10^{3} S m^{-1} at room temperature, i.e. over 13 orders of magnitude.

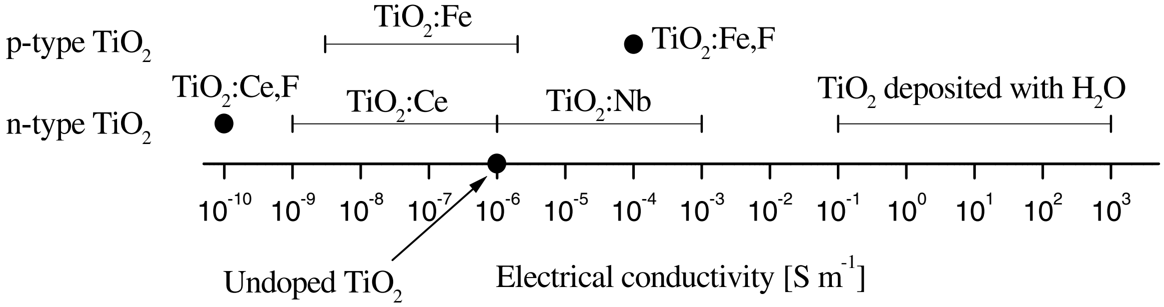

It is interesting to note that the insulating layers composed of amorphous TiO_2 or of anatase possess a dielectric constant lower than that of rutile. It is also worth noting that the highly conducting thin films have rutile as the major phase, which has a lower electrical mobility than anatase. Impurity incorporation is always accompanied by defect formation that limits the electrical conductivity by trapping the charge carriers. To obtain more conductive thin films, multiple doping should be attempted, with impurities that give the charge carriers and other impurities that neutralize the defects or prevent the defects formation. A combination of iron and fluorine gave a more conductive p-type TiO_2 than iron-doped TiO_2. When the grain size decreases, the fraction of atoms belonging to the grain surfaces becomes more and more important and new properties can be obtained. It is illustrated by the conductivity increase obtained when oxygen is replaced by water vapor during the deposition. In this case, the major differences are situated in the grain boundaries rather than inside the grains. Thus the control of the film morphology is a major challenge to modify the electrical properties of the material.

Up to now, we have no indications that transparent TiO_{2-x} deposited with oxygen can show an electrical conductivity as high as in the case of TiO_{2-x} deposited with water vapor. H_2O is interesting from the technical point of view, because of the large range of deposition parameters leading to conductive thin films. Reactive sputtering using H_2O as reactive gas opens new perspectives for titanium oxide thin film fabrication and possibly also for other oxide materials.

Appendix A

Papers on cerium doped TiO_2

Jpn. J. Appl. Phys. Vol. 36 (1997) pp. 5696–5702
Part 1, No. 9A, September 1997

Ce-doped TiO_2 Insulators in Thin Film Electroluminescent Devices

Kshem PRASAD[1], Alain R. BALLY[1,*], Philippe E. SCHMID[1], Francis LÉVY[1], Jacques BENOIT[2], Carlos BARTHOU[2] and Paul BENALLOUL[2]

[1] *Institut de Physique Appliquée, Ecole Polytechnique Fédérale de Lausanne, 1015 Lausanne, Switzerland*
[2] *Laboratoire d'Acoustique et Optique de la Matière Condensée, Université Pierre et Marie Curie,*
Case N 80, 4 Place Jussieu, 75252 Paris, France

(Received January 27, 1997; accepted for publication June 30, 1997)

Cerium-doped TiO_2 thin films have been prepared by reactive RF sputtering. At low Ce concentration, X-ray diffraction indicates that the films have the anatase structure. Ce concentrations higher than 1.2 at.% result in an amorphization of the film which remains stable up to 873 K. The TiO_2 electrical properties have been stabilized and improved by cerium doping, resulting in a lower conductivity ($10^{-9}\,\Omega^{-1}\mathrm{m}^{-1}$), a higher electrical breakdown strength (2×10^7 V/m), and a high value of the permittivity (45 ± 5). The implementation of amorphous TiO_2:Ce thin films as insulator layers in ZnS:Mn alternating current thin film electroluminescent devices (ACTFELD) results in a significant drop in the threshold operating voltage and a notable increase in the device brightness compared with ACTFELD containing Y_2O_3 or $BaTa_2O_6$ insulator layers. Rapid thermal annealing further improves the performance of the electroluminescent device.

KEYWORDS: titanium oxide, cerium, insulator, thin film, electroluminescent device

1. Introduction

Alternating current thin film electroluminescent devices (ACTFELD) provide an attractive alternative for solid-state flat panel displays.[1)] They offer a high contrast, a wide viewing angle, the possibility of high resolution and fast response for video applications. Dielectric materials play a decisive role in the performance of these MISIM type structures[1–3)] (M = metal electrode, I = insulator, S = semiconducting phosphor). Under actual operating conditions, very high electrical fields of the order of 1–2 $\times 10^8$ V/m are applied to the phosphor layer. The role of the dielectric is to prevent device breakdown by carrier injection under these high fields and to keep charge carriers suitably trapped in interface states so that they do not leak out into the phosphor at lower fields. Most important of all, a dielectric with a high permittivity lowers the device operation voltage as it concentrates a large fraction of the external bias in the light-emitting layer. It leads to lower power consumption in both devices and addressing circuits, which in turn can be controlled by lower voltage drivers.

A number of studies have reported[4)] attempts at finding suitable dielectrics for ACTFELD applications having the highest figure of merit, which has been defined as the product of dielectric constant and breakdown electric field $\varepsilon_0 \varepsilon E_{\mathrm{bd}}$. This figure of merit, which corresponds to the maximum trapped charge density for an insulator material, is of the order of 4–6 μC/cm^2 in classical electroluminescent devices (ELD).[5)] Most dielectrics having a high permittivity turn out to be unsuitable due to their low breakdown strength. Because of its high permittivity, TiO_2 is a potential candidate provided its conductivity can be kept low enough. Like many oxides, however, undoped TiO_2 is always slightly substoichiometric and oxygen vacancies generate charge carriers. A figure of merit of only 1 μC/cm^2 has been reported for atomic layer epitaxy prepared TiO_2[5)] corresponding to a high permittivity (60) but a low breakdown field (0.2×10^8 V/m). It has been proposed to overcome this problem by having recourse to mixed dielectrics such as Al_2O_3/TiO_2.[6)] We have recently improved the resistivity and stability of TiO_2 by Ce doping. A 2.1% Ce concentration leads to an increase of the resistivity of TiO_2, an increase of the breakdown voltage, and a reduced variation of the permittivity with frequency. A frequency-independent constant value between 35 and 45 is obtained for the permittivity. In this paper we report on the electrical properties of TiO_2:Ce and present the results of our investigations of this new insulator for ACTFELD applications. TiO_2:Ce thin films have been integrated as dielectric layers in standard ACTFELD structure using ZnS:Mn as phosphor. The performance of the TiO_2:Ce devices is compared with that of standard devices using Y_2O_3 insulators ($\varepsilon = 12$), and with an experimental device based on the high permittivity dielectric $BaTa_2O_6$ ($\varepsilon = 22$).

2. Experimental Details

Two types of structures have been prepared for the present study. For ac and dc electrical measurements thin films of undoped and Ce-doped TiO_2 have been deposited on glass coated with indium-tin oxide (ITO) by reactive RF sputtering in a 1/2 oxygen/argon mixture. Ce doping was achieved by sputtering from a composite Ti (purity 99.5%) target comprising small CeO_2 (purity 99.9%) sections. The deposition conditions are reported in Table I. Gold dots (2 mm^2) were evaporated on top of the film as electrical contacts. Electrical measurements were carried out in this transverse geometry (ITO/TiO_2:Ce/Au). The dc electrical conductivity was determined by measuring the current across the thin films under a constant voltage of 0.1 V. An oscillation level of 0.1 V_{rms} was used for the ac measurements. The structure of the films was investigated by X-ray diffractometry in a grazing angle configuration ($\theta = 3°$). Electron probe microanalysis (EPMA) was used to establish the chemical composition of Ce-doped films. A thin layer

---

*E-mail address: bally@ipasg.epfl.ch

of carbon was evaporated on the film to avoid electrical charging during the EPMA measurements. Rutile TiO_2 and $CePO_4$ crystals were used as standards for the calibration.

For electroluminescence investigations, MISIM structures were fabricated on ITO-coated glass.[5] Table II gives the details of each device configuration. The standard Y_2O_3 insulator layers have been prepared by e-gun evaporation under a pressure of 2×10^{-5} Torr of oxygen. Due to its high permittivity, $BaTa_2O_6$ is another insulator which is considered for use in ELD. In the present study, $BaTa_2O_6$ was deposited by reactive RF sputtering from a ceramic target in an ambient composed of 20% of oxygen and 80% of argon. The Mn-doped ZnS phosphor layer was prepared by e-gun evaporation of ZnS with simultaneous thermal evaporation of MnS. The Mn concentration was estimated, from the luminescence decay curves, to about 0.7 at.%.[7] Standard aluminum dots with an area of 2 mm^2 were evaporated as top metal contacts. Devices A, B and C were subjected to a long thermal annealing (LTA) for 2 h in vacuum at 400°C after the deposition of ZnS:Mn. Such a post-deposition heat treatment of ZnS:Mn is widely used to improve the electroluminescent brightness by increasing both excitation and radiative efficiencies.[5] In order to reduce atomic inter-diffusion between adjacent layers and to produce symmetrical interfaces, one type of device (D) was subjected to a rapid thermal annealing (RTA) for 45 s at 400°C before the Al electrode deposition. The brightness was measured using a Minolta Photometer. A sinusoidal 1 kHz voltage source was used as the excitation source. The brightness threshold voltage V_{th} reported in Table III is defined as the voltage required (or extrapolated) for a brightness of 1 cd/m^2. The transferred charge Q_t as a function of applied voltage was determined by measuring the stored charge in the sense capacitor of a Sawyer-Tower circuit.[8] It should be noted that in this work the phosphor composition was not optimized and therefore the total brightness level is less than what is generally reported.[5] Valid comparisons can nevertheless be obtained since all phosphor layers were prepared under identical deposition conditions. The Mn concentration was comparable in all devices, and they all presented the same photoluminescence decay time (~200 μs). This ensures that they all exhibited the same radiative efficiency.

3. Results and Discussion

3.1 *Structural characterization*

Undoped TiO_2 films were deposited at a substrate temperature of 540 K. Figure 1 shows the corresponding X-ray diffraction (XRD) patterns for three different thicknesses (260, 420 and 790 nm). Curves A and B illustrate the spectra obtained from the thinnest film deposited on glass and on ITO-coated glass, respectively. On glass substrates, the films crystallized in the anatase phase with an average grain size of 17 nm that was determined from the full width at half the maximum (FWMH) of the most intense peak $(101)_a$. The films grown on ITO (curve B) exhibit two additional peaks located at 27.4° and 41.2° which are associated with the $(110)_r$ and $(111)_r$ planes of the rutile phase. The remaining peaks belong to the ITO underlayer. The average grain size in the rutile phase is 14 nm (determined from the FWMH of the $(110)_r$ peak). A similar behavior is observed on thicker films deposited on ITO as illustrated in curves C and D.

Table I. TiO_2:Ce deposition parameters.

Ce concentration (at.%)	Substrate temperature (°C)	RF power (W)	CeO_2 area/ total area (%)	Deposition rate (Å/s)
0.0	270	900	0	0.50
0.3	280	900	1.8	0.66
0.4	260	1000	0.36	0.14
1.2	270	750	1.44	0.08
1.8	265	900	2.56	0.21
2.0	265	900	2.56	0.18
2.1	265	900	2.56	0.17
2.3	265	900	2.56	0.17

Table II. Electroluminescent device configurations.

Device	Insulator 1	Phosphor	Insulator 2	Thermal treatment
A Standard	Y_2O_3 Thickness 330 nm	ZnS:Mn 520 nm	Y_2O_3 360 nm	LTA
B Asymmetrical	$BaTa_2O_6$ 330 nm	ZnS:Mn 520 nm	TiO_2:Ce 270 nm, 1.8 at.% Ce	LTA
C Symmetrical	TiO_2:Ce 300 nm[a]	ZnS:Mn 520 nm	TiO_2:Ce 270 nm, 1.8 at.% Ce	LTA
D Symmetrical	TiO_2:Ce 230 nm, 2.0 at.% Ce	ZnS:Mn 520 nm	TiO_2:Ce 220 nm, 2.3 at.% Ce	RTA

a) Ce concentration was not determined on this layer.

Table III. ACTFELD parameters.

Device	V_{th} ($V_{0\text{-}p}$)	$V_{peak}^{a)}$ ($V_{0\text{-}p}$)	$B^{a)}$ (cd/m^2)	$Q_t^{a)}$ (μC/cm^2)	L_{30} (cd/m^2)	dQ_t/dV (μC/V cm^2)
A	140	240	225	3.92	55	0.115
B	60	184	460	6.97	9	0.091
C	80	132	328	3.92	60	0.330$^{b)}$
D	85	134	455	7.33	322	0.330

a) these values refer to the marked points in Figs. 6(a) and 6(b)
b) between 110 and 125 V only

Table IV. Numerical values for dc conductivity.

Ce concentration (at.%//cm^{-3})	0 // 0	0.3 // 2.6 × 10^{20}	2.1 // 1.9 × 10^{21}
O vacancy concentration (cm^{-3})	1 × 10^{19}	2.6 × 10^{20}	1.9 × 10^{21}
O vacancy shallow level (eV)		< 0.2	
O vacancy deep level (eV)	0.65	0.65	0.6
Intrinsic trap concentration (cm^{-3})		1.01 × 10^{19}	
Energy gap (eV)$^{12)}$		3.20	
Mobility (10^{-4} m^2/V s)	0.3	0.3	0.0001
Conduction band density of states (cm^{-3})		1 × 10^{20}	

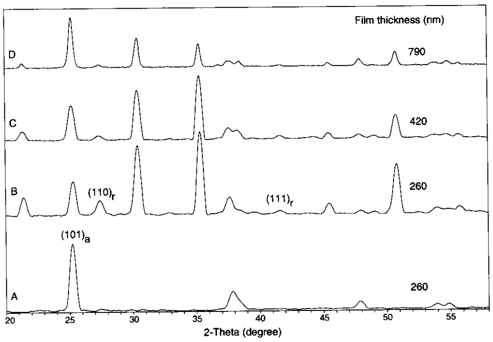

Fig. 1. X-ray diffraction spectra of undoped TiO_2 for three different film thicknesses.

The intensity of the $(101)_a$ anatase peak increases with film thickness while the peak intensities corresponding to rutile decrease. In mixed anatase/rutile TiO_2 thin films the weight fraction W_a of the anatase phase was estimated from the relation $W_a = 1/(1 + 1.265 I_R/I_A)$ proposed by Spurr,$^{9)}$ where I_R/I_A is the ratio of the most intense peaks of the rutile and anatase phases ($(110)_r$ and $(101)_a$). The weight fraction of anatase increases from 60% to 91% as the film thickness increases from 260 to 790 nm. The mixed phase morphology of the undoped films is also observed on Ce-doped films deposited on ITO as long as the concentration of Ce remains below 1.2 at.%. No significant change is observed on the crystallite size of the anatase phase compared to that of undoped films. A further increase of the Ce concentration leads to an amorphization of the films. Our XRD studies show that the crystal structure and the morphology of the films are influenced by the chemical nature and the temperature of the substrate, and by the concentration of the doping material. The rutile-like structure of the ITO substrate is likely to be at the origin of the nucleation of the rutile phase observed during the initial growth stages. With increasing film thickness, the anatase phase eventually predominates. The nucleation of the rutile phase is limited to the film/ITO interface as it requires a high temperature to form.$^{10)}$

On highly Ce-doped films (> 1.2 at.%), the mismatch between the ionic radii of Ti^{4+} (0.68 Å) and of Ce^{4+} (1.01 Å) or Ce^{3+} (1.13 Å) is suspected to be at the origin of the amorphization of the films. The amorphous morphology of these films persists in spite of high-temperature thermal treatments (RTA up to 873 K). At intermediate Ce-doping concentrations (0–1.0 at.%), amorphous films can be also obtained by film deposition at 373 K. Upon thermal treatment up to 673 K (by LTA or RTA) such films transform into pure anatase. The film structure is similar to that of films prepared with low or no Ce doping at 540 K on glass substrates. We conclude therefore that both LTA and RTA, performed on amorphous samples deposited at low temperature, are efficient and well-controlled processes to obtain a homogeneous anatase film on ITO substrates.

3.2 DC electrical properties

The dc electrical conductivity of TiO_2:Ce (cf. Table I for preparation conditions) was measured between 300 and 600 K. Its dependence on the Ce concentration is reported in Fig. 2. Ce doping decreases the TiO_2 conductivity so that samples doped with 2.1 at.% of Ce have a conductivity 300 times lower than undoped samples. The experimentally determined activation energy of the conductivity decreases slightly from 0.65 eV for light doping to 0.60 eV for heavy doping. If Ce were acting as a simple electron trap or as a simple acceptor, the activation energy would actually increase with increasing compensation, which is contrary to observation. Since the Ce ion is much larger than the Ti^{4+} ion (1.01 versus 0.68) it is quite unlikely that Ce can act as a substitutional impurity. For steric reasons, however, the formation of a complex defect comprising a Ce atom and an oxygen vacancy in close proximity should be energetically more favorable. Kofstad has proposed several models[11] of defect equilibria in which the concentration of an intrinsic defect (here, the oxygen vacancy) becomes equal to the concentration of the extrinsic impurity. In fact, the following model is able to explain the dependence of conductivity on both temperature and Ce concentration: It has been shown[12] that undoped TiO_2 films contain about $10^{19}\,cm^{-3}$ oxygen vacancies which act as double donor.[13] All the electrons of the shallow donor level are trapped by an unidentified impurity level, and electrons must be promoted from the deep donor level to the conduction band to participate in the electronic transport. The present model proposes that each Ce atom introduced in TiO_2 creates on the one hand a trap level and on the other hand an additional oxygen vacancy. In other words, the doping of TiO_2 with Ce can be represented as the replacement of a $Ti^{4+}O^{2-}O^{2-}$ unit by a $Ce^{3+}O^{2-}X^-$ unit, in which the O vacancy has lost one electron to the Ce trap level. The corresponding model for the carrier concentration can be specified as follows: a) the conduction electron concentration is given by $n = N_C \exp(-(E_C - E_F)/kT)$, where N_C is the effective density of states in the conduction band (in our case, $N_C =\sim 10^{20}\,cm^{-3}$ is a reasonable value), E_C the energy of the bottom of the conduction band, E_F the Fermi level, k the Boltzmann constant, and T the temperature, b) in the unintentionally doped material the concentration of O vacancies is N_{X^o} and in Ce-doped material it is increased by an amount x equal to the Ce concentration. The concentration of singly-ionized vacancies is

$$N_{X^+} = \frac{(N_{X^o} + x)}{(1 + 2\exp(-(E_{X_1} - E_F)/kT))}$$

and the concentration of doubly-ionized vacancies is

$$N_{X^{++}} = \frac{N_{X^+}}{(1 + 2\exp(-(E_{X_2} - E_F)/kT))}$$

The undoped material also contains deep trap levels in concentration $N_{X^o} < N_{T_1} < 2N_{X^o}$ with binding energy E_{T_1}, and the Ce-doped material contains deep traps in concentration $x < N_{T_2} < 2x$ with binding energy E_{T_2}. The concentrations of occupied traps are given by

$$N_{T^-_{1,2}} = \frac{N_{T_{1,2}}}{(1 + 2\exp(-(E_F - E_{T_{1,2}})/kT))}$$

where the binding energies $E_{T_{1,2}}$ are larger than E_{X_2}. The Fermi energy is determined by the neutrality requirement

$$n + N_{T^-_1} + N_{T^-_2} = N_{X^+} + N_{X^{++}}$$

Fitting the experimental results shows that a) the first ionization energy of the is less than 200 meV so that the concentration of neutral vacancies is negligible, and b) the second ionization of the vacancy is 650 meV and it is approximately equal to the activation energy of the carrier concentration. Finally, if one assumes that the electron mobility μ = about 0.3 V s/cm^2,[12] is not a strong function of temperature, compared to the electron concentration dependence, one obtains the conductivity $\sigma = ne\mu$ reported as solid lines in Fig. 2.

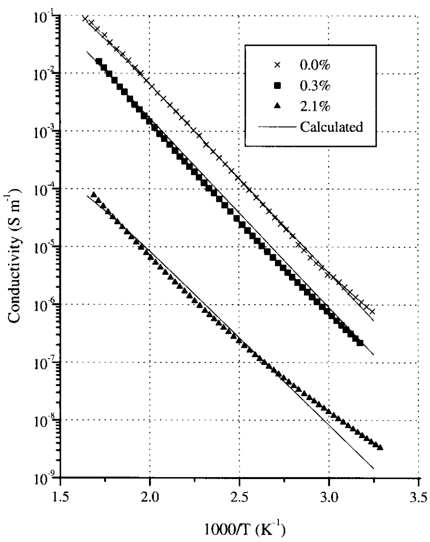

Fig. 2. Influence of Ce doping on the dc conductivity of TiO_2 films.

It is worth noting that the same model explains the properties of the undoped or, more accurately, unintentionally doped films: that is, such films contain an unidentified impurity M, and for each M atom, a $Ti^{4+}O^{2-}O^{2-}$ unit is replaced by an $M^{3+}O^{2-}X^-$ unit.

The conductivity drop between polycrystalline films (Ce concentration < 1.2 at.%) and amorphous films indicates that the mobility is 3000 times lower in amorphous samples than in polycrystalline material. As expected, electronic conduction in the amorphous films appears to be a hopping process rather than a band process. The progressive decrease of the activation energy at low temperature is another telltale sign of hopping conduction.

3.3 Dielectric properties

The dielectric properties of Ce-doped films have been investigated in the frequency range extending from 10^2 to 10^6 Hz. The effects of the Ce concentration on the dielectric properties of an anatase (0.4 at.%) and an amorphous (2.1 at.%) films are shown in Fig. 3. Ce doping shifts the ac conductivity towards lower values while the maximum value of the ac permittivity and the frequency dispersion of heavy doped films are much weaker than that of lightly doped films. The film with the largest Ce doping (2.1 at.%) exhibits a frequency independent permittivity. The temperature dependence of the ac permittivity and ac conductivity of heavily Ce-doped films have been investigated over the temperature range from 300 to 573 K. The results of the measurements performed on a 230-nm-thick, 2.1 at.%, Ce-doped amorphous film are shown in Fig. 4. The fre-

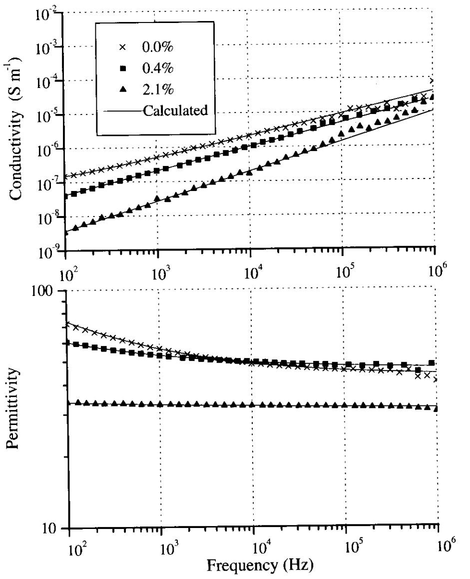

Fig. 3. Influence of Ce doping on the dielectric properties of TiO_2 films. (a) conductivity vs. frequency, (b) permittivity vs. Frequency.

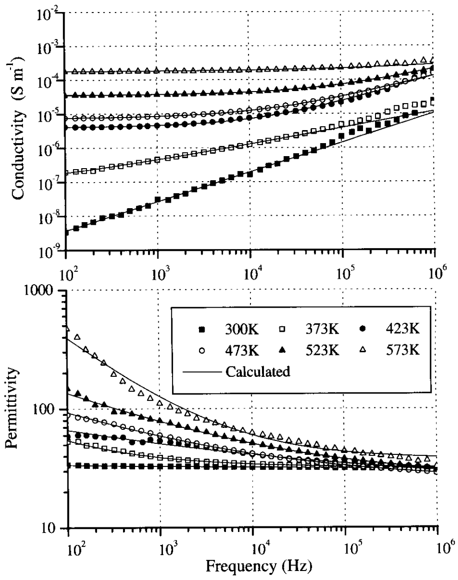

Fig. 4. Temperature dependence of the dielectric properties of 2.1 at.% Ce-doped TiO_2 films. (a) conductivity vs. frequency, (b) permittivity vs. frequency.

quency dependence of the permittivity and conductivity of all the films discussed here obey a simple power law, viz. $\sigma(\omega) = \sigma_0 + \sigma_1\omega^p$ and $\varepsilon(\omega) = \varepsilon_\infty + \varepsilon_1\omega^{(p-1)}$, with $0 < p < 1$ and $\varepsilon_0\varepsilon_1 = \sigma_1 \tan(p\pi/2)$, where ε_0 is the permittivity of vacuum and σ_0 the dc conductivity. The solid curves in Figs. 3 and 4 represent the values obtained with this power law. This behavior is commonly observed on a wide range of insulating or poorly conducting materials.[14–18] In the particular case of $4.5TiO_{2-x}\cdot 2P_2O_5$ glass,[14] it has been shown to ensue from hopping conduction. When the Ce concentration increases, the exponent p increases from 0.65 (undoped) to 0.86 (2.1 at.% Ce). In several hopping theories,[14] the increase of p at a given temperature indicates that the typical distance between hopping sites decreases. In our case, it indicates that distance between hopping sites varies like the distance between Ce impurities. The decrease of p with temperature (strong frequency dispersion at high temperature) is consistent with Springett's hopping model.[14] At high temperature, the electronic transport is dominated by the conduction band conductivity that results in an almost frequency-independent resistivity. As a result, σ_1 becomes much smaller than σ_0.

3.4 *Insulator breakdown characteristics*

Figure 5 shows the current density as a function of the electric field for TiO_2 thin films having different Ce concentrations (cf. Table I for preparation conditions). In doped films the current at low fields is more than two orders of magnitude lower than in the undoped films. This confirms the higher resistivity of the doped material. The breakdown threshold is identified as the abrupt bending off (knee) of the curve at a field of about 3 x 10^6 V/m. Beyond the knee an avalanche-like current increase results in a destructive breakdown of the insulator. In

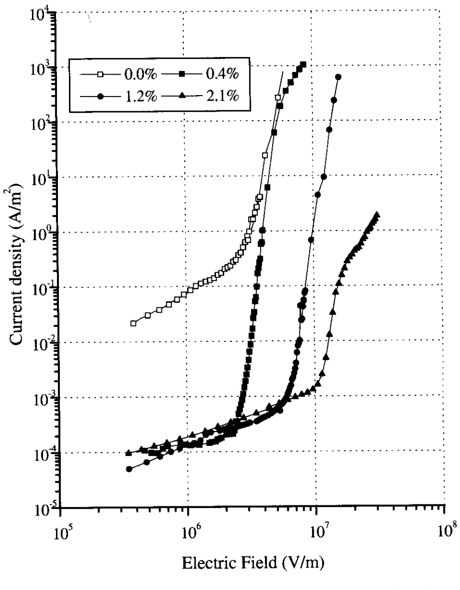

Fig. 5. Ce-doped TiO_2 thin films. Electrical current density vs. electrical field for several levels of doping.

films containing 0.4 at.% Ce, the current at low fields is lower than in the undoped films, but the breakdown knee is not modified. A further increase in Ce concentration induces a shift of the breakdown knee towards higher electric fields: it is located at 7 × 10^6 V/m for films containing 1.2 of Ce and above 10^7 V/m for the most heavily doped sample (2.1 at.%). The breakdown field increase is due to both the introduction of cerium traps and to the transformation from crystalline anatase to an amorphous structure. The breakdown mode depends on the metal used for electrical contacts. With Al contacts, a propagating breakdown occurs, while with Au contacts, breakdown is self healing.

3.5 ELD performance

The above results show that TiO_2:Ce is an interesting insulating material. Now we present the improvement in performance of ELD using amorphous TiO_2:Ce instead of Y_2O_3 or $BaTa_2O_6$ as insulating layers. We have not prepared ELDs with undoped TiO_2 because of its poor electrical properties for this purpose (low resistivity and low breakdown voltage). Typical characteristic curves, i.e. brightness B and transferred charge Q_t versus applied peak voltage V_{peak} are presented in Figs. 6(a) and 6(b). For standard devices of type A (cf. Table II), the threshold voltage is of the order of 140 V (cf. Table III). The brightness increases steeply at first and then reaches saturation at 240 cd/m² above 200 V for a transferred charge Q_t of 4 μC/cm². For asymmetrical devices of type B, the small slope of the brightness curve indicates an important charge leakage in these devices. For devices without charge leakage, Lissajou curves of the stored charge versus applied voltage (as in Fig. 7) should display as a straight line below the threshold voltage (ideal capacitance) and as parallelograms above the threshold voltage.[5] In the case of the B devices, hysteresis appears already at low bias. This indicates that type B devices do not behave as an ideal capacitance at low voltage, and that leakage currents are present. In spite of this limitation, at voltages less than 200 V the devices reach a higher brightness level (460 cd/m²) than type A devices. In comparison, for symmetrical devices of type C and D which have TiO_2:Ce insulators on both sides, the threshold voltage is as low as 80 V. The brightness increases with a steeper slope than in A or B devices. The maximum brightness level at 132 V is 330 cd/m² and 455 cd/m² for C and D devices respectively. In both groups, high brightness levels require significantly lower operating voltages than type A and B devices. Devices of type D, which were subject to an RTA process, show a steeper rise in their Q_t–V characteristics than devices of type C. The transferred charge rises with a slope of 0.330 μC/cm². It results in a high value (320 cd/m²) of the L_{30} brightness, where L_{30} is defined as the brightness at 30 V above the threshold voltage. A brightness level of 455 cd/m² was measured on these devices without reaching saturation. The devices, however, broke down at higher voltages. Charge densities of the order of 5 to 8 μC/cm² are transferred across the phosphor during device operation. Samples of type C and D give a higher brightness due to a larger transferred charge, the total efficiency being slightly higher for samples of type C and D compared with type A samples.

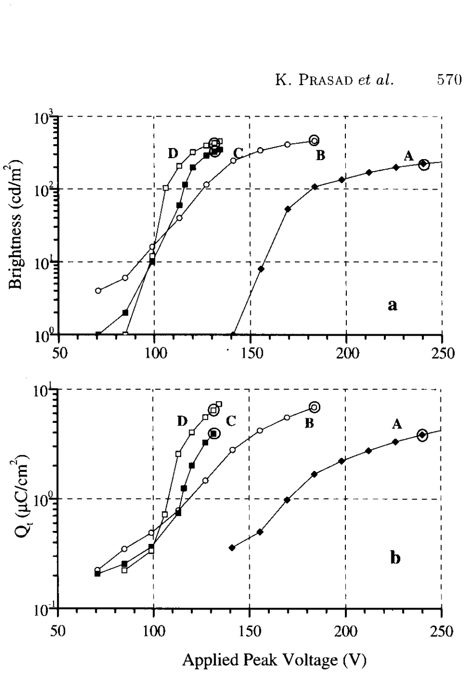

Fig. 6. Electroluminescent devices (MISIM structure). (a) brightness vs. applied peak voltage, (b) transferred charge Q_t vs. applied peak voltage for A, B, C and D devices (cf. Table II).

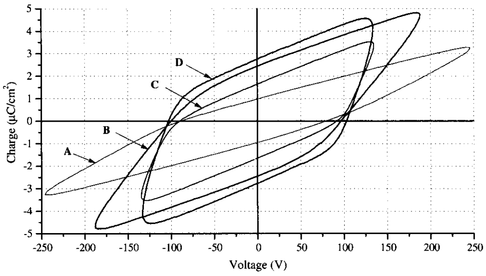

Fig. 7. Electroluminescent devices (MISIM structure). Charge vs. applied voltage (above the threshold voltage) for A, B, C and D devices (cf. Table II).

Figure 7 shows stored charge versus applied voltage at high luminescence levels for the four device groups. The measurement points are marked by circles in Figs. 6(a) and 6(b). The slope of the steepest parallelogram side corresponds to the insulator capacitance.[5] The values of the insulator layer permittivity ε were estimated from the slope at high field and from the insulator thickness. The resulting values of ε are 16, 32, 57, and 61 for devices of type A, B, C and D, respectively. Due to the lower dielectric constant of $BaTa_2O_6$ ($\varepsilon = 22$) the "apparent" permittivity of the insulators is lower in the asymmetrical devices of type B than in devices of type C and D. Compared to C devices, the slope at high field is higher for devices of type D which were subjected to an RTA process. The D insulators, although similar to those in devices of type C, are estimated to have a higher value of the permittivity ($\varepsilon = 61$). It is likely that this improvement is due to the RTA process carried out on devices of type D. The threshold voltage across the phosphor layer is given by the intercept of the voltage axis and the high voltage part of the parallelogram.$^{5)}$ In D devices it occurs at 105 V and corresponds to an electric field of 2×10^8 V/m across the phosphor layer, which is in agreement with values reported for ZnS:Mn phosphor. The breakdown voltage for type D devices was of the order of 134 V. Considering that the field across the phosphor layer remains constant above the threshold voltage, the electric field across the insulator layer is 6.4×10^7 V/m. This value is higher than the measured value 2×10^7 V/m for thin films doped with 2.1 at.% of Ce (Fig. 5). This difference is due to the higher Ce concentration of 2.3 at.% and to the properties of the interface between TiO$_2$:Ce and ZnS:Mn. Such an electric breakdown field gives us a figure of merit of the order of 3.5 μC/cm^2.

4. Conclusion

The insulating properties of TiO$_2$ thin films have been stabilized and improved by cerium doping. The film structure is anatase at low doping (< 1.2 at.%) and becomes amorphous for higher Ce concentration. The dc conductivity measurements show that cerium incorporation into TiO$_2$ has two effects. Due to the large Ce ionic radius, new oxygen vacancies are created into the oxide and electron traps are simultaneously introduced. The combination of these two effects results in a decrease of the TiO$_2$ conductivity with Ce doping. The ac conductivity and ac permittivity can be explained by including a hopping contribution in the electron conduction process. At high Ce concentration, the permittivity is frequency independent. A Ce concentration increase also results in an increase of the electrical breakdown field.

The implementation of such thin films as insulators in the MISIM structure of an ACTFELD shows a significant drop in the operating threshold voltage, an increase in the slope of brightness-voltage characteristics and a higher efficiency of the transferred charge. Annealed amorphous Ce-doped TiO$_2$ insulator layers exhibit an electric breakdown field of 6.4×10^7 V/m, a dielectric constant ε of 61, and a figure of merit of 3.5 μC/cm^2. Thus Ce-doped TiO$_2$ films meet the requirements for a high permittivity insulator layer and are able to form a suitable interface with ZnS in an ACTFELD. Further improvements are still required to drive the devices into saturation. RTA processing may provide an interesting alternative to anneal out defects and to produce symmetrical, improved interfaces with the phosphor.

Acknowledgements

The authors would like to thank Mrs. M. Gouy, S. Gamper, H. Jotterand and A. Nappey for their valuable assistance and technical support. This work was supported by the Priority Program of the Board of the Swiss Federal Institutes of Technology: Optical Science, Applications and Technology and by the Swiss National Science Foundation.

1) T. Inoguchi and S. Mito: *Electroluminescence*, ed. J. I. Pankove (Springer, New York, 1982) Topics in Applied Physics, Vol. 17, p. 197.
2) W. E. Howard: IEEE Trans. Electron Devices **24** (1977) 903.
3) S. K. Tiku and G. C. Smith: IEEE Trans. Electron Devices **31** (1984) 105.
4) Y. Fujita, J. Kuwata, M. Nishikawa, T. Tohda, T. Matsuoka, A. Abe and T. Nitta: Japan Display (1983) 76.
5) Y. Ono: *Electroluminescent Display*, ed. H. L. Ong (World Scientific, Singapore, 1995) Series on Information Displays.
6) J. Antson: Dig. Society for Information Display Int. Symp. (1982) p. 124.
7) J. Benoit, P. Benalloul, A. Geoffroy, N. Balbo, C. Barthou, J. P. Denis and B. Blanzat: Physica Status Solidi A **83** (1984) 709.
8) H. Xian, P. Benalloul, C. Barthou and B. Benoit: Jpn. J. Appl. Phys. **33** (1994) 5801.
9) R. A. Spurr and H. Myers: Anal. Chem. **29** (1957) 760.
10) D. Wikaskana, A. Kobayashi and A. Kinbara: J. Vac. Sci. & Technol. A **10** (1992) 1479.
11) P. Kofstad: *Nonstoichiometry, Diffusion, and Electrical Conductivity in Binary Metal Oxides* (R. E. Krieger, Malabar, 1983).
12) H. Tang, K. Prasad, R. Sanjinès, P.E. Schmid and F. Lévy: J. Appl. Phys. **75** (1993) 2042.
13) K. Mizushima, M. Tanaka, A. Asai, S. Ilda and J. B. Goodenough: J. Phys. Chem. Solids **40** (1979) 1129.
14) B. E. Springett: J. Non-Cryst. Solids **15** (1974) 179.
15) A. K. Jonscher: Nature **267** (1977) 673.
16) A. K. Jonscher: J. Non-Cryst. Solids **8–10** (1972) 293.
17) F. Argall and. A. K. Jonscher: Thin Solid Films **2** (1968) 185.
18) D. L. Sidebottom, P. F. Green and R. K. Brow: Phys. Rev. B **51** (1995) 2770.

TiO_2:Ce/CeO_2 HIGH PERFORMANCE INSULATORS FOR THIN FILM ELECTROLUMINESCENT DEVICES

A. R. Bally*, K. Prasad*, R. Sanjinés*, P. E. Schmid*, F. Lévy*, J. Benoit**, C. Barthou**, P. Benalloul**

*Institute of Applied Physics, EPFL, Lausanne, Switzerland, schmid@ipasg.epfl.ch
**Laboratoire d'Acoustique et Optique de la Matière Condensée, Université P. et M. Curie, Paris, France, cbp@aomc.jussieu.fr

ABSTRACT

The electrical properties of titanium dioxide thin films have been stabilised by cerium doping. These films have a high permittivity between 35 to 45 and withstand 650°C. Multilayer TiO_2:Ce/CeO_2 insulators have been fabricated. The breakdown voltage is increased by a factor 10 with a modest decrease in the permittivity (30 - 35 instead of 35 - 45).

Electroluminescent devices (ELDs) with a classical ZnS:Mn phosphor have been prepared using TiO_2:Ce as the first insulator and a TiO_2:Ce/CeO_2 multilayer as the second insulator. Compared with a standard ELD based on Y_2O_3 insulators, devices with the new insulators show a significant decrease of the threshold voltage along with a notable increase of the brightness. An important increase is also achieved in the total device efficiency which is maintained over a large range of brightness and transferred charge. Consequences of rapid thermal annealing and conventional thermal treatments on device performance have also been investigated.

INTRODUCTION

Thin film electroluminescent devices (TFELD) provide an attractive alternative for solid-state flat panel displays[1]. Dielectric materials play a decisive role in the performance of these Metal-Insulator-Semiconductor-Insulator-Metal (MISIM) structures[1,2,3,4]. Under actual operating conditions, very high electrical fields of the order of 100-200 MV/m are applied to the phosphor layer. The role of the dielectric is to prevent the device breakdown under these high fields and to keep charges suitably trapped in interface states so that they do not leak out into the phosphor at lower fields. Most important of all, a dielectric with a high permittivity lowers the operation threshold voltage as it increases the electric field in the emitting layer for a same applied voltage.

A number of studies have reported attempts at finding suitable dielectrics for TFELD applications having the highest figure of merit, which is defined as the product of dielectric constant and breakdown electric field $\varepsilon_o\ \varepsilon\ E_{bd}$[5]. This figure of merit, which indicates the maximum trapped charge density for an insulator material, is of the order of 4-6 $\mu C/cm^2$ in classical TFELDs[6]. Because of its high permittivity, TiO_2 is a potential candidate provided its electrical properties can be controlled. Undoped TiO_2 is always slightly substoichiometric and oxygen vacancies modify its dielectric properties. A figure of merit of only 1 $\mu C/cm^2$ has been reported corresponding to a high ε (60) but a very low E_{bd} (20 MV/m)[6].

The electrical properties of titanium dioxide have been stabilised by cerium doping. Ce doping leads to an increase of the resistivity, a reduced variation of the permittivity with frequency and a higher breakdown voltage. After a description of cerium doping effects on TiO_2 thin films, a comparison between a standard TFELD (with Y_2O_3 insulators and ZnS: Mn

Mat. Res. Soc. Symp. Vol. 424 © 1997 Materials Research Society

phosphor) and a device with TiO_2:Ce/CeO_2 insulators will show the improvement due to the new insulators.

EXPERIMENTAL DETAILS

Two types of structures were prepared in the present study. For electrical measurements, thin films of undoped TiO_2, Ce-doped TiO_2 and CeO_2 were deposited on ITO-coated glass by reactive RF sputtering. 2 mm^2 gold dots were evaporated as top contacts. For TFELD investigations, MISIM structures were fabricated on ITO-coated glass. The standard Y_2O_3 insulators were deposited by e-gun evaporation and the Mn-doped ZnS phosphor layers were prepared using co-evaporation of ZnS by e-gun and MnS by thermal evaporation. Aluminium or gold dots with an area of 2 mm^2 were evaporated as top metal contacts.

Devices were subjected to a long thermal annealing (LTA) for 2 hours in vacuum at 650°C after the deposition of ZnS:Mn. Such post-deposition heat treatment of ZnS:Mn is widely used to improve the electroluminescent brightness by increasing both excitation and radiative efficiencies[6]. The device structure is given in Table I.

Table I: Electroluminescent Device configurations

Device	Transparent electrode	Bottom insulator	Phosphor	Top Insulator	Reflecting electrode
A	ITO	Y_2O_3 330 nm	ZnS:Mn 520 nm	Y2O3 360 nm	Al
B	ITO	TiO2:Ce 270 nm	ZnS:Mn 520 nm	TiO2:Ce 200 nm CeO2 200 nm	Au

An impedance analyser (HP 4192A) was used to perform ac electrical measurements on the MIM structures. The frequency was swept in the range from 100 Hz to 1 MHz. An amplitude of 100 mV was selected for the oscillation level of the signal. For luminescence measurements, a sinusoidal 1 kHz voltage source was used as the excitation signal. The brightness was measured using a Minolta Photometer. The threshold voltage is defined as the voltage required (or extrapolated) for a brightness of 1 cd/m^2. The transferred charge as a function of applied voltage was determined by measuring the stored charge in the sense capacitor of a Sawyer-Tower circuit[7].

It should be noted that in this work the phosphor was not optimised and therefore the total brightness level is less than what is generally reported[6]. Valid comparison can nevertheless be obtained since the phosphor is the same in both devices.

RESULTS

The dielectric properties of the doped and undoped films were investigated in the frequency range from 10^2 to 10^6 Hz. The permittivity and resistivity were deduced from the ac impedance measurements while taking into account the series resistance due to the ITO electrode. In the case of undoped films, the results reveal large differences in the dielectric constant ε and the ac resistivity ρ depending on the preparation and thermal treatments. At room temperature, the films exhibit values of $\varepsilon = 50 - 400$ and $\rho = 10^7$-10^9 Ωm at 10^2 Hz.

The effects of the cerium doping on the dielectric properties of the TiO_2 are shown in Fig. 1. Cerium doping shifts the resistivity towards higher values while the high permittivity values and the frequency dispersion is much weaker than in undoped films. The dielectric constant undergoes a sharp drop as the Ce concentration is increased from 0.4 to 0.7 at.%. Films with the largest Ce doping (2.1 at.%) exhibit a frequency independent value of the permittivity.

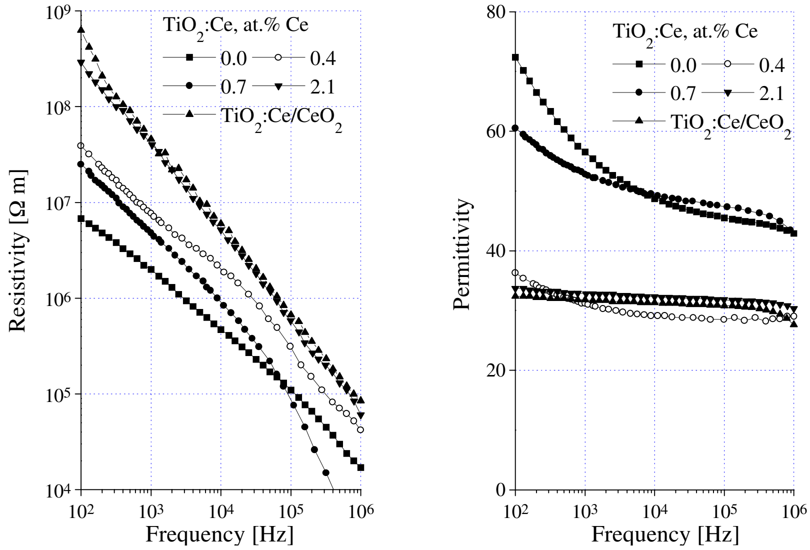

Figure 1: Dielectric properties of Ce-doped TiO_2 thin films.

Fig. 2 shows the current density J as a function of the electric field E for TiO_2 thin films having different concentrations of Ce and different thicknesses. In undoped films the current at low fields is more than two orders of magnitude higher than in the doped films. This confirms the higher resistivity of the doped material. The breakdown threshold is identified as the abrupt bending off (knee) of the J-E curve at a field of about 3 MV/m. Beyond the knee the avalanche-like current increase results in a destructive breakdown of the insulator.

In films which contains 0.4 at.% Ce, the current at low fields is lower than in the undoped films indicating an increase of its resistivity. However, the breakdown knee is not modified. In the remaining curves one observes a shift of the breakdown knee towards higher electric fields: it is situated at 7 MV/m for the films containing 1.2 and above 10 MV/m for the most highly doped sample (2.1 at.%). Thus the breakdown strength of Ce-doped TiO_2 increases with increasing Ce concentration.

CeO_2 is reported to have a higher breakdown voltage then TiO_2. Its value varies between 200 and 2000 MV/m in thin films[8]. The formation of multilayer insulator with TiO_2:Ce and CeO_2 shows a breakdown voltage of 100 MV/m, which is 30 times higher than the breakdown voltage of undoped TiO_2 thin films. The resistivity and permittivity curves represented in Fig. 1 show that the dielectric properties are quite close to than those of TiO_2:Ce values because CeO_2 thin films also have a high permittivity of about 26[8].

It is worth noting that preliminary oxide breakdown measurements indicate that Au contacts are self healing and more stable at higher voltage than Al contacts. Unlike Al contacts lead to propagative breakdown.

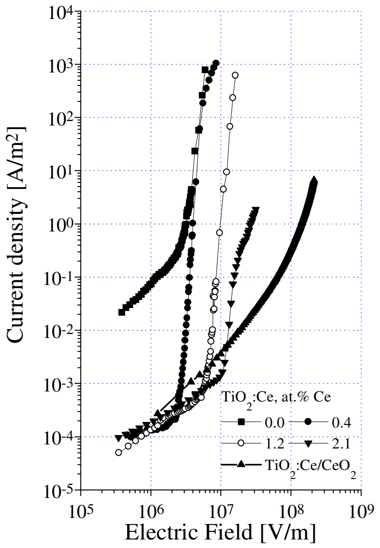

Figure 2: Electrical current density versus electrical field for different levels of doping of TiO_2:Ce.

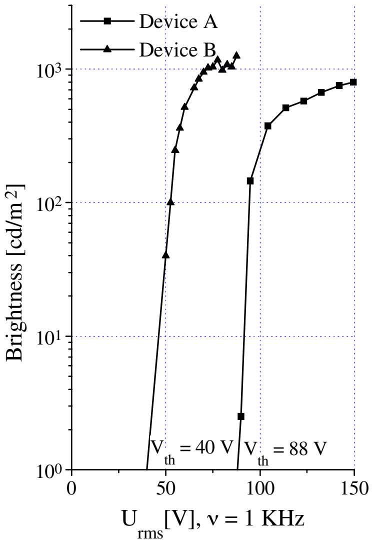

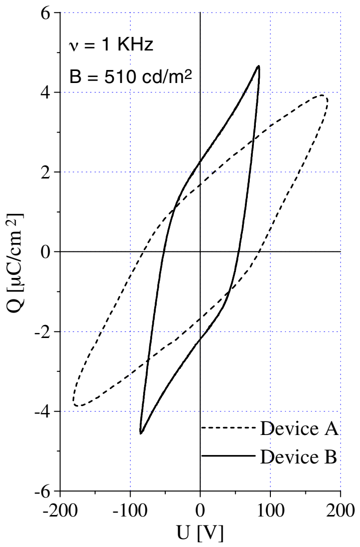

Figure 3: Brightness versus applied voltage for two different devices.

Figure 4: Charge versus applied voltage for two different devices.

The brightness dependence on the applied voltage for two different devices with the same phosphor is presented in Fig. 3. The high permittivity of the TiO_2:Ce/CeO_2 insulator compared to the Y_2O_3 insulator results in a substantial decrease of the threshold voltage for device B. In this case, threshold voltage goes down from 88 V_{rms} to 40 V_{rms}. The highest brightness saturation of the device B and the steep increase of the brightness show that the interface between TiO_2:Ce and ZnS:Mn does not leak carriers, as seen in the well-defined curve of Fig. 4. The incorporation of a CeO_2 layer in the insulators protects the device against breakdown, so that it can be driven to brightness saturation.

The Lissajou curves for the both devices at a same brightness level are shown in Fig. 4. The steeper slopes of the device B curve show the higher permittivity of our new insulators. A permittivity value of 11.8 is found for the Y_2O_3 insulator and 42.7 for the TiO_2:Ce/CeO_2 insulator. The power dissipated in the device is proportional to the area under the Lissajou curve. At the same brightness level, device B shows a better efficiency than device A.

CONCLUSIONS

The results presented in this paper show that TiO_2:Ce/CeO_2 insulators are suitable for thin film electroluminescent devices based on a ZnS:Mn phosphor. The improvements, when comparing with the standard Y_2O_3 insulator, are a decrease of the threshold voltage and an increase of both brightness and efficiency.

ACKNOWLEDGMENTS

The authors would like to thank M. Gouy, S. Gamper, H. Jotterand and A. Nappey for their valuable assistance and technical support. This work was supported by the Priority Program of the Board of the Swiss Federal Institutes of Technology: Optical Science, Applications and Technology and by the Swiss National Science Foundation.

REFERENCES

1. T. Inoguchi, and S. Mito, Electroluminescence, Topics in Applied Physics 17, eds. J. I. Pankove (Springer, New York, 1982), p. 197.
2. W. E. Howard, IEEE Trans. Electron Devices ED-24, 903 (1977).
3. S. K. Tiku and G. C. Smith, IEEE Trans. Electron Devices ED-31, 105 (1984).
4. C. N. King, Society for Information Display (1985), Seminar Lecture Notes 4.1.
5. Y. Fujita, J. Kuwata, M. Nishikawa, T. Tohda, T. Matsuoka, A. Abe and T. Nitta, Japan Display, 76 (1983).
6. Y. Ono, Electroluminescent Display, Series on information displays (World scientific Publication Co., London, 1995).
7. H. Xian, P. Benalloul, C. Barthou and B. Benoit: Jpn. J. Appl. Phys. 33 (1994) 5801.
8. H. Bergmann, Gmelin Handbuch der Anorganische Chemie, Seltenerdelement Teil C1 (Springer-Verlag, New York, 1974), p. 244.

Appendix B

Paper on iron doped TiO_2

J. Phys. D: Appl. Phys. **31** (1998) 1149–1154. Printed in the UK

PII: S0022-3727(98)89101-8

Structural and electrical properties of Fe-doped TiO_2 thin films

A R Bally[†][‡], **E N Korobeinikova**[§], **P E Schmid**[†], **F Lévy**[†] **and F Bussy**[‖]

[†] Institut de Physique Appliquée, Ecole Polytechnique Fédérale de Lausanne, CH-1015 Lausanne, Switzerland
[§] Institute of Crystallography, Academicheskaya, 248033-Kaluga, Russia
[‖] Institut de Minéralogie, Université de Lausanne, CH-1015 Lausanne, Switzerland

Received 11 November 1997

Abstract. The present study discusses the effect of iron doping in TiO_2 thin films deposited by rf sputtering. Iron doping induces a structural transformation from anatase to rutile and electrical measurements indicate that iron acts as an acceptor impurity. Thermoelectric power measurement shows a transition between n-type and p-type electrical conduction for an iron concentration around 0.13 at.%. The highest p-type conductivity at room temperature achieved by iron doping was 10^{-6} S m^{-1}.

1. Introduction

Titanium dioxide is used in a wide range of applications as gas sensors [1], antireflective coatings [2], thin film capacitors [3], etc. The electrical and optical properties of TiO_2 depend on the concentrations of both intrinsic defects (mostly oxygen vacancies) and extrinsic impurities. Many impurities have been put into TiO_2 to improve its properties depending on the application. Few studies about iron-doped TiO_2 have been reported in the literature, though iron is always present in titanium oxide as an intrinsic impurity. As titanium oxide thin films are often deposited from a metal titanium target, it is important to know the behaviour of iron impurities in titanium oxide. The present study shows the structural and electrical changes of TiO_2 thin films with iron doping in titanium oxide. The structure of the films can be controlled by several deposition parameters including gas pressure, substrate temperature and discharge current [4–6]. In order to highlight the effect of iron, the deposition parameters were not changed except for the amount of iron oxide used during the deposition. Iron doping induces a structural transformation from anatase at low Fe concentration to rutile for Fe concentrations larger than 0.32 at.%. Electrical and thermoelectric power measurements show that the electrical conduction changes from n-type conduction for undoped TiO_2 to p-type conduction for heavily doped TiO_2, and demonstrate that iron atoms behave as acceptor impurities. Even at high iron concentration, thin films remain transparent.

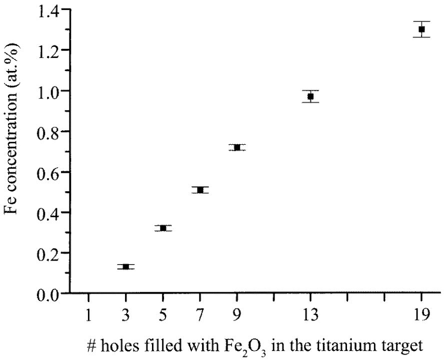

Figure 1. Iron concentrations versus number of holes filled in the titanium target during deposition.

2. Experimental details

Fe-doped TiO_2 thin films were deposited by reactive rf sputtering. The target was a metallic titanium disc (purity 99.5%, 60 mm diameter). Holes drilled into the titanium target (3 mm diameter) were filled with iron oxide powder (Fe_2O_3, purity 99.999%) to obtain Fe-doped TiO_2 thin films. Depositions took place under a pressure of 10^{-1} Pa of mixed Ar and O_2 atmosphere (33% of oxygen). Silicon, glass and indium tin oxide (ITO)-coated glass substrates were heated to 260 °C during the deposition. The rf power was 700 W, and the deposition rate was between 0.2 and 0.4 Å s^{-1}. Table 1 summarizes the properties of the

---

[‡] E-mail address: bally@ipasg.epfl.ch

0022-3727/98/101149+06$19.50

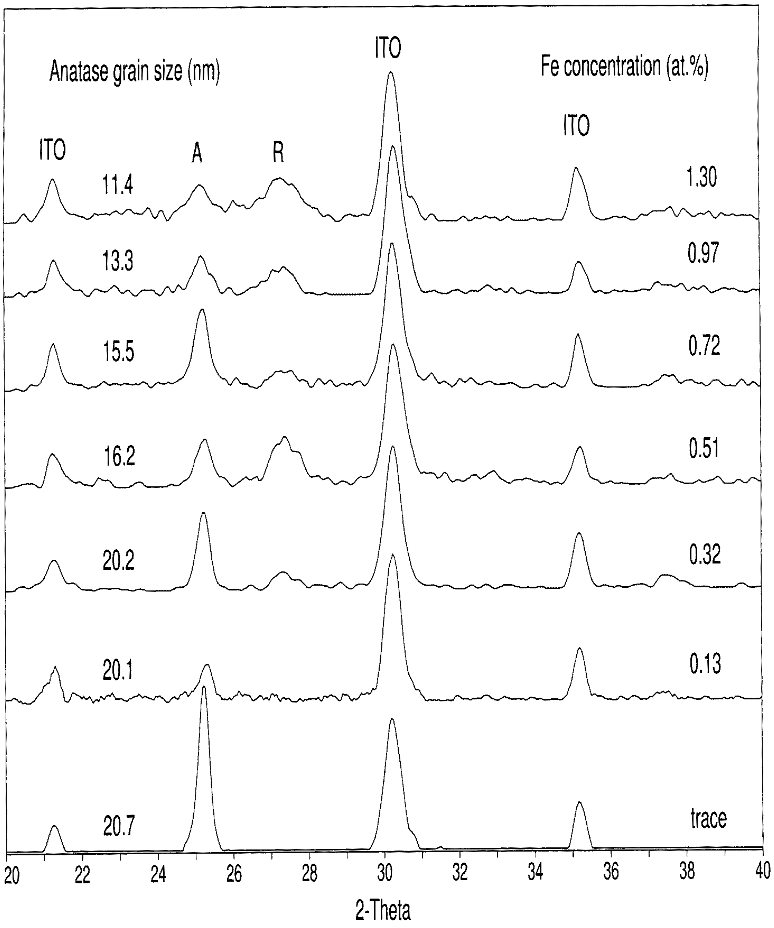

Figure 2. X-ray diffraction spectra of the Fe-doped TiO_2 thin films: A; (101) anatase peak; R, (110) rutile peak.

films. The iron concentration was measured by electron probe microanalysis (EPMA) using thin films deposited on a silicon substrate. Rutile TiO_2 and Fe_2O_3 were used as standard for the calibration. A small layer of carbon was deposited on the thin films to avoid electrical charging during the EPMA measurements. The thin film structure was investigated by x-ray diffractometry in a $\theta/2\theta$ angle configuration, and the morphology was investigated by atomic force microscopy (AFM) with a Topometrix Explorer AFM in non-contact mode. Gold contacts were evaporated on top of the thin films deposited on ITO-coated glass and the electrical measurements were performed in a transverse geometry (ITO/TiO_2:Fe/Au). dc electrical conductivity measurements were made with a Keithley 617 electrometer and ac electrical measurements with an HP4192a impedance analyser. In both cases, a voltage of 0.1 V was applied for the measurements. To determine the sign of the charge carriers, the thermoelectric power was measured on thin films deposited on glass substrates. Due to the high resistance of TiO_2:Fe thin films, the thermoelectric power was measured at 350 °C.

Table 1. Thin film properties. E_a denotes the conductivity activation energy at 333 K.

Name	Thickness (nm)	No of holes	Fe concentration (at.%)	E_a (eV)
A	300	0	0	0.65
B	290	1	Trace	0.51
C	240	3	0.13	0.59
D	290	5	0.32	0.63
E	190	7	0.51	0.65
F	200	9	0.72	0.56
G	240	13	0.97	0.54
H	350	19	1.30	0.51

3. Results and discussion

3.1. Iron concentration

The iron concentration in the films was varied from 0.1 to 1.3 at.% by changing the number of holes filled with

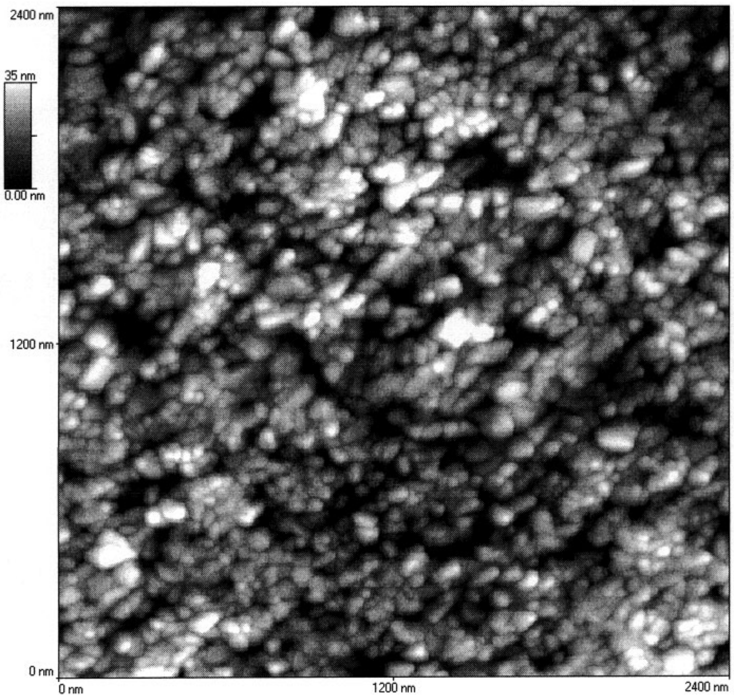

Figure 3. AFM image of TiO_2 : Fe sample D (0.32 at.% Fe).

iron oxide in the titanium (figure 1). The Fe concentration measurement errors were calculated using the same relative error as that of the raw data. A model was used to take into account the silicon substrate contribution. The concentration evolution is monotonic with the number of holes filled. The first part is linear, and when more than nine holes were filled the resulting iron concentration increased slowly. This can be explained by the fact that the holes are filled from the centre to the edge of the target and that the plasma is denser in the centre of the target. Therefore, the contribution of the outside holes during the deposition is less important.

3.2. Structural characterization and morphology

X-ray diffraction spectra (figure 2) reveal the influence of Fe doping on the structure of the TiO_2 thin film. The peaks related to the lower ITO electrode are labelled ITO. The ratio between the anatase and rutile phases can be calculated from the intensity I_A of the (101) anatase peak (labelled A) and the intensity I_R of the (110) rutile peak (labelled R) [7] with the following formula: $W_A = 1/(1 + 1.265\ I_R/I_A)$, where W_A is the weight percentage of the anatase phase. For Fe concentrations lower than 0.32 at.%, the rutile phase is not present in the films. When the Fe concentration increases, the weight percentage of the rutile phase becomes more and more important; it reaches 60% for the sample with 1.3 at.% Fe. The increase of the rutile phase weight percentage is accompanied by a decrease of the anatase grain size. Values calculated from the measured values of the full width at half the maximum (FWHM) of the most intense anatase peak (110) (shown in figure 2), indicate that the crystallite size decreases from 20 to 10 nm. No tendency to amorphization has been observed with Fe doping, whereas samples doped with more than 1.2 at.% Ce are consistently amorphous [3]. This can be explained by the fact that the Fe^{3+} ionic radius (0.64 Å) is close to the Ti^{4+} ionic radius (0.68 Å). The transformation from the anatase to the rutile structure with Fe doping is consistent with Bregani *et al*'s observations [8]; they noted that impurities like Cu, Mn, Cd, Fe, Co, Zn favour the transformation from anatase to rutile structure.

An AFM image from sample D (0.32 at.% Fe) is reported in figure 3. It shows that the thin films are composed of small crystallites. The crystallite diameter, around 35 nm, is larger than the size measured with XRD. As XRD is sensitive to the crystallite thickness perpendicular to the film and the AFM image shows the film surface, this means either that the grains are not spherical or that the grains are larger at the film surface than at the inner region. No preferential orientation for the crystallites was detected.

3.3. Optical properties

All films are transparent in the visible range. The absorption threshold for interband transitions appears at

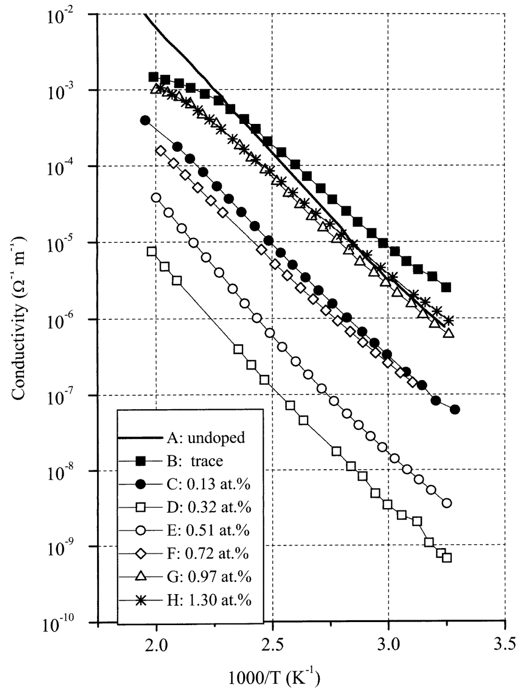

Figure 4. dc conductivity in TiO_2 thin films as a function of temperature, showing the influence of Fe doping (the lines are guides for the eyes). The inset indicates the iron concentration of the films.

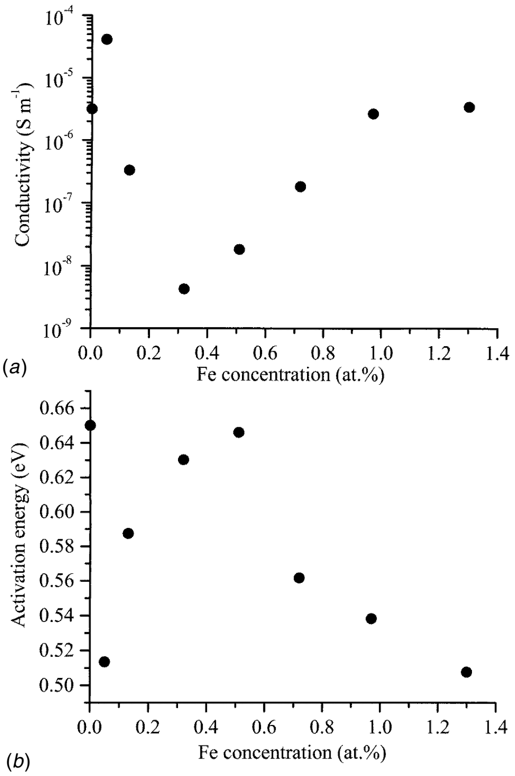

Figure 5. The dependence on the iron concentration of (*a*) the dc conductivity at 333 K and (*b*) the conductivity activation energy.

lower energy in highly Fe-doped samples. This change in the absorption spectrum in not actually related to the iron concentration, it simply reflects the change of structure from anatase to rutile induced by the iron atoms. The bandgap of the rutile (3.0 eV) is lower than the bandgap of the anatase (3.2 eV) [9], which explains the absorption threshold difference.

3.4. dc electrical properties

The dc electrical conductivity versus temperature was measured for various Fe concentrations (figure 4). For a fixed temperature, as the Fe concentration increases, the conductivity at first decreases, goes through a minimum for Fe concentrations between 0.13 and 0.32 at.% and then increases again (see figure 5(*a*)). This kind of behaviour, already reported in the literature for the case of Mn-doped TiO_2 [10], suggests a transition from n-type to p-type electrical conduction. Thermoelectric power measurements made at 350 °C show that samples A and B have n-type conductivity (negative thermoelectric power) and that other samples have p-type conductivity (positive thermoelectric power). The thermoelectric power is lower in sample C than in samples D to H where it is nearly constant. This means that both n-type and p-type conduction are present in sample C and that the transition between n-type and p-type TiO_2:Fe occurs for an Fe concentration near 0.13 at.%. It has been reported in the literature that Fe impurities act as acceptor impurities in TiO_2 [11], but Fe atoms do not behave as simple substitutional impurities replacing Ti atoms in the oxide lattice. It must be noted that sample B, the sample with the lowest Fe doping, shows an n-type conductivity higher than that of the undoped or, more accurately, not intentionally doped sample A at room temperature. This indicates that new oxygen vacancies are induced by the presence of iron atoms as proposed by Sayle *et al* [12]. The exponential dependence of the conductivity on inverse temperature defines an activation energy E_a. The activation energy E_a is lower in the case of low Fe doping (sample B, 0.51 eV) than in the case of the undoped sample A (0.65 eV), which is in agreement with Yu and Halley's calculations [13]. This confirms that the oxygen vacancy surroundings are different in each case. The ratio between the oxygen vacancy concentration and the iron concentration must be greater than 0.5 so as to account for the fact that all the acceptors created by the iron atoms are compensated by electrons given up by the oxygen vacancies (two electrons are available for each vacancy). As the iron

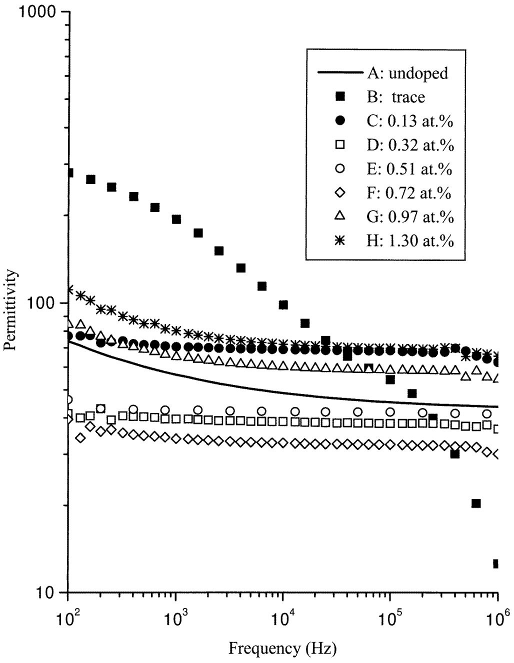

Figure 6. The permittivity of TiO_2 thin films as a function of frequency showing the influence of Fe doping.

concentration increases, the donor (vacancy) over acceptor (iron) ratio decreases and when it becomes lower than 0.5 the conductivity switches from n-type to p-type. The fact that the iron atoms create fewer oxygen vacancies at high concentration is consistent with the transformation from the anatase to the rutile structure when the iron concentration increases. Oxygen vacancies are necessary to stabilize the anatase structure [8] but iron can crystallize in a rutile-like structure in FeS_2 or $(Ta, Ti, Fe)O_2$ compounds [14] for example. Therefore, Fe atoms create fewer oxygen vacancies in the rutile structure then in the anatase structure. The evolution of the conductivity activation energy (figure 5(*b*)) shows that for p-type samples the acceptor level is located at 0.5 eV above the valence band.

3.5. Dielectric properties

The permittivity versus frequency was measured for different Fe concentrations (figure 6). At low doping, the permittivity exhibits a high value, which varies with frequency. Although the permittivity of the most heavily doped samples (>0.72 at.%) is lower than that of sample B (Fe trace), it also decreases with increasing frequency. The lowest permittivity values are observed in highly resistive thin films, for which the permittivity is frequency independent. Its values (around 40) are quite similar to the value reported for Ce-doped TiO_2 [3]. It is difficult to relate the permittivity dispersion to the film structure, because the grain size and the weight per cent of the anatase phase decrease in a consistent manner with the increase of the Fe concentration, whereas there is an Fe concentration for which the dispersion is minimum. The permittivity dispersion denotes an inhomogeneous conductivity [15]. This inhomogeneity is related to the different properties of the grains and grain boundaries, and/or to the different properties of the anatase and rutile phases.

4. Conclusion

We have shown that iron doping induces a transformation from anatase to rutile, without amorphization for doping lower than 1.3 at.%. Electrical measurements confirm that iron is an acceptor impurity. The transition from n-type to p-type electrical conduction occurs for an iron concentration around 0.13 at.%. The highest p-type conductivity reached at room temperature is 10^{-6} S m^{-1}. The dispersion of the permittivity with frequency indicates that the electrical conduction of the thin films is inhomogeneous. The influence of the iron atom depends on the crystal structure of the oxide. The introduction of iron generates more oxygen vacancies in anatase than in rutile. A large fraction of the acceptors created by the iron atoms are compensated by the oxygen vacancies created by the same iron atoms. The results presented in the paper point out that pure rutile, iron-doped TiO_2 has a higher p-type conductivity than mixed, anatase/rutile TiO_2 iron-doped thin films.

Acknowledgments

The authors would like to thank Christophe Ballif for the AFM measurements. This work was supported by the Swiss National Science Foundation. One author (ENK) acknowledges the Swiss Academy of Engineering Sciences for a Branco Weiss grant.

References

[1] Tang H, Prasad K, Sanjinés R and Lévy F 1995 *Sensors Actuators* B **26–27** 71
[2] Bange K, Ottermann C R, Anderson O, Jeschkowski U, Laube M and Feile R 1991 *Thin Solid Films* **197** 279
[3] Prasad K, Bally A R, Schmid P E, Lévy F, Benoit J, Barthou C and Bénalloul P 1997 *Japan. J. Appl. Phys.* **36** 5696
[4] Okimura K and Shibata A 1997 *Japan. J. Appl. Phys.* **36** 2849
[5] Kitao M, Oshima Y and Urabe K 1997 *Japan. J. Appl. Phys.* **36** 4423
[6] Wicaksana D, Kobayashi A and Kinbara A 1991 *J. Vac. Sci. Technol.* A **10** 1479
[7] Spurr R A and Myers H 1957 *Anal. Chem.* **29** 760
[8] Bregani F, Casale C, Depero L E, Natali-Sora I, Robba D, Sangaletti L and Toledo G P 1996 *Sensors Actuators* B **31** 25
[9] Tang H, Prasad K, Sanjinés R, Schmid P E and Lévy F 1994 *J. Appl. Phys.* **75** 2042

[10] Fujitsu S and Hamada T 1994 *J. Am. Ceram. Soc.* **77** 3281

[11] Radecka M, Rekas M and Zakrzewska K 1994 *Solid State Phenomena* **39–40** 113

[12] Sayle D C, Catlow C R A, Perrin M-A and Nortier P 1995 *J. Phys. Chem. Solids* **56** 799

[13] Yu N and Halley J W 1995 *Phys. Rev.* B **51** 4768

[14] Banfield J F, Bishoff B L and Anderson M A 1993 *Chem. Geol.* **110** 211

[15] Sayer M, Mansingh A, Arora A K and Lo A 1992 *Integ. Ferroelectrics* **1** 129

Appendix C

Paper on mechanical properties of TiO_x

ELSEVIER

Surface and Coatings Technology 108–109 (1998) 166–170

SURFACE & COATINGS TECHNOLOGY

Mechanical and electrical properties of fcc TiO_{1+x} thin films prepared by r.f. reactive sputtering

A.R. Bally*, P. Hones, R. Sanjinés, P.E. Schmid, F. Lévy

Institut de Physique Appliquée, Ecole Polytechnique Fédérale de Lausanne, CH-1015 Lausanne, Switzerland

---

Abstract

This paper reports on an investigation on fcc TiO_{1+x} thin films with $0<x<1$. The films were deposited by r.f. reactive sputtering and characterized by X-ray diffraction, electron probe microanalysis, X-ray photoelectron spectroscopy, atomic force microscopy, scanning tunneling microscopy, and electrical measurements. The films crystallized in the fcc phase with a lattice parameter $a=0.419$ nm, exhibit a gold like color, an electrical resistivity of about 400 μΩ cm at room temperature, and remarkable nanohardness values of about 23 GPa. The results of these experiments are discussed and compared to the archetypal fcc TiN coatings.

Keywords: Transition metal oxides; Reactive sputtering; TiO_x; Hardness

---

1. Introduction

Titanium nitride thin films are widely used as hard coatings [1]. An important problem is the hardness degradation due to oxidation at high temperature [2]. For bulk TiN a Vicker's hardness of 20.5 GPa is reported [3]. Titanium oxide TiO crystals with the same structure as TiN (fcc structure) has a hardness up to 19.6 GPa [4]. Thus, it is interesting to compare the hardness of titanium oxide thin films and titanium nitride thin films, and to follow the hardness evolution after oxidation. Two sets of titanium oxide thin films (TiO_{1+x} with $0<x<1$) have been prepared by r.f. sputtering using two different reactive gases, oxygen and water vapor. In this paper we report on the structure and hardness of TiO_{1+x} deposited with oxygen or water vapor as reactive gas and we compare the results with titanium nitride. To the best of our knowledge, this is the first systematic study of mechanical properties and annealing effects of TiO_{1+x} thin films.

2. Experimental

TiO_{1+x} thin films were prepared by reactive r.f. sputtering. The target material was metallic titanium (purity 99.5%). The depositions were performed at a total pressure of 10^{-1} Pa in mixed Ar and O_2 or Ar and water vapor atmosphere, respectively. The ratio between the inert gas (Ar) and reactive gas (O_2 or H_2O) was varied from 5 to 30% in order to obtain different oxygen concentrations in the films. Thin films deposited with oxygen as reactive gas are named type A TiO_{1+x} and thin films deposited with water vapor as reactive gas are named type B TiO_{1+x} throughout the paper. Silicon wafers, glass, and high speed steel (HSS) were used as substrates. The film thickness was about 1 μm. Thin films deposited with addition of water vapor did not adhere on glass and HSS substrates. For this reason 50 nm TiO_2 prepared by d.c. reactive sputtering [5], in the same chamber, was deposited as an adhesive layer on glass and HSS substrates. The oxygen concentration of films deposited on silicon was measured by electron probe microanalysis (EPMA) using the Ti Kα and the O Kα lines. A rutile TiO_2 crystal was used as a standard. Secondary ion mass spectrometry (SIMS) was applied to quantify the residual hydrogen content. The crystal structure, phase, and residual stress were investigated by X-ray diffraction (XRD) in a grazing angle configuration ($\theta=5°$). The morphology was investigated by atomic force microscopy (AFM) with a Topometrix Explorer AFM in a non-contact mode, and by scanning tunneling microscopy in ultra-high vacuum with an Omicron STM. Electrical measurements were performed in the four-point geometry on glass substrates. The nanohardness was determined by a commercial nanoindentation system (XP, Nano Instruments). A Berkovich-type pyramidal diamond tip indented the films to a maximum depth of 700 nm. Constant stiffness data measurements were obtained by oscillating the tip during indentation at a frequency of

---

*Corresponding author. Tel.: +41-21-6934439; fax: +41-21-6934666; e-mail: alain.bally@epfl.ch

0257-8972/98/$ – see front matter
PII: S0257-8972(98)00629-X

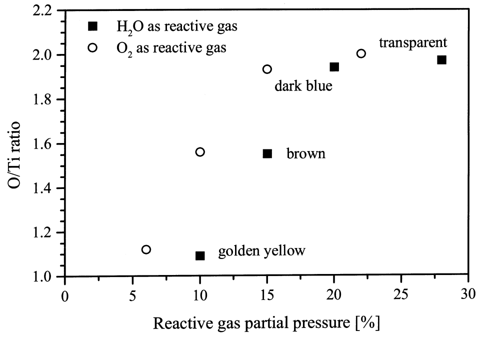

Fig. 1. Chemical composition of TiO_{1+x} thin films versus reactive gas partial pressure.

about 62 Hz and an amplitude of about 1 nm. This kind of measurement provides hardness, *E* modulus, and stiffness data throughout the whole indentation depth. Hardness values were taken at 200–300 nm depth to avoid influences of the surface roughness and of the substrate. The XPS studies were performed using a Scienta ESCA 300 system equipped with a rotating anode (Al Kα source), an X-ray monochromator, and a hemispherical analyzer.

3. Results

3.1. Composition and structure

The chemical composition of the thin films as a function of the partial pressure of reactive gas is reported in Fig. 1. TiO_{1+x} can be deposited with either O_2 or H_2O as reactive gas. The H_2O partial pressure must be higher than the O_2 partial pressure to obtain a given chemical composition, which is explained by the fact that at the same pressure O_2 provides two oxygen atoms compared to only one for H_2O. Changes in oxygen concentration in the films are accompanied by color changes from golden yellow for nearly stoichiometric TiO films to transparent for TiO_2 films, passing through brown and dark blue. secondary ion mass spectroscopy (SIMS) reveals the same small hydrogen content in thin films deposited with either H_2O or O_2. The origin of this small, constant hydrogen concentration is attributed to contamination of the films by atmospheric water after their removal from the deposition chamber.

The XRD results, presented in Fig. 2, reveal that transparent TiO_{1+x} films ($0.95 \leq x \leq 1$) are composed of a mixture of the anatase and rutile phases. When the oxygen concentration decreases the rutile phase dominates with a very small grain size ($d<5$ nm). At lower oxygen concentration, type B TiO_{1+x} amorphous films are obtained, while type A TiO_{1+x} X-ray diffraction spectra show Ti_2O_3 and Ti_3O_5 patterns. No amorphous type A TiO_{1+x} thin films were observed. Golden yellow TiO_{1+x} ($0 \leq x \leq 0.25$) have the same fcc NaCl structure as TiN. The lattice parameter $a=0.422$ nm in the case of type B TiO_{1+x}, which is considerably larger than the lattice parameter $a=0.418$ nm reported in the literature for $TiO_{1.12}$ crystals [6]. In the case of type A TiO_{1+x}, the lattice parameter $a=0.419$ nm almost matches the values found in single crystals.

Fcc $TiO_{1.16}$ thin films deposited with H_2O as reactive

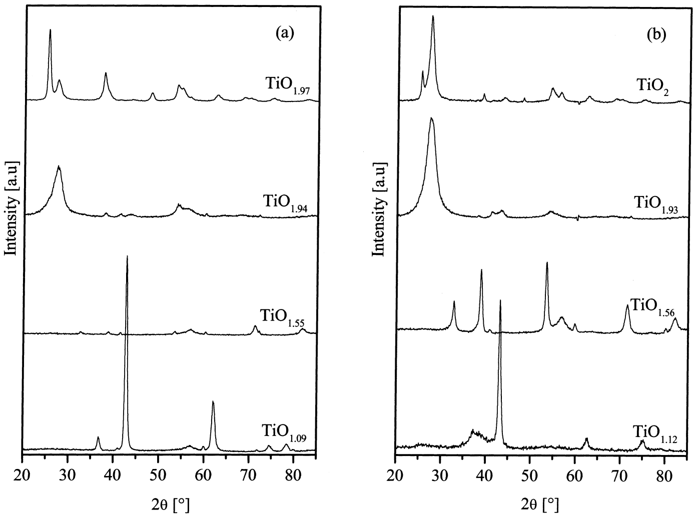

Fig. 2. X-ray diffraction spectra of TiO_{1+x} deposited with (a) H_2O and (b) O_2 as reactive gas.

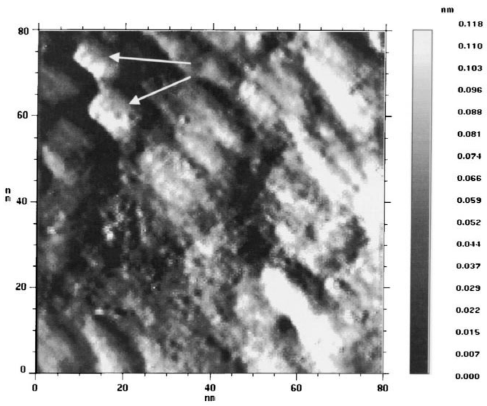

Fig. 3. STM image of fcc $TiO_{1.16}$ deposited with H_2O as reactive gas.

gas have a very smooth surface as we can see on STM image (Fig. 3). In Fig. 3, rectangular patterns (highlighted by white arrows), typical of the fcc phase, are present. The size of these patterns, about 15 nm, is in good agreement with the crystallite size measured by XRD (d=15 nm). The surface of amorphous type B TiO_{1+x} thin film is presented in Fig. 4a. The layer is composed of regular spherical grains with a diameter of 150 nm. The amorphous agglomerates are much larger than the grains of crystallized TiO_2 thin films (Fig. 4b).

3.2. Electronic properties

XPS measurements of the Ti 2p spectra on golden yellow $TiO_{1.16}$ deposited with H_2O show features which can be associated with several valence states of Ti. To obtain an insight into the composition, the spectra were deconvoluted, assuming contributions from the Ti^0, Ti^{2+}, Ti^{3+} and Ti^{4+} species, which are encountered in Ti metal, TiO, Ti_2O_3 and TiO_2. The most intense peak is associated with Ti^{4+} (458.6 eV). This means that the sample surface is heavily oxidized. The Ti^{3+} peak (456.9 eV) and the Ti^{2+} peak (455.1 eV) show that the sample composition lies between x=0 and x=0.5. Some metal titanium represented by a peak at 454.0 eV is probably located in the grain boundaries.

The electrical resistivity decreases rapidly with decreasing oxygen concentration and then stabilizes at 4×10^{-6} Ω m (Fig. 5). The resistivity is higher than the value reported for bulk material, 2.60×10^{-6} Ω m for $TiO_{1.2}$ [7], because of the small grain size and of grain boundary effects. Except at high oxygen concentrations, type B TiO_{1+x} and type A TiO_{1+x} exhibit the same values for electrical resistivity.

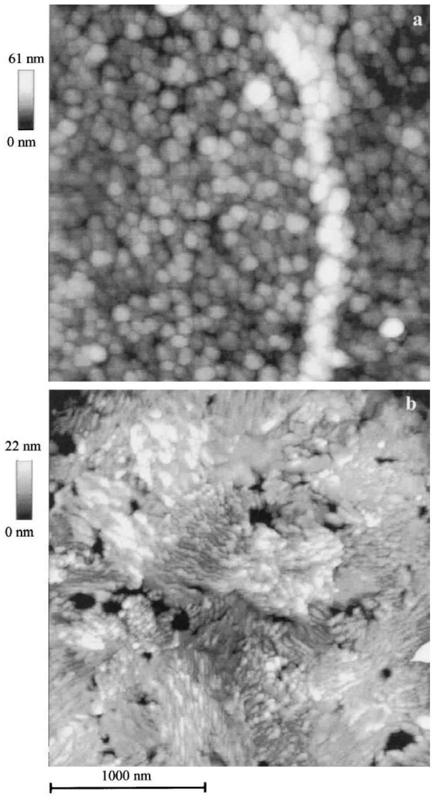

Fig. 4. AFM images of (a) amorphous $TiO_{1.75}$ thin film deposited with H_2O as reactive gas, (b) anatase TiO_2 thin film deposited with O_2 as reactive gas.

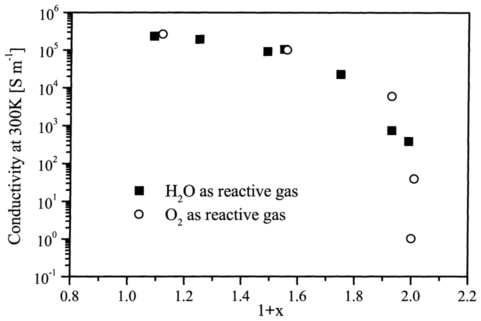

Fig. 5. Electrical conductivity of Type B TiO_{1+x} and Type A TiO_{1+x} thin films at room temperature.

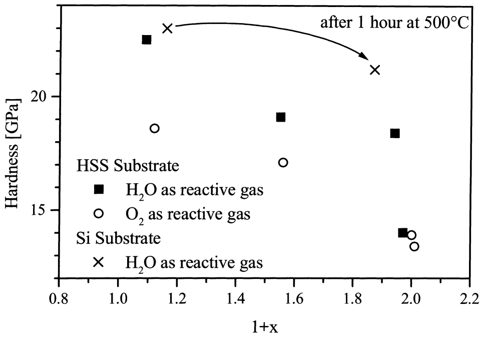

Fig. 6. Hardness of Type B TiO_{1+x} and Type A TiO_{1+x} thin films.

Preliminary spectroscopic ellipsometry measurements have been performed on TiO_{1+x} films. The golden yellow color stems from the position of the reflectivity minimum, corresponding to the energy of a screened, free-carrier plasmon, at about 3 eV. The screened plasmon frequency shifts from 3 to 1.8 eV when the oxygen concentration increases. This shift has a strong impact on the apparent color of the TiO_{1+x} films. A detailed study of the optical properties of the TiO_{1+x} thin films will be published elsewhere.

3.3. Nanohardness

Nanohardness varies from 13.4 GPa for anatase TiO_2 thin films to 22.5 GPa in cubic TiO_{1+x} (Fig. 6). Type B TiO_{1+x} thin films exhibit a higher hardness value than type A TiO_{1+x} thin films at the same chemical composition, only at x~0.95 do both deposition methods show similar results. Cubic TiO_{1+x} films oxidized at 500°C under air for 1 h, despite a limited drop of the hardness value from 23 to 21.2 GPa, still exhibit larger hardness values than pristine films (cross on Fig. 6).

4. Discussion

Although the electrical conductivity is similar in type A and type B TiO_{1+x} films, their hardness values exhibit large differences. In particular, type B TiO_{1+x} films (deposited with water as reactive gas) with $x<1$ exhibit higher hardness values compared to those of conventional type A films (Fig. 6). This could be of great interest in industrial applications, which require improved mechanical properties. The mechanical properties of these films are related to crystal structure, electronic structure and film morphology (grain size, grain boundary properties, residual stress) [1]. Therefore, the changes in electrical and mechanical properties of TiO_{1+x} films as a function of the oxygen content ($0<x<1$) can be understood considering the crystal structure and the electronic structure. The differences in the mechanical properties between type A and type B films can essentially be explained by noticeable modifications of the morphology of type B thin films due to the interaction with water.

4.1. Crystal structure and electronic properties

As deduced from XRD data, the crystal structure of TiO_{1+x} films changes from cubic fcc TiO (type NaCl) through amorphous or trigonal Ti_2O_3 to tetragonal TiO_2 (rutile or anatase) when x increases from 0 to 1. For $0<x<0.2$, as in fcc mono-nitrides and carbides, the physical properties of fcc TiO_{1+x} films stem from mixed ionic, covalent and metallic contributions to Ti and O bonding [8,9]. The higher hardness values observed in fcc TiO_{1+x} films compared to those of TiO_2 films arise mainly from the fact that the bonding between Ti and O atoms is more strongly covalent in a fcc than in a tetragonal structure. The decrease of the hardness with increasing oxygen concentration for both type A and type B thin films is due to the increase of the ionic character of the Ti–O bonding (see Fig. 6).

4.2. Film morphology

Understanding of the effect of water vapor as reactive gas on the growth mechanism and on the mechanical properties (hardness and adherence) of TiO_{1+x} films remains a great challenge. The hardness differences, at a given chemical composition, cannot be explained by a single parameter. In each case the crystal structure and the morphology of the films must be considered. Thus, in the case of TiO_{1+x} films with $x<0.2$, the crystal structure is the same (fcc type NaCl), and only low tensile stress levels (<150 MPa) were determined by the $\sin^2\Psi$ method in XRD in both cases. A preliminary analysis of scanning electron micrographs revealed a dense granular morphology in type B films, whereas type A films exhibit a columnar morphology. Therefore the influence of the morphology has to be considered when one attempts to explain the mechanical properties. For TiO_{1+x} with x~0.55 two different structures are observed: an amorphous structure for type B $TiO_{1.55}$ and a mixture of Ti_2O_3 and Ti_3O_5 for type A $TiO_{1.56}$. These structural differences lead to differences in hardness. In the case of tetragonal TiO_2 films, the dark blue rutile has a significantly smaller grain size than transparent rutile (3 vs 12 nm) and a higher hardness, which is in agreement with the Hall Petch relation [1].

The interaction of water with TiO_2, Ti_2O_3 and $SrTiO_3$ single-crystal surfaces has been thoroughly investigated by other authors because of the catalytic properties of these surfaces [10–12]. Both nearly perfect and defective surfaces give rise to dissociative adsorption of H_2O at 300 K. In particular from the photoemission studies it is deduced that the dissociative adsorption of H_2O results in an increased concentration of Ti^{3+} surface defect states on nearly perfect surfaces [10]. In the case of anatase TiO_2 single crystals exposed to H_2O or H_2, the appearance of new features in the XPS valence band spectra attributed to adsorbed OH^- radicals was also reported [13]. These results support the assumption that dissociative adsorption/desorption of H_2O molecules can also take place at the surface of the crystallites during the deposition of type B TiO_{1+x} films using water vapor as reactive gas. The crystallites of the synthesized films certainly exhibit the same surface defects as the single crystals described above. These defects, characterized by changes in the Ti–O bonding, are most likely to have profound effects on the intergrain cohesion and on the hardness.

Since no actual hydrogen incorporation is detected in type B TiO_{1+x} films, and since the type B TiO_{1+x} and type A TiO_{1+x} films do exhibit a different morphology, we conclude that hydrogen or water vapor acts as a catalyst during the deposition. The fact that type B TiO_{1+x} adheres poorly on HSS shows that water vapor influences the substrate properties as in the case of indium tin oxide deposited in the presence of water vapor [14]. The anatase peaks of the 50 nm, adhesion TiO_2 sublayer do not show in the XRD spectra of cubic and amorphous type B TiO_{1+x}. Moreover, golden yellow cubic type B TiO_{1+x} develops a dark blue interface region at the junction with the adhesion layer, as can be seen easily from the back side through the glass substrate. This means that a chemical reaction take place at the interface resulting in a gradient of the oxygen concentration at the interface. The concentration gradient seems to be necessary for adhesion. Indeed a type B TiO_{1+x} does not adhere on top of a 50-nm type A TiO_{1+x} layer with similar chemical composition and structure.

5. Conclusions

We have shown the structural differences of TiO_{1+x} thin films deposited with O_2 or H_2O as reactive gas. Reactive sputtering with oxygen favors complete oxidation of titanium at the grain surfaces. The presence of water during film deposition prevents titanium oxidation into TiO_2. The structural differences, especially at the grain boundaries, result in a higher hardness in the case of TiO_{4x} deposited with H_2O as reactive gas. The highest hardness value measured on HSS substrates (22.5 GPa) is obtained for golden yellow $TiO_{1.09}$ with fcc, TiN-like structure.

Acknowledgements

This work was supported by the Fonds National Suisse de la Recherche Scientifique. Particular thanks are due to H. Jotterand and A. Gentile for experimental support, Dr A. Karimi for help in the nanoindentation, and Dr F. Bussy at the University de Lausanne for the electron probe microanalysis measurements.

References

[1] J.-E. Sundgren, H.T.G. Hentzell, J. Vac. Sci. Technol. A4 (1986) 2259.

[2] B. Milosev, H.-H. B. Navinsek, Strehblow, Corrosion properties of hard PVD nitride coatings (with the emphasis on TiN), in: Scientific Series of the International Bureau, vol. 37, Forschungszentrum Jülich GmbH, 1995.

[3] G.V. Samsonov, I.M. Vimitskii, Handbook of Refractory Compounds, IFI/Plenum, New York, 1980.

[4] G.V. Samsonov, The Oxide Handbook, IFI/Plenum, New York, 2nd ed., 1982.

[5] H. Tang, K. Prasad, R. Sanjinés, P.E. Schmid, F. Lévy, J. Appl. Phys. 75 (1994) 2042.

[6] K.-H. Hellwege, Landolt-Börnstein Numerical Data and Functional Relationships in Science and Technology, vol III/7b1, Springer Verlag, Berlin, 1975.

[7] C.N.R. Rao, W.E. Wahnsiedler, J.M. Honig, J. Solid State Chem. 2 (1970) 315.

[8] A. Neckel, Int. J. Quantum Chem. 23 (1983) 1317.

[9] S.R. Barman, D.D. Sarma, Phys. Rev. B49 (1994) 16141.

[10] R.L. Kurtz, R. Stockbauer, T.E. Madey, E. Roman, J.L. de Segovia, Surf. Sci. 218 (1989) 178.

[11] V.E. Henrich, Rep. Progress Phys. 48 (1985) 41.

[12] S. Ferrer, G.A. Somorjai, Surf. Sci. 94 (1980) 41.

[13] R. Sanjinés, H. Tang, H. Berger, F. Gozzo, G. Margaritondo, F. Lévy, J. Appl. Phys. 75 (1994) 2945.

[14] Y. Shigesato, Y. Hayashi, A. Masui, T. Haranou, Jpn. J. Appl. Phys. 30 (1991) 814.

Acknowledgements

I would first like to thank Dr P. E. Schmid, my PhD director, who has guided me during the full time of the thesis and has read this manuscript with a critical and constructive mind. I thank Professor F. Lévy, who welcomed me in his laboratory and who gave me the opportunity to do this thesis.

I thank Dr F. Bussy, from the Institute of Mineralogy at the University of Lausanne, who performed the chemical analysis with EPMA, and Dr D. Léonard from the Materials Department at the EPFL for the SIMS measurements.

I am grateful to Dr R. Sanjines for his perpetual good spirits and for the fruitful discussions we have had together. I thank Dr K. Prasad, Mrs E. N. Korobeinikova, Dr C. Zakri, and Dr N. Martin, who worked on subjects close to mine and have shared their knowledge with me. This work could not have been completed without the technical support of Mr H. Jotterand, A. Gentile, and L. Braun. I would also like to thank all staff of the Institute of Applied Physics.

Finally, I thank my family and my friends who have supported me during these long years of study.

Curriculum Vitae

Nom	Bally
Prénoms	Alain Robert
Né	le 21 avril 1972
À	Lausanne, Suisse
Nationalité	Suisse

Formation

1987 - 1990	Gymnase Cantonal de la Cité, Lausanne obtention de la maturité fédérale type C (scientifique)
1990 – 1995	Ecole Polytechnique Fédérale de Lausanne obtention du diplôme d'ingénieur physicien

Stage

Eté 1993	Stage chez Nestec S.A., Linor, « Propriétés barrière de dépositions SiO_x sur papier-carton »

Activité d'enseignement et de recherche

1995-1999	Assistant-doctorant à l'Institut de Physique Appliquée de l'Ecole Polytechnique Fédérale de Lausanne travail de thèse sur les couches minces d'oxyde de titane

Publications

“TiO_2:Ce/CeO_2 High Performance Insulators for Thin Film Electroluminescent Devices”: A. R. Bally, K. Prasad, R. Sanjines, P.E. Schmid, F. Levy, J. Benoit, C. Barthou, and P. Benalloul, MRS 1996 Spring Meeting, Material Research Society Symposium Proceeding Vol. 424 (1997) 471.

“Ce-doped TiO_2 Insulators in Thin Film Electroluminescent Devices”: K. Prasad, A. R. Bally, P. E. Schmid, F. Levy, J. Benoit, C. Barthou, and P. Benalloul, Japanese Journal of Applied Physics 36(9A) (1997), 5696.

“Structural and Electrical properties of Fe-doped TiO_2 thin films”: A. R. Bally, E. N. Korobeinikova, P. E. Schmid, F. Levy, and F. Bussy, Journal of Physics D: Applied Physics 31(10) (1998), 1149.

“Reactive sputtering as a tool for preparing photocatalysts”: D. Dumitriu, A. R. Bally, C. Ballif, V. I. Parvulescu, P. E. Schmid, R. Sanjinés, and F. Lévy, Preparation of Catalysts VII (B. Delmon et al., editors.) (1998), 485.

“Mechanical and electrical properties of fcc TiO_{1+x} thin films prepared by RF reactive sputtering”, A.R. Bally, P. Hones, R. Sanjinés, P. E. Schmid, and F. Lévy, Surface and Coatings Technology 108-109 (1998), 166.

“Photocatalytic degradation of phenol by TiO_2 thin films prepared by sputtering technique”: D. Dumitriu, A. R. Bally, C. Ballif, P. Hones, P. E. Schmid, R, Sanjinés, F. Lévy, and V. I. Parvulescu, to be published.

Conférences

“Dielectric Properties of Ce-doped Titanium Dioxide Thin Films”: A. R. Bally, K. Prasad, R. Sanjinés, P. E. Schmid, and F. Lévy, Session d’automne de la Société Suisse de Physique, Saint-Gall (Suisse), 1995.

“TiO_2:Ce/CeO_2 high performance insulators for thin film electroluminescent devices”: A. R. Bally, K. Prasad, R. Sanjines, P.E. Schmid, F. Levy, J. Benoit, C. Barthou, and P. Benalloul, MRS 1996 Spring Meeting, San Francisco (USA), 1996.

“Electrical properties of Nb, F, and Fe-doped TiO_2 thin films”: A. R. Bally, P. E. Schmid, and F. Lévy, Session d’automne de la Société Suisse de Physique, Zürich (Suisse), 1996.

“Highly conductive titanium oxide thin films by reactive sputtering”: A. R. Bally, R. Sanjinés, P. E. Schmid, and F. Lévy, Session d’automne de la Société Suisse de Physique, La Chaux-de-Fonds (Suisse), 1997.

“Mechanical and electrical properties of fcc TiO_{1+x} thin films prepared by RF reactive sputtering”, A. R. Bally, P. Hones, R. Sanjinés, P. E. Schmid, F. Lévy, International Conference on Metallurgical Coatings and Thin Films, San Diego (USA), 1998.